

Latent Room-Temperature T_c in Cuprate Superconductors

Jamil Tahir-Kheli*

Applied Physics and Chemistry,

Beckman Institute (MC 139-74),

California Institute of Technology, Pasadena CA 91125

(Dated: February 15, 2017)

Abstract

The ancient phrase, “All roads lead to Rome” applies to Chemistry and Physics. Both are highly evolved sciences, with their own history, traditions, language, and approaches to problems. Despite all these differences, these two roads generally lead to the same place. For high temperature cuprate superconductors however, the Chemistry and Physics roads do not meet or even come close to each other. In this paper, we analyze the physics and chemistry approaches to the doped electronic structure of cuprates and find the chemistry doped hole (out-of-the-CuO₂-planes) leads to explanations of a vast array of normal state cuprate phenomenology using simple counting arguments. The chemistry picture suggests that phonons are responsible for superconductivity in cuprates. We identify the important phonon modes, and show that the observed $T_c \sim 100$ K, the T_c -dome as a function of hole doping, the change in T_c as a function of the number of CuO₂ layers per unit cell, the lack of an isotope effect at optimal T_c doping, and the D-wave symmetry of the superconducting Cooper pair wavefunction are all explained by the chemistry picture. Finally, we show that “crowding” the dopants in cuprates leads to a pair wavefunction with S-wave symmetry and $T_c \approx 280 - 390$ K. Hence, we believe there is enormous “latent” T_c remaining in the cuprate class of superconductors.

The highest superconducting transition temperature, T_c , at ambient pressure is 138 K in the Mercury cuprate $\text{HgBa}_2\text{Ca}_2\text{Cu}_3\text{O}_{8+\delta}$ (Hg1223) with three CuO_2 layers per unit cell.^{1,2} Hg1223 was discovered in 1993. The longest time period between record setting T_c discoveries is the 17 years between Pb (1913 with $T_c = 7.2$ K) to Nb (1930 with $T_c = 9.2$ K). With the enormous increase in focus on superconductivity after the discovery of cuprates 30 years ago, the current 24 years without a new record at ambient pressure indicates we may be reaching the maximum attainable T_c .

In this paper, we show this conclusion to be wrong. We demonstrate that T_c can be raised above room-temperature to $\approx 400\text{K}$ in cuprates by precise control of the spatial separation of dopants. Hence, there still remains substantial “latent” T_c in cuprates. Our proposed doping strategy and superconducting mechanism is not restricted to cuprates and may be exploited in other materials.

Our room-temperature T_c result is based upon four observations:

- Cuprates are intrinsically inhomogeneous on the atomic-scale and are comprised of insulating and metallic regions. The metallic region is formed by doping the material.
- A diverse set of normal state properties are explained solely from the topological properties of these two regions and their doping evolution.
- Superconductivity results from phonons at or adjacent to the interface between the metallic and insulating regions. Transition temperatures $T_c \sim 100$ K are possible because the electron-phonon coupling is of longer-range than metals (nearest neighbor).
- These interface phonons explain the observed superconducting properties and lead to our prediction of room-temperature superconductivity.

How is our claim of room-temperature T_c possible? The talent and funding invested into finding the mechanism of cuprate superconductivity and higher T_c materials has led to more than 200,000 refereed papers.³ After this mind-boggling quantity of literature, it seems unlikely that any unturned stones remain that could lead to our prediction.

Our claim does not come from locating an overlooked stone beneath the cuprate stampede. Instead, we believe the majority of the cuprate community settled upon the incorrect orbital nature of the doped hole. This mistake led to Hamiltonians (Hubbard models) that “threw the baby out with the bath water.”

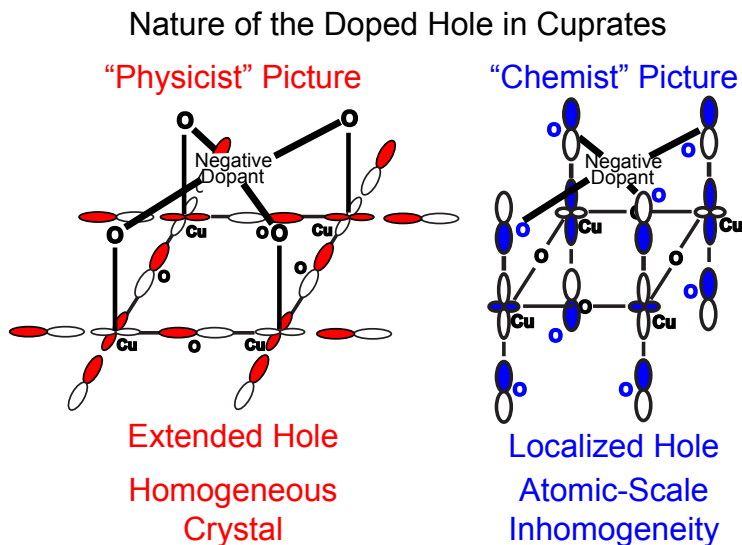


FIG. 1. The difference in the character of the doped hole using the “physicist’s” density functionals, LDA and PBE, versus the “chemist’s” hybrid density functionals. The dopant is negatively charged and resides out-of-the CuO_2 plane. The physicist’s hole state has density in the CuO_2 plane and is delocalized over the crystal. It is a peculiar hole state. Intuitively, one would expect the positive hole charge to point at the negatively charged dopant. The chemist’s hole state density is out-of-the- CuO_2 plane (points at dopant), and is localized around the four-Cu-site plaquette beneath the dopant. In the chemist’s view, the crystal has atomic-scale inhomogeneity that is not a small perturbation of translational symmetry. The physicist’s view leads to an approximately homogeneous crystal.

A major reason for the early adoption of these Hubbard models for cuprates was due to computational results using the ab initio local density approximation (LDA) in density functional theory (DFT). While LDA is now deprecated, being replaced by the Perdew-Burke-Ernzerhof functional⁴ (PBE), both functionals lead to exactly the same doped hole wavefunction in cuprates. These “physicist” functionals find the doped hole to be a *delocalized wavefunction* comprised of orbitals residing in the CuO_2 planes common to all cuprates.⁵⁻⁷ Unfortunately, LDA and PBE both contain unphysical Coulomb repulsion of an electron with itself.⁸ The “chemist” hybrid density functionals, invented in 1993 (seven years after the discovery of cuprate superconductivity), corrected for this self-Coulomb error, and thereby found the doped hole residing in a *localized wavefunction* surrounding the dopant atom with orbital character pointing out of the CuO_2 planes.^{9,10} The physicist and

chemist doped holes are shown in Figure 1. A discussion of the superiority of the chemist’s DFT to the physicist’s DFT is in Appendix A.

The “chemist’s” ab initio doped hole leads to eight *electronic structure concepts* that explain a vast array of normal and superconducting state phenomenology using simple counting. These eight structural concepts are described below.

STRUCTURAL CONCEPT 1: Cuprates are inhomogeneous on an atomic-scale. The inhomogeneity is not a small perturbation to translational symmetry. It must be included at zeroth order.

STRUCTURAL CONCEPT 2: The Cuprate motif is a four-Cu-site plaquette formed by each dopant. See Figure 2. The out-of-the-CuO₂ plane negative dopant is surrounded by an out-of-the-CuO₂ plane hole. The hole is comprised of apical Oxygen p_z and planar Cu $d_{3z^2-r^2}$ character. There is also some planar O p_σ character that is not drawn.

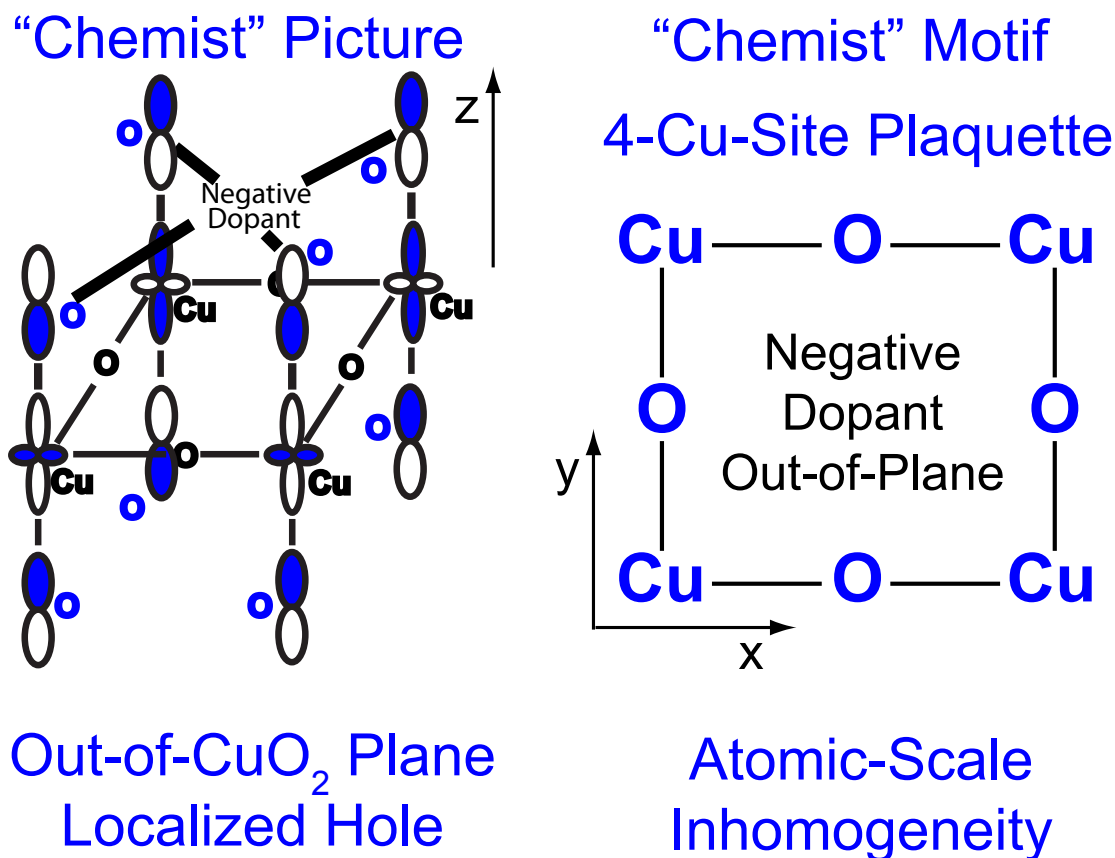


FIG. 2. The doped four-Cu-site plaquette “motif.”

STRUCTURAL CONCEPT 3: A tiny piece of metal is formed within each plaquette from electron delocalization in the *planar* Cu $d_{x^2-y^2}$ and O p_σ (p_x and p_y) orbitals. See Figure 3. Delocalization occurs because the positive charge of the out-of-plane hole lowers the Cu $d_{x^2-y^2}$ orbital energy relative to the O p_σ orbital energy. In contrast, these electrons are localized in a spin-1/2 antiferromagnetic (AF) state in an undoped plaquette.

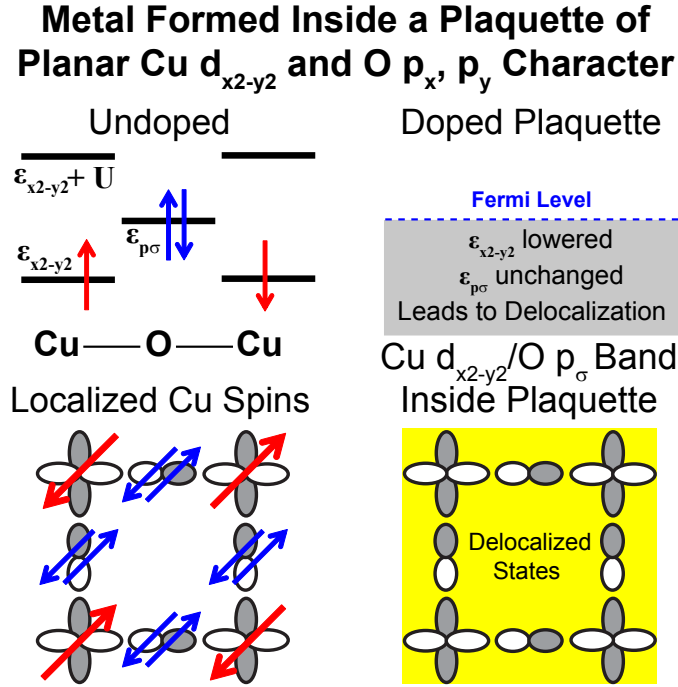


FIG. 3. The mechanism for the creation of delocalized *planar* metallic wavefunctions inside a doped plaquette. (a) The Cu $d_{x^2-y^2}$ and O p_σ orbital energies in an undoped plaquette. The energy ordering, $\epsilon_{x^2-y^2} < \epsilon_{p\sigma} < \epsilon_{x^2-y^2} + U$, where U is the large on-site Cu $d_{x^2-y^2}$ Coulomb repulsion leads to localization of the spins on the Cu sites, and hence the undoped AF state. (b) The induced delocalization (yellow overlay) of the *planar* Cu $d_{x^2-y^2}$ and O p_σ electrons in the plaquette from the decrease of the Cu $d_{x^2-y^2}$ orbital energy relative to the O p_σ orbital energy. The decrease occurs because the positive charge of the chemist's out-of-the-plane hole from Figures 1 and 2 is closer to the planar Cu site. The out-of-plane hole is not shown here. There are a total of 4 O atom p_σ orbitals and 4 Cu $d_{x^2-y^2}$ orbitals inside the four-Cu-site plaquette. Since there are two spin states for each orbital, there is a total of $(4 + 4) \times 2 = 16$ states in the yellow overlay in the bottom right figure. These 16 states are filled with the 12 electrons (4 red plus 8 blue) shown in the lower left figure.

STRUCTURAL CONCEPT 4: A metal is formed when the doped plaquettes percolate through the crystal. When a three-dimensional (3D) pathway of adjacent doped plaquettes is created through the crystal (percolation of the plaquettes), a metallic band comprised of *planar* Cu $d_{x^2-y^2}$ and O p_σ orbitals is created inside the percolating region. These delocalized metallic wavefunctions do not have momentum, \mathbf{k} , as a good quantum number. Two-dimensional (2D) percolation occurs at a higher doping ($x \approx 0.15$ holes per planar Cu) than the start of 3D percolation (at $x \approx 0.05$ holes per planar Cu). See Figure 4. The undoped (non-metallic) region remains an insulating spin-1/2 AF. Thus cuprates have both insulating and metallic regions on an atomic-scale.

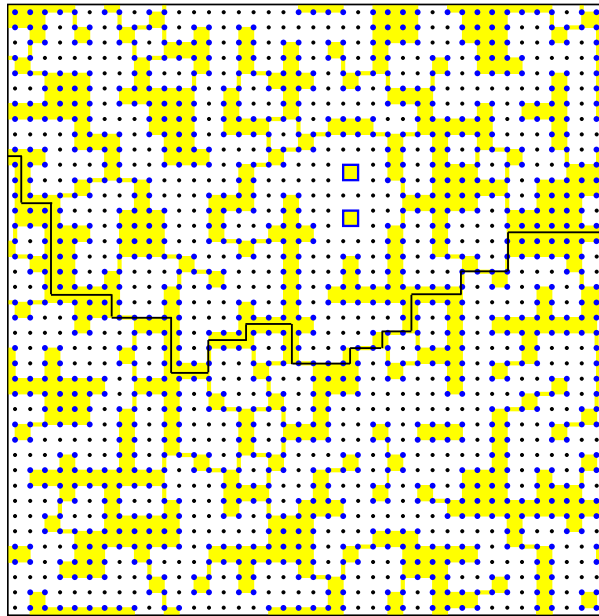


FIG. 4. A 2D percolating pathway in an optimally doped CuO_2 plane ($x = 0.16$ dopants per planar Cu). The black line shows a pathway from the left to the right side of this 40×40 CuO_2 lattice. The localized antiferromagnetic (AF) spins on the Cu sites are shown as black dots. The blue dots are Cu sites inside the doped metallic region. The O atoms are not shown. The yellow overlay represents the delocalized metallic band comprised of planar orbitals inside the doped region. The blue squares represent isolated plaquettes (not adjacent to another plaquette). There is a degeneracy at the Fermi level inside each isolated plaquette (see Appendix B) that is split by its interaction with the crystal environment, and thereby leads to the pseudogap.¹¹ The number of isolated plaquettes “vanish” (become of measure zero) at hole doping $x \approx 0.19$ where the cuprate pseudogap is known to disappear.¹¹ The *tenuous* percolating pathway has poor critical current.

STRUCTURAL CONCEPT 5: The out-of-the- CuO_2 plane hole shown in Figures 1 and 2 is a dynamic Jahn-Teller distortion that is a linear superposition of two “frozen dumbbell” states. See Figure 5. Figure 25 in Appendix C shows that the out-of-the-plane hole goes into the states in Figure 5. We call the dynamic Jahn-Teller hole state a “fluctuating dumbbell.”

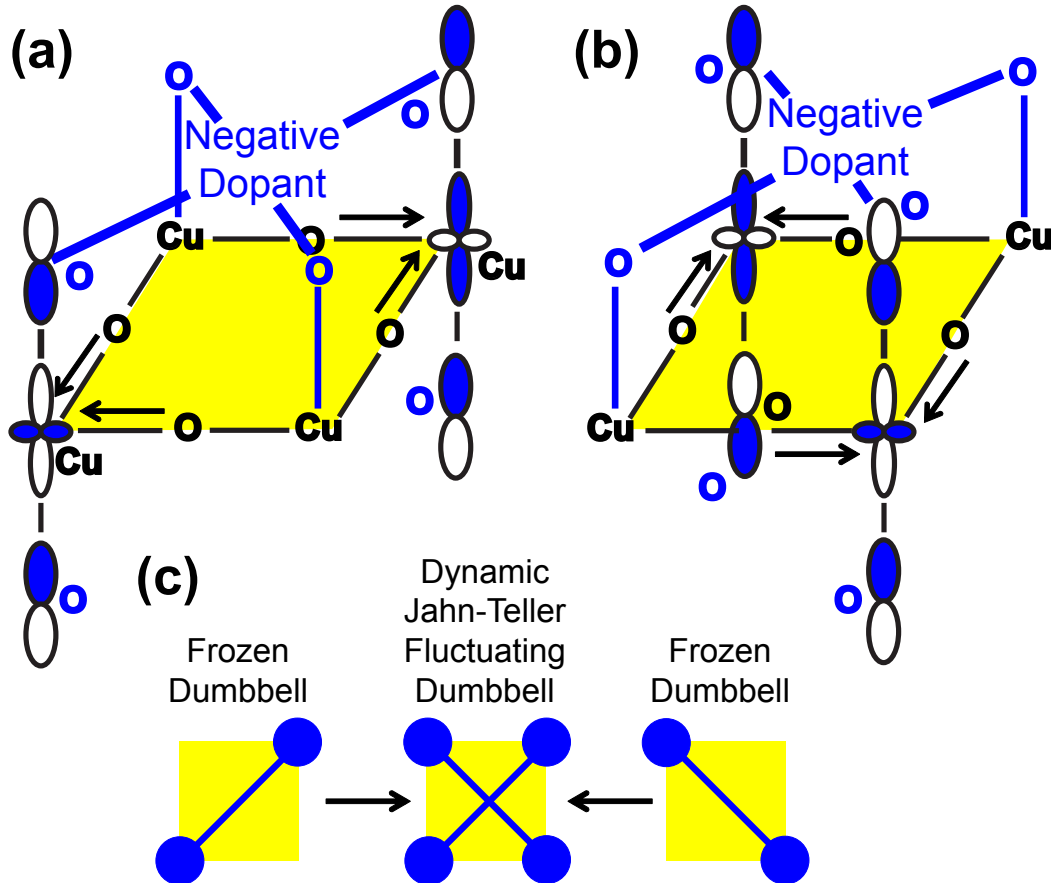


FIG. 5. The character of the out-of-plane hole inside a doped plaquette. The arrows show the displacement of the O atoms in the CuO_2 plane with each “frozen dumbbell” configuration. We propose that the out-of-plane hole wavefunction is a dynamic Jahn-Teller state that is a linear superposition of the two dumbbells shown in (a) and (b) (called a “fluctuating dumbbell”). We represent the two frozen dumbbells in (a) and (b) schematically by the left and right figures in the bottom row. The fluctuating dumbbell is shown in the center figure at the bottom. The yellow overlay represents the *planar* Cu $d_{x^2-y^2}$ and O p_σ electrons (not shown) that are delocalized inside the plaquette.

STRUCTURAL CONCEPT 6: A fluctuating dumbbell can be frozen by overlapping its plaquette with another plaquette. See Figure 6.

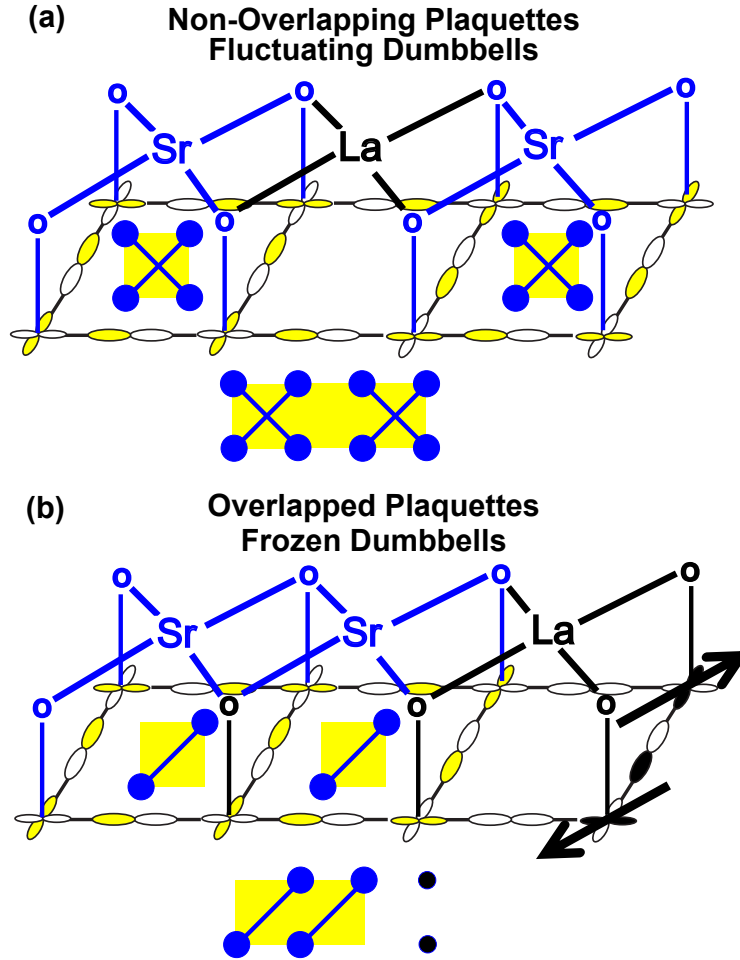


FIG. 6. The effect of overlapping plaquettes on the fluctuating dumbbells for the case of Sr doping of $\text{La}_{2-x}\text{Sr}_x\text{CuO}_4$. (a) Two non-overlapping plaquettes with fluctuating dumbbells. The top figure shows the CuO_2 layer and the out-of-the-plane Sr dopants. The schematic figure below shows the metallic delocalization of the *planar* Cu $d_{x^2-y^2}$ and O p_σ orbital electrons (yellow overlay) and the two fluctuating dumbbells. (b) Two overlapping plaquettes. The degeneracy of the two dumbbell states inside each plaquette is broken and the two dynamic Jahn-Teller fluctuating dumbbells become two frozen dumbbells. The bottom figure shows a schematic of the metallic regions (yellow overlay) and the frozen dumbbells. The orientation of the dumbbells in this figure is arbitrary. The actual orientation in the crystal will depend on the environment.

STRUCTURAL CONCEPT 7: If possible, plaquettes avoid overlapping. Since the dopant atom is negatively charged, two plaquettes will repel each other. Their Coulomb repulsion is short-ranged because of screening from the planar metallic electrons. Hence, plaquettes do not overlap, but are otherwise distributed randomly. Plaquettes can avoid overlap up to a hole doping of $x = 0.187$. For dopings greater than $x = 0.187$, plaquettes must overlap. Plaquettes overlap as little as possible to minimize their mutual repulsion. Up to $x = 0.187$ doping, there always exists a four-site square of AF spins where the next plaquette can be placed. For the doping range $0.187 < x < 0.226$, added plaquettes can cover three AF spins. In the range $0.226 < x < 0.271$, plaquettes cover two AF spins, and from $0.271 < x < 0.316$, a single localized spin. At $x = 0.316$, the crystal is fully metallic with no localized spins. Further doping cannot increase the number of metallic sites. Figure 4 shows that plaquettes can avoid overlap at $x = 0.16$ doping. Figure 7 below shows $x = 0.23$ doping, where plaquettes must overlap.

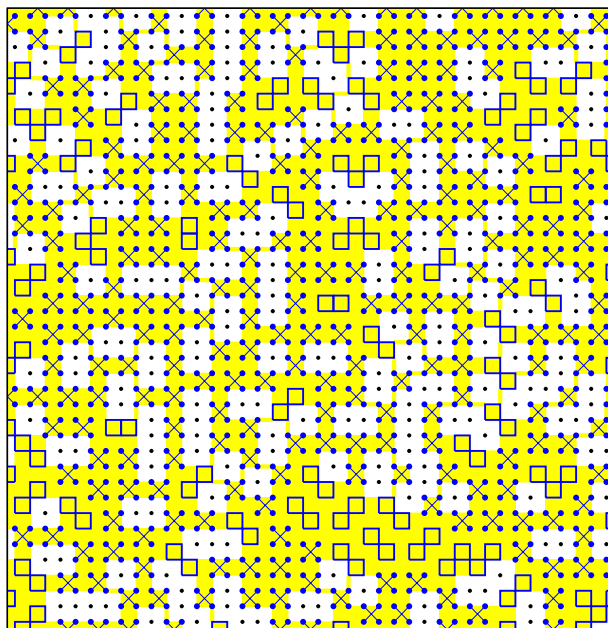


FIG. 7. Plaquette doping at $x = 0.23$ on a 40×40 CuO_2 lattice. The black dots are undoped AF Cu sites. The O atoms are not shown. The yellow overlay represents the delocalized metal comprised of planar Cu $d_{x^2-y^2}$ and planar O p_σ character. Fluctuating dumbbells (blue crosses) are seen in non-overlapped plaquettes. The overlapped plaquettes are shown as blue squares. There are frozen dumbbells inside each blue square. The frozen dumbbells are not shown in the figure.

STRUCTURAL CONCEPT 8: Plaquette Clusters smaller than the superconducting coherence length (~ 2 nm) thermally fluctuate and do not contribute to the superconducting pairing. At low dopings, the plaquettes have not yet merged into a single connected region. There exist plaquette clusters smaller than the coherence length, as shown in magenta in Figure 8. They cannot contribute to the superconducting T_c . These fluctuating clusters lead to superconducting fluctuations above T_c .

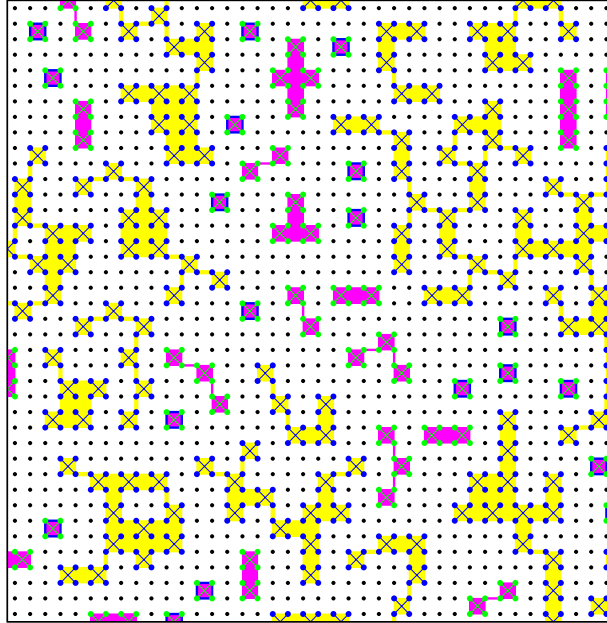


FIG. 8. Plaquette doping of $x = 0.12$ on a 40×40 CuO_2 lattice. The black dots are undoped AF Cu sites. No O atoms are shown. The blue squares are isolated plaquettes (no neighboring plaquette). The yellow overlay represents the metallic region comprised of planar Cu $d_{x^2-y^2}$ and planar O p_σ character. Fluctuating dumbbells (blue and green crosses) are seen in non-overlapped plaquettes. The magenta clusters are smaller than the Cooper pair coherence length and do not contribute to superconducting pairing. Since the size of a single plaquette (the Cu–Cu distance) is ≈ 3.8 Å and the superconducting coherence length is ~ 2 nm, we have chosen plaquette clusters fewer than or equal to 4 plaquettes in size to be fluctuating. The magenta overlay means there is metallic delocalization of the planar Cu and O orbitals in these clusters. The isolated plaquettes do not contribute to the superconducting pairing and the superconducting fluctuations above T_c because they contribute to the pseudogap, as shown in Appendix B.

Figures 9, 10, and 11 show the evolution of the plaquettes as a function of doping. Only twelve dopings are shown here from the range $x = 0.00$ to $x = 0.32$. The Appendix has similar figures for all dopings in this range in 0.01 increments (Figures S0–S32). Only one CuO_2 plane is shown in each of these figures.

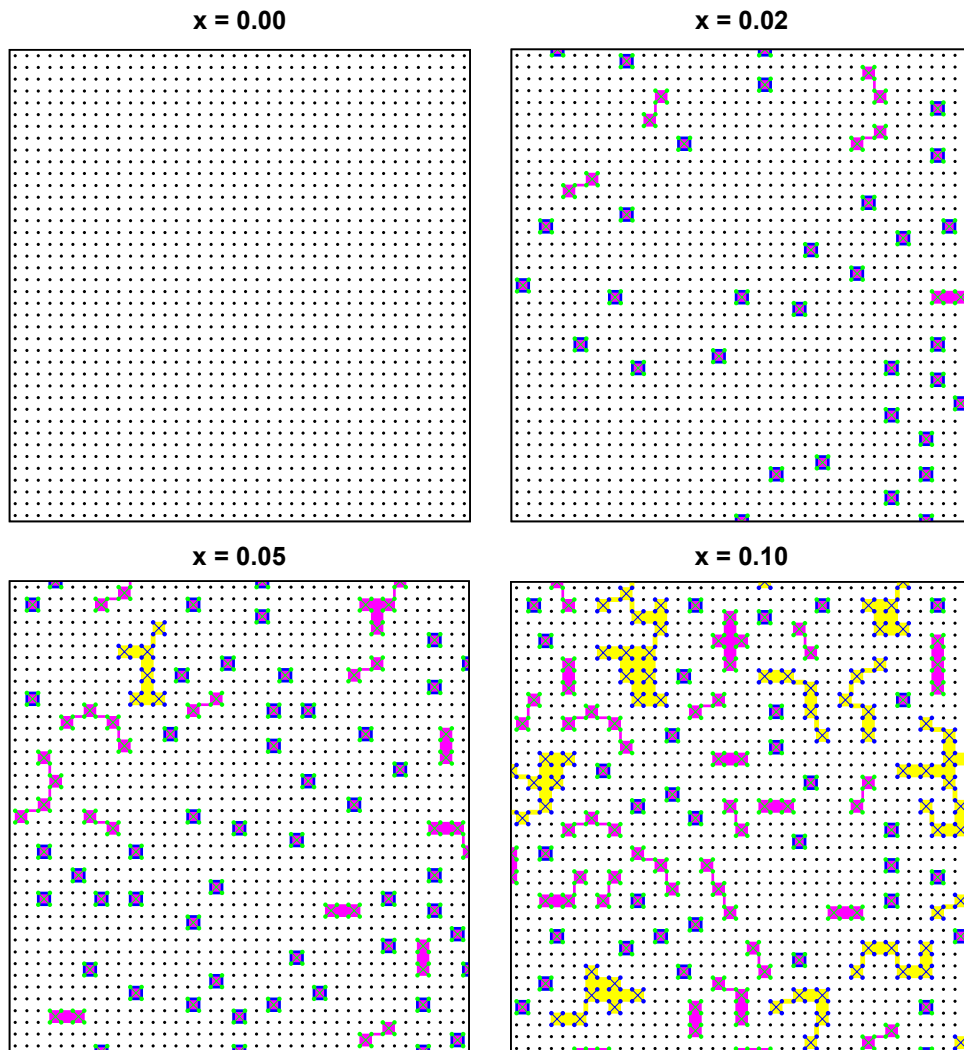


FIG. 9. Plaquette doping of a 40×40 square CuO_2 lattice for dopings $x = 0.00, 0.02, 0.05,$ and 0.10 . Only the Cu sites are shown. The black dots are undoped AF Cu sites. The blue squares are isolated plaquettes (no neighboring plaquette). The yellow plaquette clusters are larger than 4 plaquettes in size (larger than the coherence length), and thereby contribute to the superconducting pairing. The magenta clusters are metallic clusters that are smaller than the coherence length. The blue and green crosses are the fluctuating dumbbells. There is no plaquette overlap in this doping range.

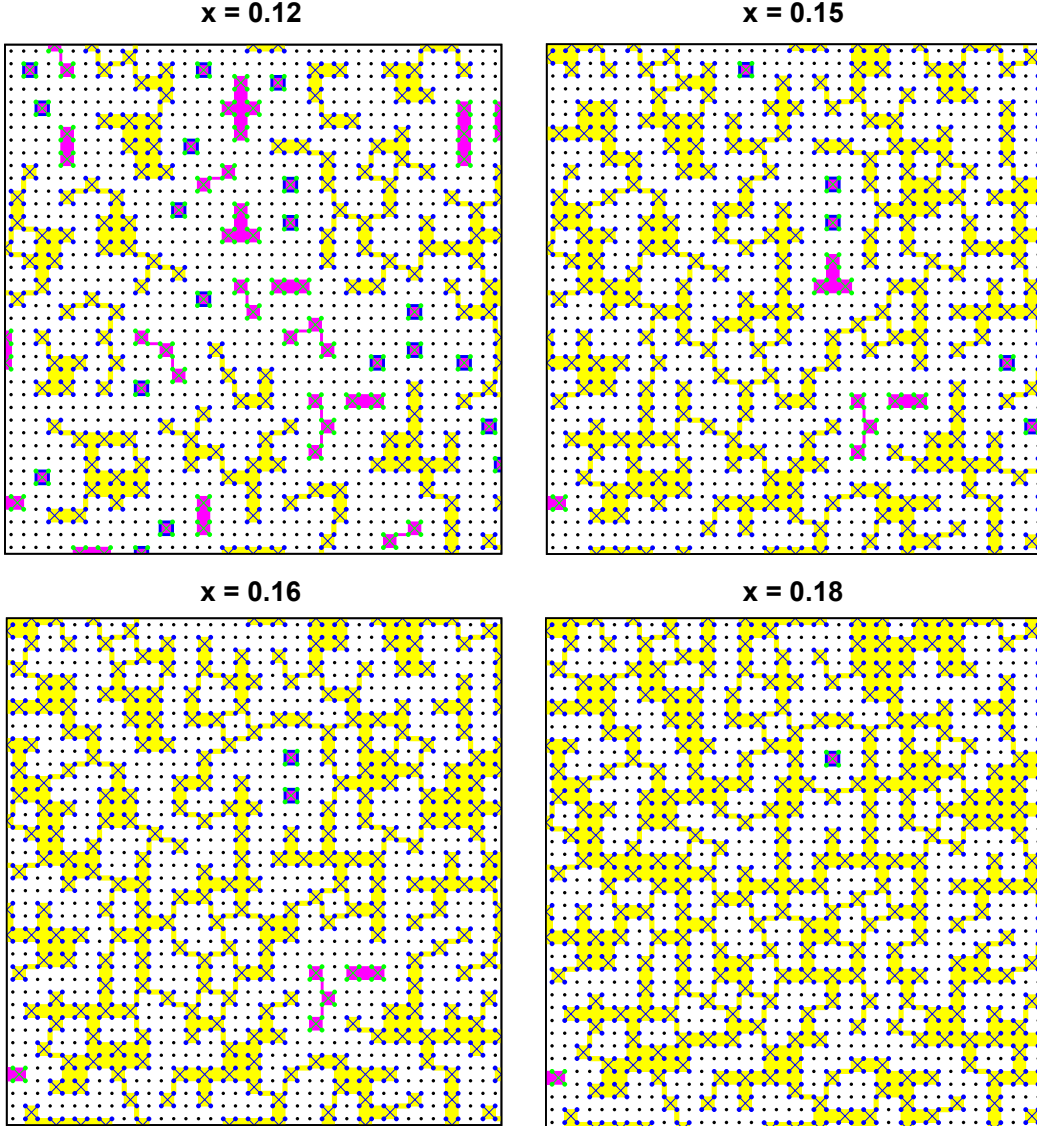


FIG. 10. Plaquette doping at $x = 0.12, 0.15, 0.16$, and 0.18 . The caption of Figure 9 explains the symbols in this figure. Optimal T_c occurs for $x \approx 0.16$ because the *product* of the size of the metallic region (number of electrons that can participate in superconducting pairing) and the size of the interface (the number of pairing phonon modes) is maximized. Percolation in 2D occurs at $x \approx 0.15$. In the finite lattice shown here, there is no 2D percolating metallic pathway for $x = 0.15$. A 2D percolating pathway appears at $x = 0.16$, as shown in Figure 4. The number of isolated plaquettes rapidly decreases over this doping range. By $x = 0.18$ doping, there is only one isolated plaquette in its 40×40 lattice. At optimal doping, the percolation pathway is *very* tenuous. The maximum critical current density, J_c , will be much less than the maximum due to Cooper pair depairing. Using current fabrication methods, cuprates have a low J_c at the highest T_c . Crossing continuous metallic pathways one plaquette in width would have both large T_c and J_c .

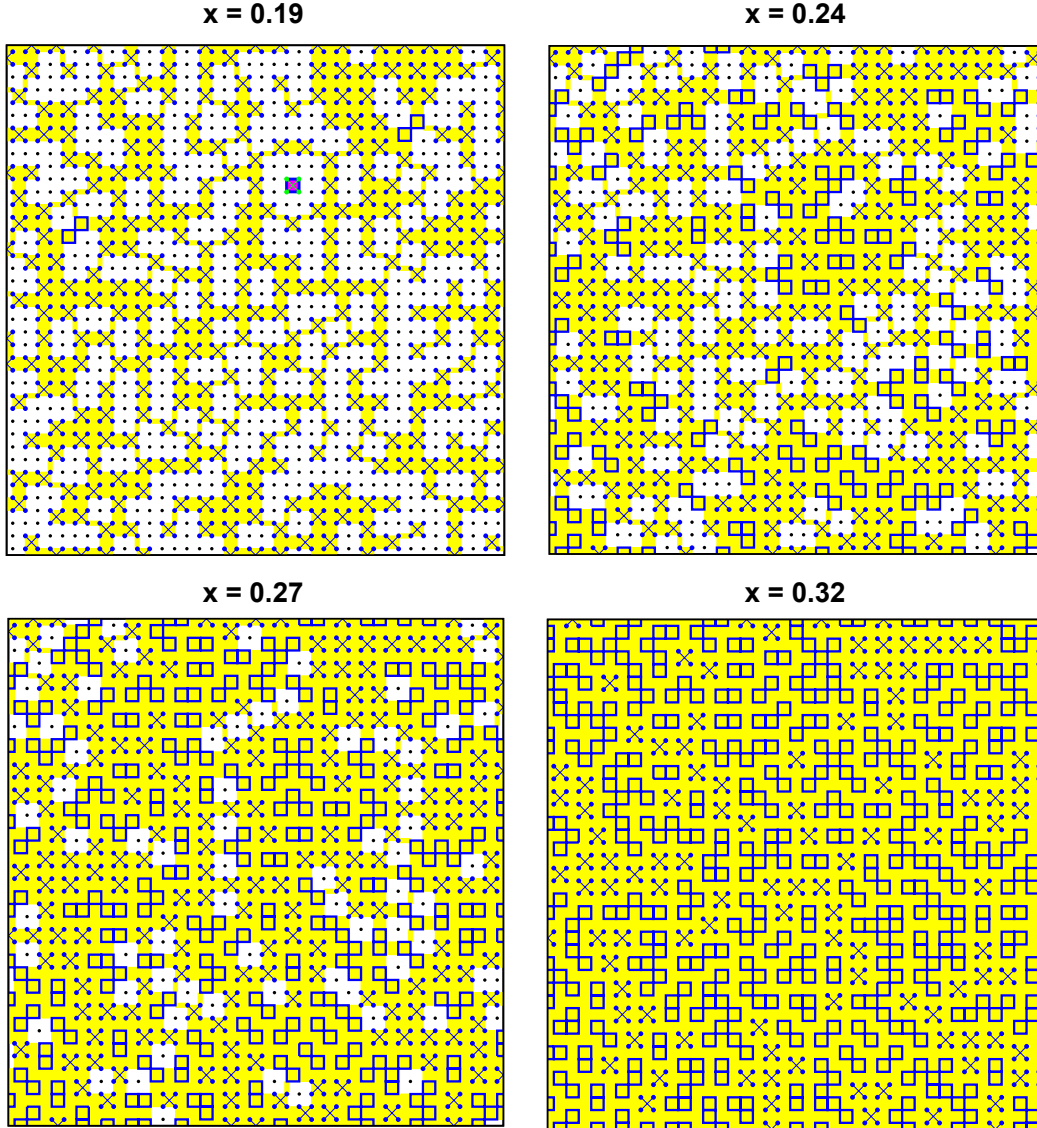


FIG. 11. Plaquette doping of a 40×40 square CuO_2 lattice for dopings $x = 0.19, 0.24, 0.27$, and 0.32 . See the caption of Figure 9 for an explanation of the symbols in this figure. The first plaquette overlap can be seen at 0.19 doping (blue squares). The degeneracy of the two dumbbells states inside each overlapping plaquette has been broken. A frozen dumbbell configuration exists inside each overlapped plaquette. It is not drawn. At 0.27 doping, only isolated spins remain (black dots). At 0.32 doping, there are no localized spins remaining. The crystal is purely metallic. Only one isolated plaquette (blue square with magenta interior) remains at $x = 0.19$ doping. The number of isolated plaquettes never vanishes entirely. Instead, their number becomes of measure zero above $x \approx 0.19$ doping and leads to the vanishing of the pseudogap at $x \approx 0.19$. At $x = 0.32$, the critical current density, J_c , will be close to the Cooper pairing depairing limit since the metallic pathways through the crystal are *not* tenuous. However, there is no interface pairing, leading to $T_c = 0$.

The above eight electronic structural concepts explain a diverse set of normal state cuprate phenomenology as a function of doping by simple *counting* arguments,^{11–14} as we have shown previously. These include (See reference 12 for a videotaped seminar summarizing all of these results.):

- the low and high-temperature normal state resistivity by *counting* the number of overlapped plaquettes and the size of the metallic region.^{12,13}

For $\text{La}_{2-x}\text{Sr}_x\text{CuO}_4$, the fluctuating dumbbells in adjacent CuO_2 layers become decorrelated above ~ 1 K. Phonon modes with character predominantly inside these plaquettes become 2D, leading to the low-temperature linear resistivity term. For the double-chain cuprate, $\text{YBa}_2\text{Cu}_4\text{O}_8$, if the fluctuating dumbbells between adjacent CuO_2 layers are correlated, then these phonons remain 3D, leading to a low-temperature resistivity that is quadratic in temperature, as observed.¹⁵

- the pseudogap and its vanishing at $x \approx 0.19$ doping from *counting* isolated plaquettes (not adjacent to another doped plaquette in the same CuO_2 plane) and their spatial distribution.^{11,12}

As discussed in Appendix B, there is a degeneracy near the Fermi level of the planar states inside an isolated plaquette. The degeneracy is broken by interaction with the environment. A nearby isolated plaquette strongly splits the degeneracy and leads to the pseudogap.

- the “universal” room-temperature thermopower by *counting* the sizes of the insulating AF and metallic regions and taking the weighted average of the thermopower of each region.^{12,14}

Since the room-temperature thermopower of the AF region is $\sim 100 \mu\text{V}/\text{K}$ and the metallic region thermopower is $\sim -10 \mu\text{V}/\text{K}$, there is a rapid decrease in the thermopower as the size of the metallic region increases with doping.

- the STM doping incommensurability by *counting* the size of the metallic regions.^{12,14}
- the energy of the (π, π) neutron spin scattering resonance peak by *counting* the size of the AF regions.^{12,14} The resonance peak arises from the finite spin correlation length of the AF regions.

In this paper, we use exactly the same doped electronic structure described above to explain the superconducting T_c and its evolution with doping. We show that Oxygen atom phonon modes at and adjacent to the interface between the insulating and metallic regions lead to superconductivity. We estimate the magnitude of the electron-phonon coupling and obtain the following:

- a large $T_c \sim 100$ K from phonons (because the range of the electron-phonon coupling near the metal-insulator interface increases from poor metallic screening),
- the observed T_c -dome as a function of hole doping (since the total pairing is the product of the size of the metallic region times the interface size),
- the large T_c changes as a function of the number of CuO_2 layers per unit cell (from inter-layer phonon coupling of the interface O atoms plus inhomogeneous hole doping of the layers),
- the D-wave symmetry of the superconducting Cooper pair wavefunction (also known as the D-wave superconducting gap).

In general, an isotropic S-wave superconducting pair wavefunction is energetically favored over a D-wave pair wavefunction for phonon induced superconductivity. However, the fluctuating dumbbells reduce the S-wave T_c below the D-wave T_c by drastically increasing the Cooper pair electron repulsion.

- the lack of a superconducting T_c isotope effect at optimal doping (due to the random anharmonic potentials of each pairing O atom).
- by overlapping plaquettes, the fluctuating dumbbells become frozen and the S-wave pair wavefunction T_c rises above the D-wave T_c . (Figure 19).

While maintaining the same metallic “footprint” of optimal doping ($x = 0.16$), completely frozen dumbbells lead to an S-wave T_c of ≈ 400 K when the D-wave $T_c = 100$ K (Figure 19).

All the T_c 's in this paper are computed using the strong coupling Eliashberg equations¹⁶ as detailed in Appendix G. These equations include the electron “lifetime” effects that substantially decrease T_c from the simple BCS T_c expression.

These results are shown in the following set of T_c CONCEPTS.

T_c CONCEPT 1: There are two planar O atom phonon modes (one at the metal-AF insulator interface and the other adjacent to the interface on the insulating side) that have longer-range electron coupling due to poor electron screening from the metallic region. See Figure 12. For the remainder of the paper, we use the “effective” single band model for the metallic band.¹⁷ In this model, the planar O atoms are eliminated. The model has a single effective Cu $d_{x^2-y^2}$ orbital per Cu in the CuO_2 plane with an effective hopping to neighboring metallic Cu atoms. The parameters of the band structure are the Cu $d_{x^2-y^2}$ orbital energy and the hopping terms (Table II, Appendix F).

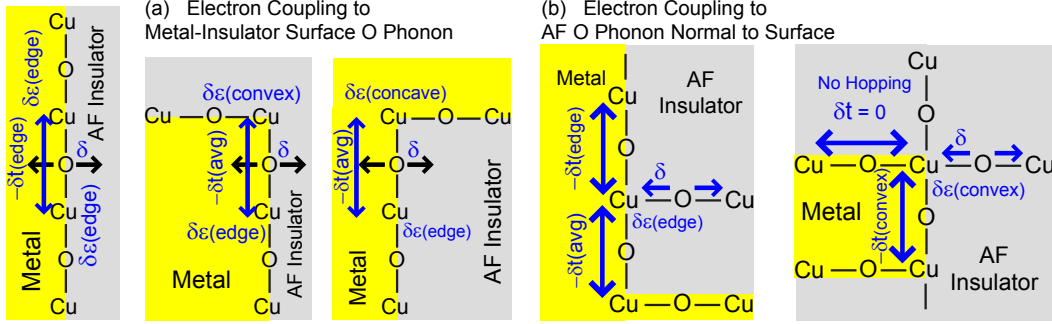


FIG. 12. (a) The planar O atom phonon mode at the metal-insulator interface. Its displacement is planar and normal to the Cu – O – Cu along the metal-insulator interface. Displacement by δ leads to changes to the neighboring interface Cu $d_{x^2-y^2}$ orbital energy by $\delta\epsilon$ ($\delta\epsilon > 0$). There are three kinds of Cu atoms, edge, convex, and concave. Similarly, there is a change in the Cu to Cu hopping matrix element $-\delta t$ ($\delta t > 0$). We choose δt to equal the average of the δt at each Cu. (b) The planar O atom phonon mode in the insulating region adjacent to the metal-insulator interface. The displacement is planar and normal to the metal-insulator interface. The $\delta\epsilon$ and δt are defined in the same way as in (a). There is a $\delta\epsilon$ for the metallic Cu closest to the O atom and two $-\delta t$ for hopping to neighboring metallic Cu sites. The metallic screening of the O atom charge is not strong because it resides in the insulating AF region. Hence, the two δt are large. In this paper, the vibrational energy of these two phonon modes is set to 60 meV.¹⁸ See Table III.

T_c CONCEPT 2: The typical magnitude of the electron-phonon coupling matrix element, g , is the geometric mean¹⁶ of the Debye energy, ω_D , and the Fermi energy, E_F , or $g = \sqrt{\omega_D E_F}$. The derivation is given in Appendix D. For $0.02 \text{ eV} < \omega_D < 0.1 \text{ eV}$ and $E_F = 1 \text{ eV}$, we find $0.14 \text{ eV} < g < 0.32 \text{ eV}$. All T_c results in this paper use electron-phonon coupling parameters in this range.

T_c CONCEPT 3: **The potential energy of each O atom in Figure 12 is strongly anharmonic due to the difference of the electron screening in the metallic and insulating regions.** See Figure 13. In fact, the phonon mode shown in Figure 12a is anharmonic even without a nearby metal-insulator boundary. The “floppiness” of the bonding of a linear chain (here, the planar Cu–O–Cu chain) has been emphasized by Phillips,¹⁹ and seen by neutron scattering (the F atom²⁰ in ScF₃ and the Ag atom²¹ in Ag₂O). However, without the metal-insulator boundary, reflection symmetry would force the electron-phonon coupling for this mode to be zero.

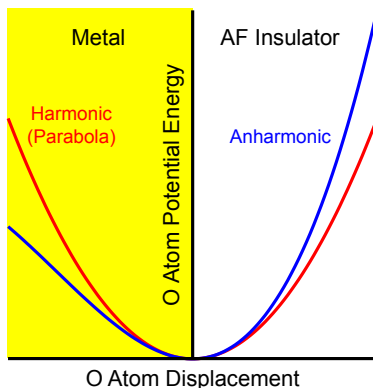


FIG. 13. Anharmonicity of the O atom phonon mode in Figure 12a due to the difference of the electron screening in the metallic and insulating regions. For Figure 12b, the yellow overlay is shifted to the left.

T_c CONCEPT 4: **Near optimal doping, $x \approx 0.16$, there is no T_c isotope effect.** Harmonic potentials have no isotope variation of the superconducting pairing strength because the pairing is inversely proportional to $M\omega^2$ where M is the O atom mass and ω is the angular frequency of the phonon mode. For a derivation of this result, substitute $g = \sqrt{(\hbar/M\omega)}\nabla V$ into the pairing coupling in Figure 14b, where V is the electron potential. Since $M\omega^2 = K$, where K is the spring constant, there is no pairing isotope effect. For anharmonic potentials, the phonon pairing strength becomes dependent on the isotope mass.²² Anharmonic potentials can decrease or increase the T_c isotope effect depending on the details of the anharmonicity.^{23–25} Near optimal doping, the metallic and insulating environments for each O atom phonon is random, leading to an average isotope effect of zero, as observed.^{26,27} The O atom environment becomes less random at lower dopings, as seen in Figure 9. Hence, the isotope effect appears at low dopings.^{26,27}

T_c CONCEPT 5: Cooper pairing from phonons is maximally phase coherent for an isotropic S-wave pair wavefunction because the sign of the pairing matrix element in Figure 14 is always negative. However, a D-wave pair wavefunction is observed for cuprates. It appears *prima facie* that phonons cannot be responsible for superconductivity in cuprates. Since Cooper pairs are comprised of two electrons in time-reversed states, the sign of the Cooper pair scattering is always *negative* and of the form $\sim (-)|g|^2/\hbar\omega_{ph}$,^{28,29} where g is the matrix element to emit a phonon and $\hbar\omega_{ph}$ is the energy of the phonon mode. See Figure 14. Hence, the lowest energy superconducting pairing wavefunction is a linear superposition of Cooper pairs with the *same* sign. It is called the isotropic ‘‘S-wave’’ state. In theory, the pair Coulomb repulsion, μ , could suppress the S-wave state and lead to a D-wave state because μ cancels out of T_c when performing the angular integral around the D-wave pair wavefunction. However, the electrons in a pair can couple via a phonon while avoiding each other (due to retardation of phonons). The ‘‘effective’’ repulsion, μ^* , known as the Morel-Anderson pseudopotential^{16,28–32} is too small to raise the D-wave T_c higher than the S-wave T_c . Unless there is a mechanism for drastically increasing μ^* , any phonon model for cuprate superconductivity is bound to fail to obtain the correct superconducting pair wavefunction. We show in T_c CONCEPT 6 that the fluctuating dumbbells in Figure 5 increase μ^* to $\mu^* \sim \mu$, leading to a D-wave pairing wavefunction.

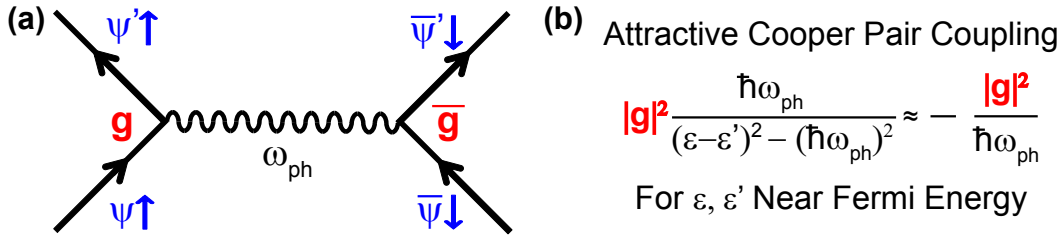


FIG. 14. The scattering matrix element between two Cooper pairs $(\psi \uparrow, \bar{\psi} \downarrow)$ and $(\psi' \uparrow, \bar{\psi}' \downarrow)$ with the exchange of a phonon. The two electrons in each pair are time-reversed partners. The symbol \bar{x} means the complex conjugate of x . For scatterings in the vicinity of the Fermi level, the matrix element is always negative, leading to a superconducting pair wavefunction that is a linear superposition of Cooper pairs with the same sign. Such a pair wavefunction is called isotropic S-wave. Unfortunately, it is known that the cuprate pair wavefunction changes sign and is of D-wave form (more specifically, of $d_{x^2-y^2}$ form). See T_c CONCEPT 6 for a resolution to the problem.

T_c CONCEPT 6: The fluctuating dumbbells suppress the S-wave pairing wavefunction and lead to a D-wave pairing wavefunction. See Figure 15. The expression for the Morel-Anderson Coulomb pseudopotential,^{16,28–32} μ^* , is shown in Figure 15. It depends on the ratio of the Coulomb and phonon energy scales, $\omega_{Coul}/\omega_{phonon}$. Since this ratio is large, μ^* is small, leading to an S-wave pair wavefunction rather than the experimentally observed D-wave pair wavefunction.³³ The fluctuating dumbbell frequency, $\omega_{Dumbbell}$, is of the same order as ω_{phonon} because of the dynamic Jahn-Teller distortion of the planar O atoms in Figure 5. The O atom distortion disrupts the metallic screening of the Coulomb repulsion, and thereby increases μ^* as shown in Figure 15. In essence, $\omega_{Dumbbell}$ substitutes for ω_{Coul} in the expression for μ^* . When $\mu^* \sim \mu$, a D-wave pair wavefunction is formed.

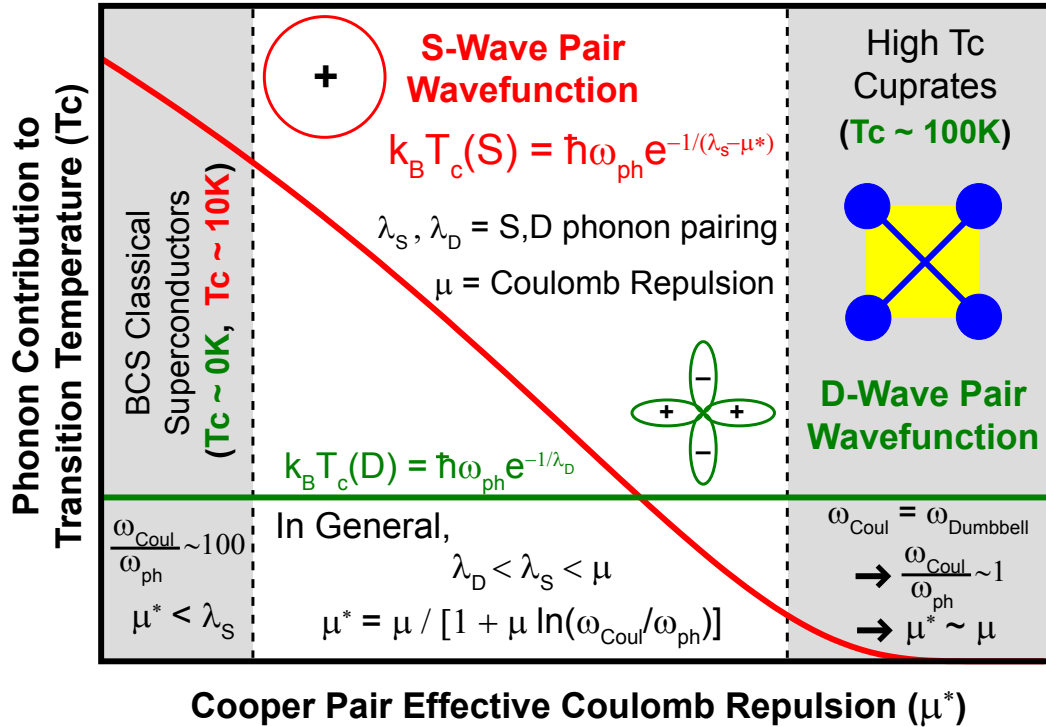


FIG. 15. Evolution of the S-wave and D-wave superconducting pairing wavefunctions as a function of the Coulomb pseudopotential, μ^* . Typically, μ^* is small, leading to S-wave pairing as seen on the left-side of the figure. The fluctuating dumbbells raise μ^* to $\mu^* \sim \mu$ by disrupting the metallic electrons from screening the bare Coulomb repulsion, μ . As μ^* increases, the S-wave T_c decreases while the D-wave T_c remains unchanged as shown in the red and green T_c expressions for S and D-wave, respectively. As μ^* approaches the “bare” Coulomb repulsion, μ , the D-wave T_c becomes the favored pair symmetry for the superconductor. The right-side of the figure applies to cuprates.

T_c CONCEPT 7: Interface O atom phonon pairing explains the experimental T_c domes. Figure 16 shows the calculated T_c -domes versus experiment as a function of doping for different cuprates using the phonon modes from Figure 12 and the electron-phonon couplings estimated in T_c CONCEPT 2. All three computed D-wave T_c domes were obtained from the strong-coupling Eliashberg equations for T_c .^{16,34,35} Other phonon modes also contribute to T_c . These phonons primarily reduce the magnitude of T_c due to their contribution to electron pair “lifetime effects” (strictly speaking, the “wavefunction renormalization effects”). The effect of all the phonon modes on T_c are included in our computations. All the details of the band structure, the interface O phonon coupling parameters, and the inclusion of the remaining phonons into the Eliashberg calculations are described in appendices F and G. We intentionally chose our parameters to be simple and conceptual. We did not attempt to fit the experimental points exactly. Our goal is to demonstrate that reasonable electron-phonon couplings and our proposed inhomogeneous cuprate electronic structure are sufficient to understand the experimental T_c -domes.

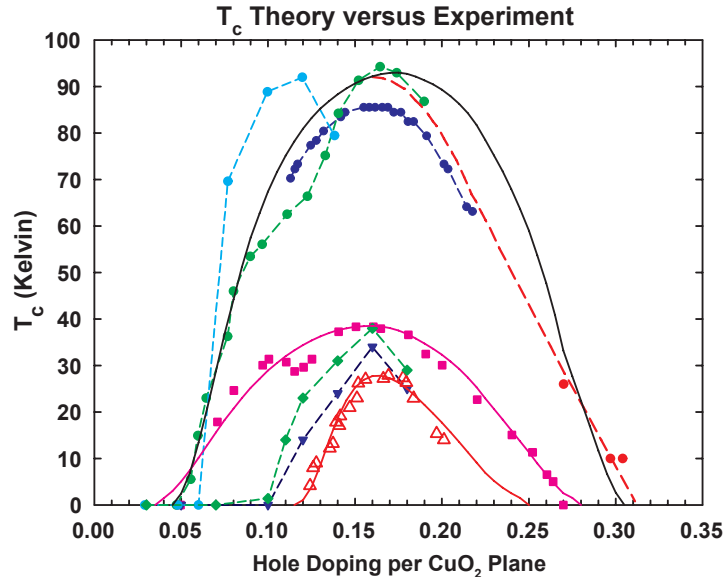


FIG. 16. Comparison of Experimental and Computed T_c -domes. $\text{Bi}_2\text{Sr}_2\text{CaCu}_2\text{O}_{8+\delta}$ (light blue solid circles³⁶), $\text{YBa}_2\text{Cu}_3\text{O}_{7-\delta}$ (green circles³⁷), $\text{Y}_{1-y}\text{Ca}_y\text{Ba}_2\text{Cu}_3\text{O}_{7-\delta}$ (dark blue circles³⁸), $\text{La}_{2-x}\text{Sr}_x\text{CuO}_4$ (magenta squares³⁹), $\text{Bi}_2\text{Sr}_2\text{CuO}_{6+\delta}$ (green diamonds⁴⁰ and solid blue triangles,¹⁷) 6% Zn doped $\text{YBa}_2(\text{Cu}_{0.94}\text{Zn}_{0.06})_3\text{O}_{7-\delta}$ (open red triangles³⁸), and $\text{Tl}_2\text{Ba}_2\text{CuO}_{6+\delta}$ (solid red circles^{41,42}). The dashed red line is the proposed $\text{Tl}_2\text{Ba}_2\text{CuO}_{6+\delta}$ curve by Hussey et al.^{41,42} The solid black, magenta, and red lines are computed. All parameters are described in Appendix F.

T_c CONCEPT 8: The experimental variation of T_c with the number of CuO_2 layers per unit cell is due to interlayer coupling of the interface O atom phonons and the nonuniform hole doping between layers. Since the O atom phonons near the metal-insulator interface are longer-ranged, they couple to adjacent CuO_2 planes. Hence, there is a strong dependence of T_c on the number of CuO_2 layers per unit cell. In addition, the Cu Knight shift measurements of Mukuda et al.² have shown that the hole doping is not the same in each CuO_2 layer. The computed T_c as a function of the number of CuO_2 layers is shown in Figure 17.

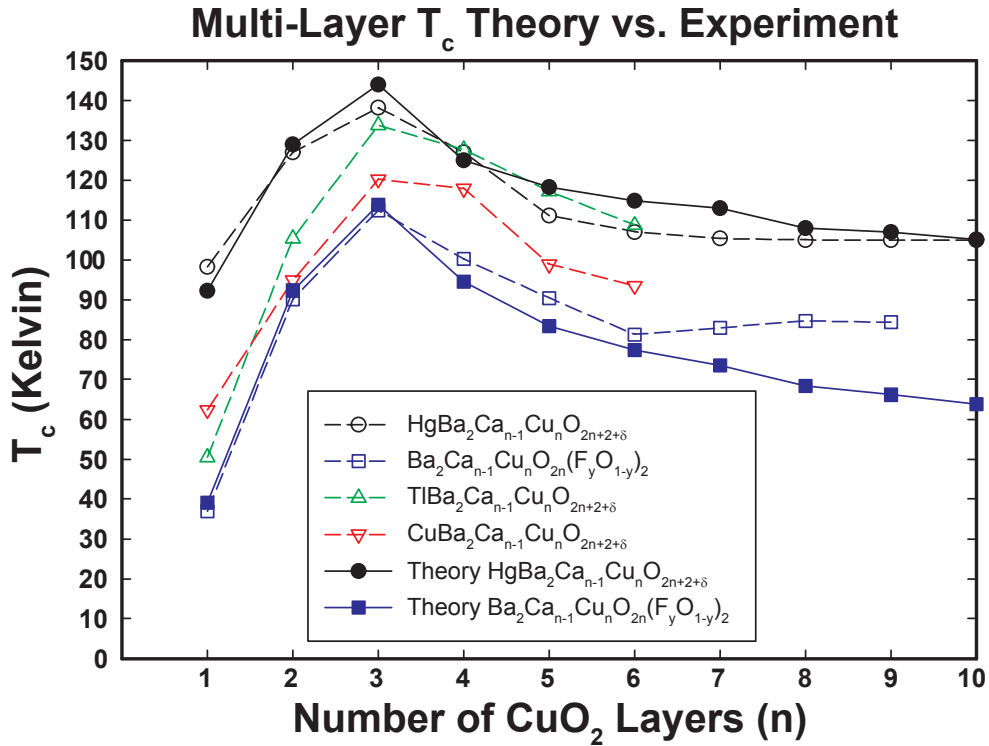


FIG. 17. Comparison of the computed and experimental T_c as a function of CuO_2 layers per unit cell. The experimental data points (open symbols and dashed lines) are from Mukuda et al.² Two theoretical T_c curves are shown (solid symbols and solid lines). All parameters, including the hole dopings in each CuO_2 layer, are in Appendix F. The generalization of the Eliashberg equations for one CuO_2 plane to multi-layers is described in Appendix G 4. If the hole doping in each layer was the same, then the computed T_c curve would monotonically increase with the number of layers, n , and saturate for large n . Since the hole doping for the inner layers is less than the hole doping on the outermost layers (see Table V in Appendix F), there are fewer interface O atom phonons that contribute to the high T_c in the inner layers. The maximum T_c occurs at three layers.

T_c CONCEPT 9: The D-wave T_c values computed in Figures 16 and 17 are weakly dependent on the orbital energy change, $\delta\epsilon$, and strongly dependent on the hopping energy change, δt . See Table I for the change in T_c at optimal doping of $x = 0.16$ for the computed black, red, and magenta curves in Figure 16.

TABLE I. The change in the T_c at optimal doping ($x = 0.16$) for the three computed curves in Figure 16. The orbital energy parameter, $\delta\epsilon$, and the hopping energy parameter, δt , are each changed by 0% and $\pm 10\%$ from their initial values found in Appendix F. In appendices G 2 a and G 2 b, the $\delta\epsilon$ terms lead to a more isotropic electron-phonon pairing, and the δt terms are more anisotropic. For a D-wave T_c , an isotropic electron-phonon pairing does not contribute to T_c . In the fourth column (red curve), $\delta\epsilon = 0$ (see Appendix F). Hence, changes to $\delta\epsilon$ do not affect T_c .

Change in ($\delta\epsilon, \delta t$)	Black Curve YBa ₂ Cu ₃ O _{7-δ}	Magenta Curve La _{2-x} Sr _x CuO ₄	Red Curve YBa ₂ (Cu _{0.94} Zn _{0.06}) ₃ O _{7-δ}
(0%, 0%)	92.2 K	38.5 K	27.7 K
(0%, -10%)	83.1 K	30.7 K	19.9 K
(0%, +10%)	100.0 K	46.3 K	35.6 K
(-10%, 0%)	93.6 K	39.4 K	27.7 K
(-10%, -10%)	84.7 K	31.3 K	19.9 K
(-10%, +10%)	101.1 K	47.5 K	35.6 K
(+10%, 0%)	90.5 K	37.5 K	27.7 K
(+10%, -10%)	81.4 K	30.1 K	19.9 K
(+10%, +10%)	98.5 K	45.0 K	35.6 K

From Table I, a 10% increase in $\delta\epsilon$ always decreases the D-wave T_c by $\approx 2 - 3\%$. A $\pm 10\%$ change in δt leads to $\approx \pm 10 - 30\%$ change in the D-wave T_c . In appendices G 2 a and G 2 b, the exact dependence of the electron-phonon pairing parameter, λ , is derived. The contribution of $\delta\epsilon$ to λ is approximately isotropic around the Fermi surface leading to a weak dependence of the D-wave T_c on changes in $\delta\epsilon$. In contrast, an S-wave pairing symmetry T_c depends strongly on both $\delta\epsilon$ and δt . The weak dependence of the D-wave T_c on $\delta\epsilon$ implies our choices for the $\delta\epsilon$ parameters for the T_c curves in Figures 16 and 17 are not accurately fitted by the experimental T_c data. The uncertainty in the magnitude of $\delta\epsilon$ leads to an S-wave T_c range from $\approx 270 - 400$ K due to dopant “crowding,” as shown next.

T_c CONCEPT 10: **Overlapping plaquettes (“crowding” the dopants) freeze the dumbbells, decrease the Coulomb pseudopotential, μ^* , and thereby raise the S-wave T_c .** If the same metallic “footprint” can be maintained, then there is no change in the phonon pairing. Only μ^* is reduced (see Figure 15). If all the dumbbells can be frozen, then from Figures 14 and 15, the S-wave T_c will be larger than the D-wave T_c . Figure 18 shows how two plaquettes with fluctuating dumbbells can be crowded by adding an additional dopant (Sr in the figure) while retaining exactly the same metallic footprint. For random doping, there will always exist adjacent plaquette pairs as shown in Figure 18c that cannot be overlapped by another plaquette within the existing metallic footprint. There are two ways to obtain an optimally doped metallic footprint and freeze 100% of the dumbbells. First, dope “dominoes” (adjacent pairs of plaquettes as in Figure 18a and b). Second, dope to less than optimum doping. Next, crowd all of the plaquettes in such a way as to end up with an optimally doped metallic footprint and 100% frozen dumbbells.

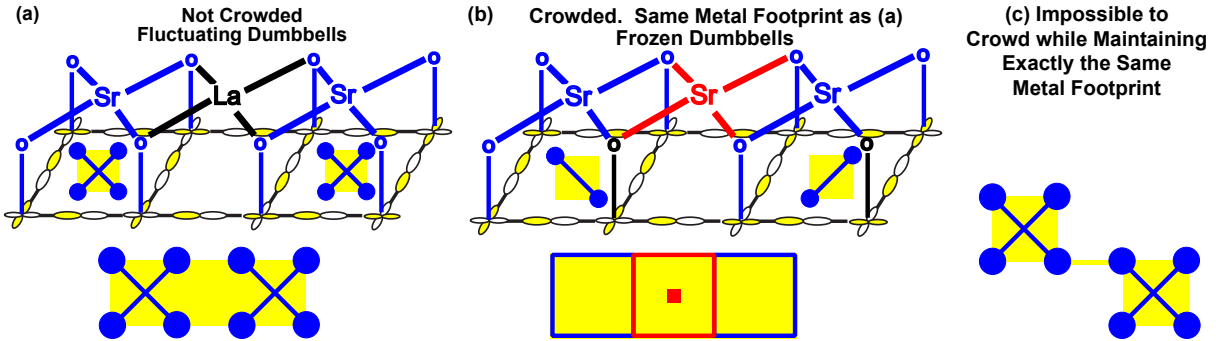


FIG. 18. (a) Two non-overlapped plaquettes with their fluctuating dumbbells and their metallic region (yellow) for the case of Sr dopants in $\text{La}_{2-x}\text{Sr}_x\text{CuO}_4$. The bottom schematic shows the fluctuating dumbbells as crosses and the metallic region in yellow. (b) Adding a Sr dopant between the two plaquettes freezes the two fluctuating dumbbells while maintaining exactly the same metallic footprint. The S-wave T_c increases due to the decrease of the Coulomb pseudopotential while the D-wave T_c remains unchanged. The blue squares in the bottom schematic represent the frozen dumbbells. The added Sr dopant is shown by the red square. However, any atom that breaks the degeneracy of the dumbbell states will work instead. The yellow metallic overlay is unchanged from (a). The orientation of the frozen dumbbells is arbitrary in the figure because it depends on the environment (not shown). (c) Two adjacent plaquettes that are shifted by one lattice spacing. No plaquette can be added to freeze the dumbbells while maintaining the same metallic footprint.

T_c CONCEPT 11: Crowding dopants while maintaining the optimal doping metallic footprint leads to room temperature S-wave T_c . See Figure 19.

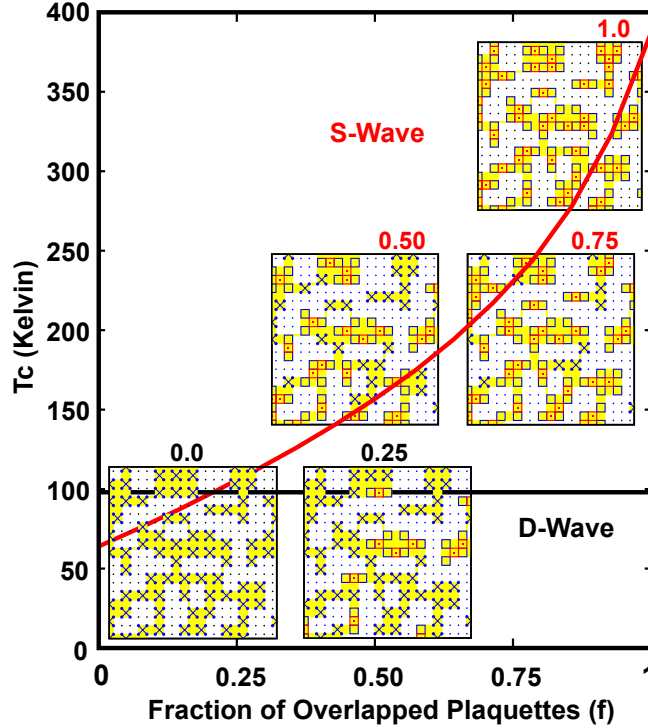


FIG. 19. The S-wave and D-wave T_c 's as a function of overlapped plaquette fraction, f . The insets show the evolution of the frozen dumbbells (blue and red squares) for optimal doping of $x = 0.16$. The metallic footprint is unchanged. The D-wave T_c is constant (the Coulomb pseudopotential, μ^* , has no effect). The maximum S-wave T_c is 387.2 K and the D-wave T_c is 98.0 K. We assume μ^* varies linearly with f , $\mu^*(f, i\omega_n) = \mu_{Fluc}^* F(i\omega_n)(1 - f) + \mu_{BCS}^*$, where $\mu_{Fluc}^* = 7$ (the fluctuating dumbbell μ^*), $\mu_{BCS}^* = 0.1$ (a typical BCS value), and the cutoff $F(i\omega_n) = \omega_{Fluc}^2 / (\omega_n^2 + \omega_{Fluc}^2)$. We set $\omega_{Fluc} = 60$ meV. The Eliashberg imaginary frequency, $i\omega_n$, is defined in Appendix G. In order to achieve 100% frozen dumbbells, “domino” doping as shown in Figures 18a and b was used. We set $\delta\epsilon = \delta t = 0.30, 0.30, 0.15$ eV for Edge, Convex, and Concave orbital and hopping energies, respectively. See the definitions in Figure 12. We used a larger $\delta\epsilon$ than Figure 16 and Appendix F because $\delta\epsilon$ should be greater than δt due to its proximity to the planar O atom. Since the D-wave T_c is weakly dependent on $\delta\epsilon$, our choices in Figure 16 were very conservative. The S-wave T_c values for 100% frozen dumbbells for the black, magenta, and red curves in Figure 16 at optimal doping are 280.1 K, 164.4 K, and 99.0 K, respectively. The corresponding D-wave T_c values are 92.2 K, 38.5 K, and 27.7 K. Hence, the S-wave T_c is in the range of $\approx 280 - 390$ K.

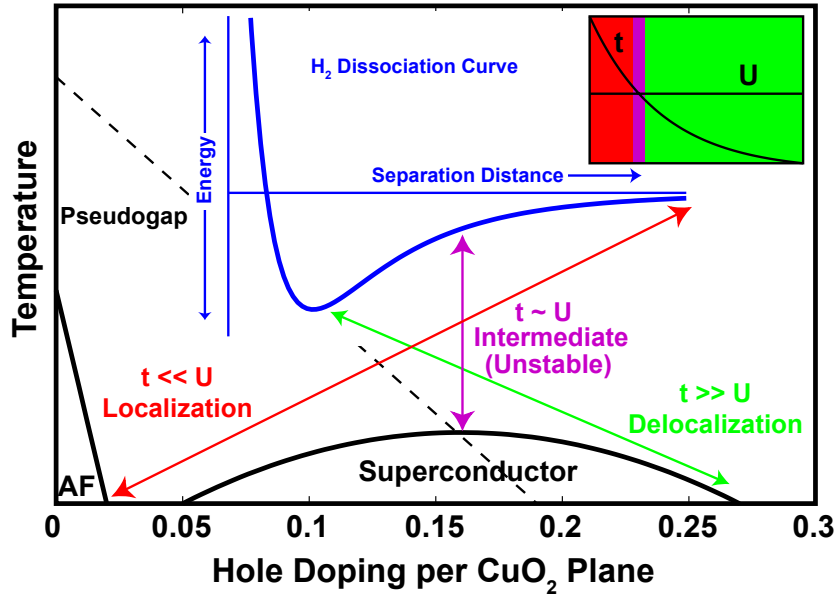


FIG. 20. The iconic H_2 dissociation curve in chemistry (blue inset) and the iconic cuprate phase diagram (larger black figure). Both figures show the regimes of delocalized, intermediate, and localized electronic states. For H_2 , electron delocalization occurs near the equilibrium bond distance of 0.74 \AA , where the effective hopping, t , is larger than the effective Coulomb repulsion, U , of the electrons (see inset in upper right corner). Molecules do *not* exist at the intermediate (magenta) region since the potential is not a local minimum. Similarly, semiconductors can be classified into delocalized (covalent) and localized (ionic) with a sharp transition in-between based upon their Fermi level stabilization at a semiconductor-metal interface.⁴³ In cuprates, the intermediate regime is where the optimal superconducting T_c occurs. In analogy to molecules and semiconductors, we believe cuprates are unstable here, and thereby “phase separate” into delocalized metallic and insulating magnetic AF regions. Finally, we intentionally avoided using the terms “weak correlation” and “strong correlation” in the figure. The word correlation means different things to different scientists. For chemists, the delocalized region ($t \gg U$) is “weak electron correlation,” and the localized region ($t \ll U$) is “strong electron correlation.” For physicists, cuprates are considered a “strong correlation” problem.

In Figure 20, the ground state electronic wavefunction of H_2 at the equilibrium bond separation of 0.74 \AA is well approximated by a restricted Hartree-Fock form (a spin up and spin down electron pair occupying the same bonding orbital). In the language of an effective

electron hopping, t , and an onsite Coulomb repulsion, U , this region is represented by $t \gg U$. At dissociation ($t \ll U$), the ground state electronic wavefunction is highly correlated. The wavefunction is large only when there is one electron on each H atom.

From Figure 20, the optimal superconducting T_c of cuprates is at “intermediate” correlation. Molecules do not generally “settle” at intermediate correlation. Since the dopants in cuprates are frozen in at high temperatures, the material avoids intermediate correlation by phase separating on an atomic-scale into a metallic (weak correlation) and an insulating AF (strong correlation) regions.

Atomic-scale inhomogeneity explains three important materials issues about cuprates. First, cuprates “self-dope” to approximately optimal T_c . Since plaquette overlap occurs at $x = 0.187$ doping, we believe it is energetically favorable for dopants to enter the crystal until their plaquettes begin to overlap. Adding further dopants is energetically unfavorable. The change in T_c between optimal doping ($x \approx 0.16$) and plaquette overlap ($x = 0.187$) is $\approx 5\%$. Hence, cuprates “self-dope” to approximately optimal T_c as a consequence of the energetics of overlapping plaquettes.

Second, $\text{YBa}_2\text{Cu}_3\text{O}_{7-\delta}$ cannot be doped past $x \approx 0.23$, as shown in Figure 16. The phenomenon can be understood if it is energetically unfavorable to overlap plaquettes that share an edge (occurring at doping $x = 0.226$). In the earliest days of cuprate superconductivity, materials scientists had difficulty observing superconductivity in $\text{La}_{2-x}\text{Sr}_x\text{CuO}_4$ above ≈ 0.24 doping.⁴⁴ We believe the difficulty was also due to the energetics of overlapping plaquettes with shared edges. Annealing in an O_2 atmosphere solved the $\text{La}_{2-x}\text{Sr}_x\text{CuO}_4$ overdoping problem. However, the problem still remains for $\text{YBa}_2\text{Cu}_3\text{O}_{7-\delta}$.

Third, it is known that a room-temperature thermopower measurement is one of the fastest ways to determine if a cuprate sample is near optimal doping for T_c because the room-temperature thermopower is very close to zero near optimal doping. This peculiar, but useful, observation can be understood because 2D percolation of the metallic region occurs at $x \approx 0.15$ doping. Since the AF region thermopower is large ($\sim +100 \mu\text{V}/\text{K}$) and the metallic thermopower is $\sim -10 \mu\text{V}/\text{K}$ at high overdoping, 2D metallic percolation “shorts out” the AF thermopower and drives the thermopower close to zero near optimal T_c .

Finally, the potential energy curve in the intermediate correlation regime is hard to study for molecules. For H_2 , the equilibrium bond distance is 0.74 \AA . The intermediate correlation

regime is at $\approx 2.0 \text{ \AA}$ bond separation. At this distance, the blue potential energy curve in Figure 20 can only be observed indirectly⁴⁵⁻⁴⁷ because it is not at a local minimum. For H_2 , the ultraviolet spectrum of the vibrational modes (there are 14 discrete level below the continuum) can be fitted to a simple Morse potential to estimate the potential energy as a function of the $H - H$ separation distance. The 10th bond-stretching phonon mode probes the potential energy of the two of H atoms up to $\approx 2.0 \text{ \AA}$.

MATERIALS APPROACHES TO ROOM-TEMPERATURE T_c AND LARGE J_c

There is enormous “latent” T_c residing in the cuprate class of superconductors from converting the D-wave superconducting pairing wavefunction to an S-wave pairing wavefunction. The result is surprising because it has been assumed by most of the high- T_c cuprate community, including the author, that there was something special about the D-wave pairing symmetry that led to $T_c \sim 100 \text{ K}$.

The first thought that comes to mind given our finding is, “With over 200,000 refereed papers³ and 30 years of intensive research in both academia and industry, surely someone overlapped plaquettes, and thereby created a room-temperature S-wave superconductor?”

Our answer is that plaquettes have been overlapped with regularity for 30 years. These materials are all overdoped with doping $x > 0.187$, as shown in Figure 11. Hence, dumbbells have been frozen and the S-wave T_c has increased. However, our calculations find the S-wave T_c remains below the D-wave T_c for reasonable parameter choices. Unfortunately, the optimally doped metallic footprint is not obtained by naive dopant crowding. Instead, the size of the metallic footprint increases and its pairing interface decreases. The right side of the T_c -dome shown in Figure 16 is the result. Even the layer-by-layer Molecular Beam Epitaxy (MBE) of Bozovic et al.⁴⁸ does not control the placement of the dopants in each layer, leading to the same result as above.

While almost everything that can be possibly be suggested for the mechanism for cuprate superconductivity has been suggested in over 200,000 papers (percolation, inhomogeneity, dynamic Jahn-Teller distortions, competing orders, quantum critical points at optimal doping or elsewhere, spin fluctuations, resonating valence bonds, gauge theories, blocked single electron interlayer hopping, stripes, mid-infrared scenarios, polarons, bipolarons, spin polarons, spin bipolarons, preformed Bose-Einstein pairs, spin bags, one-band Hubbard models, three-band Hubbard models, t-J models, t+U models, phonons, magnons, plasmons,

anyons, Hidden Fermi liquids, Marginal Fermi liquids, Nearly Antiferromagnetic Fermi liquids, Gossamer Superconductivity, the Quantum Protectorate, etc.), we believe these ideas have lacked the microscopic detail necessary to guide experimental materials design, and in some instances, may have even led materials scientists down the wrong path.

We have shown above that freezing dumbbells in cuprates leads to room-temperature T_c (see Figure 19). However, the critical current density, J_c , is approximately two orders of magnitude smaller than the theoretical maximum, $J_c \sim 10^{-2} J_{c,\max}$, where $J_{c,\max}$ is the depairing limit for Cooper pairs. J_c is small because the conducting pathway in the CuO_2 planes is *extremely* tenuous (see the discussions in the captions of Figures 4 and 10). For practical engineering, J_c should be at least $\sim 10^{-1} J_{c,\max}$.

In cuprates, T_c can be raised to room-temperature by freezing dumbbells while maintaining the random metallic footprint found at optimal doping. By fabricating wires (a wire is defined as a continuous 1D metallic pathway through the crystal), T_c remains large while J_c increases to at least $\sim 10^{-1} J_{c,\max}$.

Our results lead to the following approaches for achieving higher T_c and J_c . Unless explicitly stated, the bullet points below apply to any type of material (cuprate or non-cuprate).

- *The material should be inhomogeneous with a metallic region and an insulating region.*

The insulating region does not have to be magnetic. However, we believe the antiferromagnetic insulating region helps maintain the sharp metal-insulator boundary seen in cuprates. An ordinary insulator or a semiconductor with a small number of mobile carriers is sufficient to obtain a longer ranged electron-phonon coupling at the interface because there is less electron screening in the semiconducting (or insulating) region compared to the metallic region.

- *The ratio of the number of metallic unit cells on the interface (adjacent to at least one insulating unit cell) to the total number of metallic unit cells must be larger than 20%.*

We use the terms interface and surface interchangeably below.

The number of metallic unit cells on the interface (or surface) must be a large fraction of the total number of metallic unit cells in order for the enhanced electron-phonon pairing at the interface to have an appreciable affect on T_c . From our calculations in

Figure 16, 50% of optimal T_c is obtained when the ratio is $\approx 50\%$, and 25% of optimal T_c occurs when the ratio is $\approx 35\%$. Below a surface metal unit cells to total metal unit cells ratio of 20%, T_c falls off exponentially, and therefore T_c is too low to be useful.

Metallic clusters that are smaller than approximately the coherence length do not contribute to T_c due to thermal fluctuations. The surface metal unit cells to total metal unit cells ratio above should only include surface metal unit cells in extended metallic clusters.

Inhomogeneous materials formed at eutectic points have a surface metal unit cells to total metal unit cells ratio of $\sim 10^{-3}$ or less if the sizes of the metallic and insulating regions are on the order of microns. Standard materials fabrication methods do not lead to sufficient surface atomic sites for high T_c . Inhomogeneity on the atomic-scale is necessary.

It would appear that parallel 1D metallic wires that are one lattice constant wide (equal to one plaquette width in cuprates) would lead to the maximum surface unit cells to total metal unit cells ratio of 100%, and thereby a large T_c increase. We were surprised to discover that at optimal doping of $x = 0.16$, the surface metal unit cells to total metal unit cells ratio is 91% in cuprates.

Increasing the ratio to 100% increases T_c by only $\approx 5\%$ because at higher T_c magnitudes, T_c no longer increases exponentially with the magnitude of the electron-phonon coupling, λ (defined in Appendix G). Instead, T_c scales⁴⁹ as $T_c \sim \sqrt{\lambda}$. A 10% increase in the surface to total metal unit cells ratio increases λ by 10%, leading to a 5% increase in T_c . Hence, there is negligible T_c to be gained by fabricating wires. However, wires lead to large J_c , as discussed below.

In fact, parallel wires that are a few lattice constants in width are bad superconductors because 1D superconductor-normal state thermal fluctuations lead to large resistances below the nominal T_c . By fabricating two (or more) sets of parallel wires that cross each other, the effect of resistive thermal fluctuations in a single wire are suppressed. In the figures below, we show perpendicularly crossed wires in 2D. The same pattern or a different pattern can be used in adjacent layers normal to the 2D wires. Crossing wires in 3D (two or more sets of parallel wires spanning the whole crystal) also leads to high T_c and J_c .

- *Add dopants to an insulating parent compound that leads to metallic regions. Doping a metallic parent compound to create insulating regions will work also. In cuprates, the parent compound is insulating and doping creates metallic regions.*
- *Avoid small disconnected metallic clusters. If they are smaller than the coherence length, they do not contribute to T_c due to thermal fluctuations.*

In cuprates, high T_c can be obtained at very low doping if all the dopants leading to isolated plaquettes and small plaquette clusters are arranged such that a single contiguous metallic cluster is formed. While the T_c may be high, J_c will be low if the size of the metallic region is a small fraction of the total volume of the crystal.

- *Superconducting wires lead to a small increase of T_c and a large increase of J_c .*

Metallic wires lead to a tiny increase in T_c , as discussed in the second bullet above. However, metallic wires increase J_c dramatically (up to a factor of ~ 100) by eliminating the *tortured* conduction pathways shown in Figure 4. For cuprates, optimal T_c doping at $x = 0.16$ is barely above the 2D percolation threshold of $x \approx 0.15$ doping. Hence, the conducting pathways in a single CuO_2 plane are tenuous at optimal doping. Current materials fabrication methods for cuprates have optimized the T_c at the expense of J_c . We find this point to be evidence that despite all the proposals in over 200,000 refereed publications,³ there has been little guidance to the materials synthesis community on what is relevant at the atomic level for optimizing T_c and J_c . See Figure 21.

Crossed metallic wires with varying aspect ratios and widths provide many opportunities for optimizing T_c and J_c for specific applications. For example, wires that are four metallic atoms wide (equal to two adjacent plaquettes in cuprates), would have $\approx 1/2$ the surface to total metal ratio of metallic wires two atoms wide (or one plaquette in cuprates), leading to an $\approx 50\%$ reduction in T_c compared to wires that are two metallic atoms wide. However, J_c increases by a factor of two.

Generally, it is most favorable to fabricate the narrowest wires that are spaced closely together because both T_c and J_c will be large. In addition, interfacial phonon modes will couple to both the closest wire and the next-nearest neighboring wire, leading to further increase in T_c .

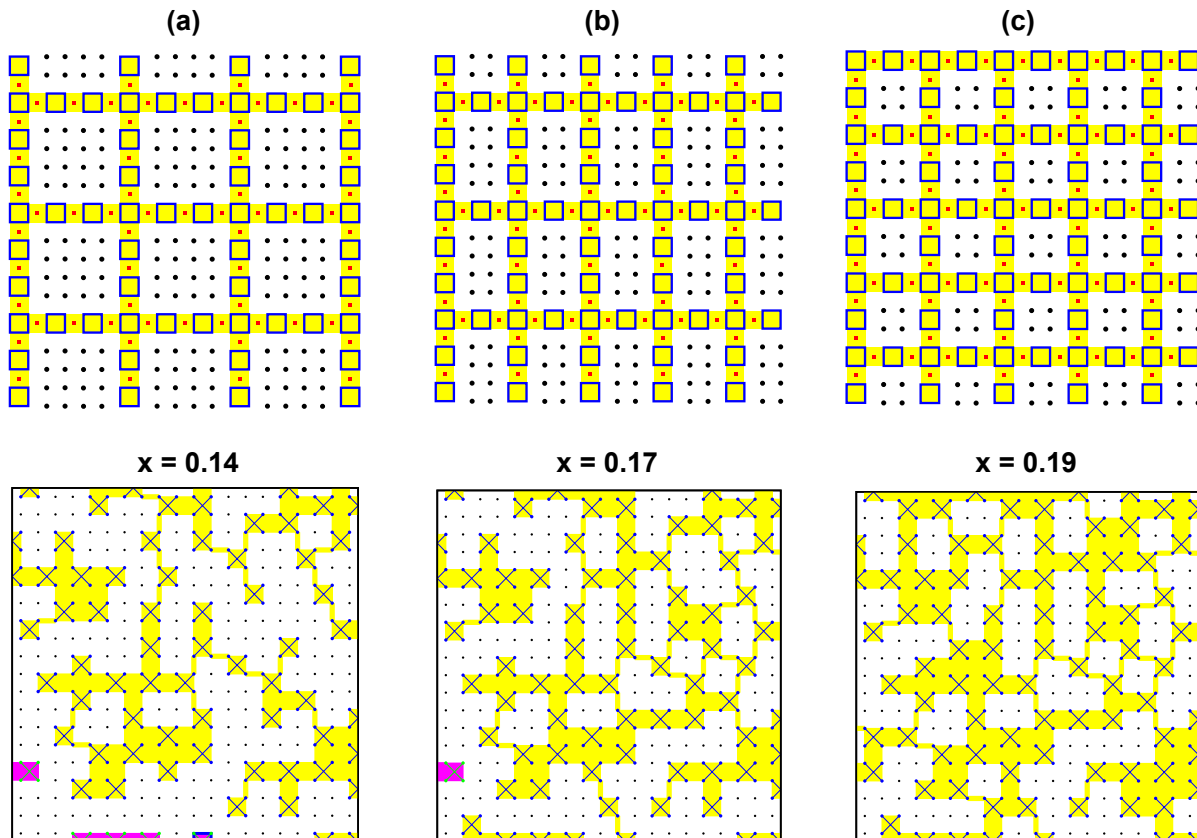


FIG. 21. “Crowded” crossed wires that have high T_c and J_c . The crossed metallic wires are one plaquette in width. The symbols in the metallic wires are defined in Figures 18 and 19, with one change solely for clarity. Here, the added dopant (solid red square) that overlaps two plaquettes (blue squares) does not have a red square boundary. The black circles are undoped AF Cu spins. The first row of (a), (b), and (c) show crossed wires with 4×4 , 2×4 , and 2×2 AF spins, respectively, inside each interior region formed by the perpendicular wires on 20×20 CuO_2 lattices. The second row shows the corresponding lattices that are randomly doped to approximately the same fraction of metallic unit cells as the crossed wires in the first row ($x = 0.14, 0.17$, and 0.19). Larger 40×40 lattice figures for the second row can be found in Figures S14, S17, and S19 at the end of the paper. The T_c for each wire configuration is approximately equal to the S-wave T_c for an optimally doped system since the ratio of the surface metal cells to the total metal cells is 68%, 75%, and 80% for (a), (b), and (c), respectively. The ratio is $\approx 91\%$ at random optimal doping. The T_c 's of (a), (b), and (c) are approximately 12%, 8%, and 6% less than the S-wave T_c at optimal doping. The J_c for (a) is $(1/2)J_{c,max}$, where $J_{c,max}$ is the theoretical maximum of $\sim 2 \times 10^7$ A/cm² for $\text{YBa}_2\text{Cu}_3\text{O}_{7-\delta}$. In (b), $J_c = (1/3)J_{c,max}$ and $(1/2)J_{c,max}$ for currents along the x and y-axes, respectively. For (c), $J_c = (1/3)J_{c,max}$. Random optimal doping leads to $J_c \sim 10^{-2}J_{c,max}$ (see Figure 4).

For cuprates, the narrowest wire is one plaquette width (see Figure 2). Other materials will have a different minimum width scale for wires.

- *Atomic-Scale metal-insulator inhomogeneity in a 3D material leads to a high- T_c 3D S-wave pairing wavefunction. A 3D material is more stable against defects and grain boundaries.*

- *Metallic and insulating regions provide new opportunities for pinning magnetic flux.*

Strong pinning of magnetic flux lines in superconductors is necessary to obtain large critical current densities, J_c . Insulating “pockets” surrounded by metallic region are energetically favorable for magnetic flux to penetrate. The flux can be strongly bound inside these insulating regions by adding further pinning centers to the insulating region. Examples of insulating pockets are shown in Figure 21.

- *In cuprates, freeze the fluctuating dumbbells in non-overlapping plaquettes while maintaining a metallic footprint with a large surface metallic unit cells to total metallic unit cells ratio.*

The ratio of the isotropic S-wave pairing wavefunction T_c to the corresponding D-wave T_c is $\approx 2.8 - 4$ (see Figure 19).

- *In cuprates, fluctuating dumbbells in non-overlapping plaquettes can be frozen by breaking the symmetry inside each plaquette by an atomic substitution into the CuO_2 plane, atomic substitution out of the CuO_2 plane (such as the apical O atom sites), or interstitial atoms, as shown in Figure 22.*

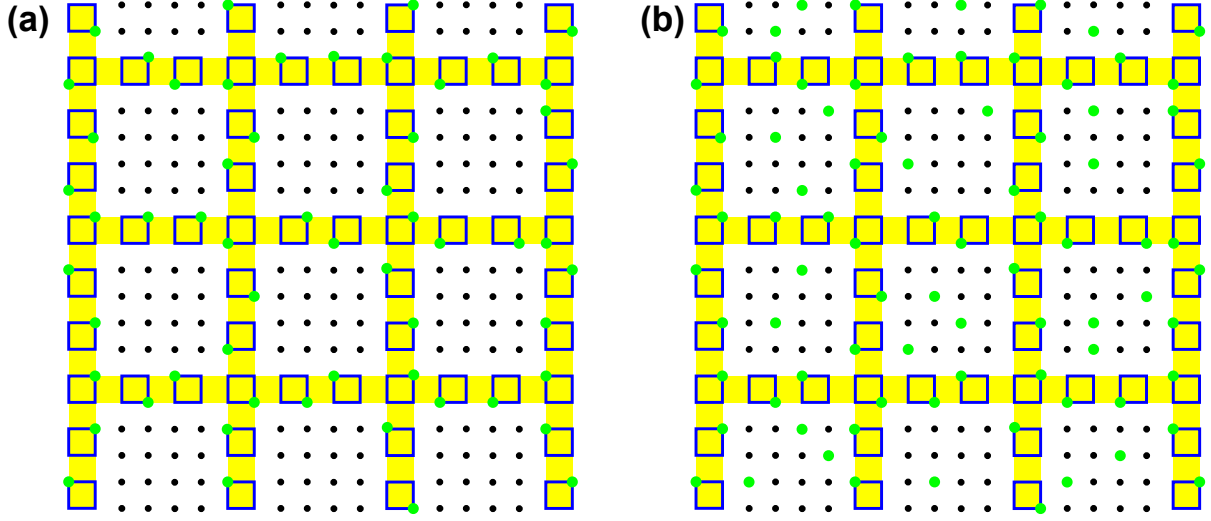


FIG. 22. Atomic substitution inside non-overlapping plaquettes can freeze dumbbells by breaking the dumbbell degeneracy inside the plaquette. (a) and (b) show 20×20 CuO_2 lattices with 4×4 AF interiors and crossing metallic wires one plaquette in width. In (a), the green dots show random atomic substitutions or interstitial atoms inside the plaquettes. The atomic substitutions may occur at the Cu atom in the plaquette (shown here), the O atoms inside the CuO_2 plaquette, or the apical O atom sites. The O atoms are not shown in the figure. (b), green dots representing atomic substitutions or interstitial atoms in the insulating AF region are also shown. So long as these green dots do not disrupt the insulating behavior of these regions, the superconductivity will not be disturbed. (b) may be easier to engineer than (a) because the green dots are dispersed more randomly.

CONCLUSIONS

We have constructed a microscopic theory of cuprate superconductivity from the results of the chemist’s ab initio *hybrid* density functional methods (DFT). Hybrid DFT finds a *localized* out-of-the-CuO₂ hole is formed around a negatively charged dopant. The doped hole resides in a four-Cu-site plaquette. The out-of-plane hole destroys the antiferromagnetism inside the plaquette and creates a tiny piece of metal there. Hence, the crystal is inhomogeneous on the atomic-scale with metallic and insulating regions.

In contrast, the physicist’s DFT methods (LDA and PBE) find a *delocalized* hole residing in the CuO₂ planes as a consequence of doping. We argue that the chemist’s result is to be trusted over the physicist’s result because it corrects the spurious self-Coulomb repulsion of the electrons found in the physicist’s density functionals.

Due to dopant-dopant Coulomb repulsion, doped plaquettes do not overlap unless the doping is sufficiently high that overlap cannot be avoided. Non-overlapping plaquettes have a dynamic Jahn-Teller distortion of the out-of-the-plane hole that we call a “fluctuating dumbbell”. The dumbbells inside an overlapped plaquette become static Jahn-Teller distortions, or “frozen”.

The above model explains a vast swath of normal state phenomenology using simple counting of the sizes of the metallic region, the insulating AF region, and the number of fluctuating and frozen dumbbells. We show that superconducting pairing arises from planar Oxygen atoms near the interface between the metallic and insulating regions. These planar O atom phonon modes explain the large $T_c \sim 100$ K, the T_c -dome as a function of doping, the changes in T_c as a function of the number of CuO₂ layers per unit cell, the lack of a T_c isotope effect at optimal doping, and the D-wave superconducting pairing wavefunction (or superconducting gap symmetry).

Generally, with phonon superconducting pairing, an isotropic S-wave pairing wavefunction is favored over a D-wave pairing wavefunction. However, we show that the fluctuating dumbbells drastically raise the Cooper pair Coulomb repulsion, leading to the observed D-wave pairing wavefunction. By overlapping the plaquettes and freezing the dumbbells, the S-wave pairing wavefunction becomes favored over the D-wave pairing wavefunction. We show that the S-wave T_c is in the range of $\approx 280 - 390$ K when the D-wave $T_c \approx 100$ K.

Finally, we summarize the materials characteristics that are relevant for fabricating room-temperature superconductors and high current densities.

Acknowledgments

*“In Ogg’s theory it was his intent
That the current keep flowing, once sent;
So to save himself trouble,
He put them in double,
And instead of stopping, it went.”*
George Gamov⁵⁰

The author thanks Professor Philip B. Allen for a discussion on estimating the electron-phonon coupling magnitude. The author is grateful to Professors William A. Goddard III and Carver A. Mead for discussions and encouragement.

* jamil@caltech.edu

- ¹ Schilling, A., Cantoni, M., Guo, J. D. & Ott, H. R. Superconductivity Above 130 K in the Hg-Ba-Ca-Cu-O System. *Nature* **363**, 56–58 (1993). URL <http://dx.doi.org/10.1038/363056a0>.
- ² Mukuda, H., Shimizu, S., Iyo, A. & Kitaoka, Y. High-*t_c* superconductivity and antiferromagnetism in multilayered copper oxides—a new paradigm of superconducting mechanism. *Journal of the Physical Society of Japan* **81**, 011008 (2012). URL <http://dx.doi.org/10.1143/JPSJ.81.011008>.
- ³ Mann, A. Still in suspense. *Nature* **475**, 280–282 (2011). URL <http://dx.doi.org/10.1038/475280a>.
- ⁴ Perdew, J. P., Burke, K. & Ernzerhof, M. Generalized gradient approximation made simple. *Phys. Rev. Lett.* **77**, 3865–3868 (1996). URL <http://link.aps.org/doi/10.1103/PhysRevLett.77.3865>.
- ⁵ Yu, J. J., Freeman, A. J. & Xu, J. H. Electronically driven instabilities and superconductivity in the layered $\text{la}_2\text{-xbaxcuo}_4$ perovskites. *Physical Review Letters* **58**, 1035–1037 (1987). URL <http://link.aps.org/doi/10.1103/PhysRevLett.58.1035>.
- ⁶ Mattheiss, L. F. Electronic band properties and superconductivity in $\text{la}_2\text{-yxycuo}_4$. *Physical Review Letters* **58**, 1028–1030 (1987). URL <http://link.aps.org/doi/10.1103/PhysRevLett.58.1028>.

- ⁷ Pickett, W. E. Electronic-structure of the high-temperature oxide superconductors. *Reviews of Modern Physics* **61**, 433–512 (1989). URL <http://link.aps.org/doi/10.1103/RevModPhys.61.433>.
- ⁸ Perdew, J. P. & Zunger, A. Self-interaction correction to density-functional approximations for many-electron systems. *Phys. Rev. B* **23**, 5048–5079 (1981). URL <http://link.aps.org/doi/10.1103/PhysRevB.23.5048>.
- ⁹ Perry, J. K., Tahir-Kheli, J. & Goddard, W. A. Antiferromagnetic band structure of La_2CuO_4 : Becke-3-lee-yang-parr calculations. *Physical Review B* **63**, 144510 (2001). URL <http://link.aps.org/doi/10.1103/PhysRevB.63.144510>.
- ¹⁰ Perry, J. K., Tahir-Kheli, J. & Goddard, W. A. Ab initio evidence for the formation of impurity $d_{3z^2-r^2}$ holes in doped $\text{La}_2\text{-xSr}_x\text{CuO}_4$. *Physical Review B* **65**, 144501 (2002). URL <http://link.aps.org/doi/10.1103/PhysRevB.65.144501>.
- ¹¹ Tahir-Kheli, J. & Goddard, W. A. Origin of the pseudogap in high-temperature cuprate superconductors. *Journal of Physical Chemistry Letters* **2**, 2326–2330 (2011). URL <http://dx.doi.org/10.1021/jz200916t>.
- ¹² Tahir-Kheli, J. Understanding superconductivity in cuprates. *Caltech YouTube Channel* (2015). URL https://www.youtube.com/watch?v=Dq2uIzS_U9k.
- ¹³ Tahir-Kheli, J. Resistance of high-temperature cuprate superconductors. *New Journal of Physics* **15**, 073020 (2013). URL <http://stacks.iop.org/1367-2630/15/i=7/a=073020>.
- ¹⁴ Tahir-Kheli, J. & Goddard, W. A. Universal properties of cuprate superconductors: T_c phase diagram, room-temperature thermopower, neutron spin resonance, and stm incommensurability explained in terms of chiral plaquette pairing. *Journal of Physical Chemistry Letters* **1**, 1290–1295 (2010). URL <http://dx.doi.org/10.1021/jz100265k>.
- ¹⁵ Proust, C., Vignolle, B., Levallois, J., Adachi, S. & Hussey, N. E. Fermi liquid behavior of the in-plane resistivity in the pseudogap state of $\text{YBa}_2\text{Cu}_4\text{O}_8$. *Proceedings of the National Academy of Sciences* **113**, 13654–13659 (2016). URL <http://www.pnas.org/content/113/48/13654.abstract>.
- ¹⁶ Allen, P. B. & Mitrovic, B. Theory of superconducting t_c . In Ehrenreich, H., Seitz, F. & Turnbull, D. (eds.) *Solid State Physics, Advances in Research and Applications*, vol. 37, 1–92 (Academic Press, New York, 1982).
- ¹⁷ Hashimoto, M. *et al.* Doping evolution of the electronic structure in the single-layer cuprate

- $\text{Bi}_2\text{Sr}_{2-x}\text{La}_x\text{CuO}_{6+\delta}$: Comparison with other single-layer cuprates. *Phys. Rev. B* **77**, 094516 (2008). URL <http://link.aps.org/doi/10.1103/PhysRevB.77.094516>.
- ¹⁸ Pintschovius, L. Electron-phonon coupling effects explored by inelastic neutron scattering. *Physica Status Solidi B-Basic Research* **242**, 30–50 (2005). URL <http://dx.doi.org/10.1002/pssb.200404951>.
- ¹⁹ Phillips, J. C. Self-organized networks and lattice effects in high-temperature superconductors. *Phys. Rev. B* **75**, 214503 (2007). URL <http://link.aps.org/doi/10.1103/PhysRevB.75.214503>.
- ²⁰ Li, C. W. *et al.* Structural relationship between negative thermal expansion and quartic anharmonicity of cubic scf_3 . *Phys. Rev. Lett.* **107**, 195504 (2011). URL <http://link.aps.org/doi/10.1103/PhysRevLett.107.195504>.
- ²¹ Lan, T. *et al.* Anharmonic lattice dynamics of Ag_2O studied by inelastic neutron scattering and first-principles molecular dynamics simulations. *Phys. Rev. B* **89**, 054306 (2014). URL <http://link.aps.org/doi/10.1103/PhysRevB.89.054306>.
- ²² Hui, J. C. K. & Allen, P. B. Effect of lattice anharmonicity on superconductivity. *Journal of Physics F: Metal Physics* **4**, L42 (1974). URL <http://stacks.iop.org/0305-4608/4/i=3/a=003>.
- ²³ Crespi, V. H., Cohen, M. L. & Penn, D. R. Anharmonic phonons and the isotope effect in superconductivity. *Phys. Rev. B* **43**, 12921–12924 (1991). URL <http://link.aps.org/doi/10.1103/PhysRevB.43.12921>.
- ²⁴ Crespi, V. H. & Cohen, M. L. Anharmonic phonons and the anomalous isotope effect in $\text{La}_{2-x}\text{Sr}_x\text{CuO}_4$. *Phys. Rev. B* **44**, 4712–4715 (1991). URL <http://link.aps.org/doi/10.1103/PhysRevB.44.4712>.
- ²⁵ Crespi, V. H. & Cohen, M. L. Anharmonic phonons and high-temperature superconductivity. *Phys. Rev. B* **48**, 398–406 (1993). URL <http://link.aps.org/doi/10.1103/PhysRevB.48.398>.
- ²⁶ Keller, H. Unconventional isotope effects in cuprate superconductors. In Müller, K. A. & Bussmann-Holder, A. (eds.) *In Superconductivity in Complex Systems. Springer Series Structure and Bonding*, vol. 114, 143–169 (Springer Berlin Heidelberg, Berlin, Heidelberg, 2005). URL <http://dx.doi.org/10.1007/b101019>.
- ²⁷ Keller, H., Bussmann-Holder, A. & Müller, K. A. Jahnteller physics and high- T_c superconduc-

- tivity. *Materials Today* **11**, 38 – 46 (2008). URL <http://www.sciencedirect.com/science/article/pii/S1369702108701780>.
- ²⁸ de Gennes, P. G. *Superconductivity of Metals and Alloys* (Addison-Wesley Publishing Co., Inc., Redwood City, California, 1989).
- ²⁹ Schrieffer, J. R. *Theory of Superconductivity* (Perseus Books, Reading, Massachusetts, 1999).
- ³⁰ Bogoliubov, N. N., Tolmachev, V. V. & Shirkov, D. V. *A New Method in the Theory of Superconductivity* (Consultants Bureau, Inc., New York, 1959).
- ³¹ Morel, P. & Anderson, P. W. Calculation of the superconducting state parameters with retarded electron-phonon interaction. *Phys. Rev.* **125**, 1263–1271 (1962). URL <http://link.aps.org/doi/10.1103/PhysRev.125.1263>.
- ³² Cohen, M. L. Superconductivity in low-carrier density systems: Degenerate semiconductors. In Parks, R. D. (ed.) *Superconductivity*, vol. 1, 615–664 (Marcel Dekker, Inc., New York, 1969).
- ³³ Tsuei, C. C. & Kirtley, J. R. Pairing symmetry in cuprate superconductors. *Rev. Mod. Phys.* **72**, 969–1016 (2000). URL <http://link.aps.org/doi/10.1103/RevModPhys.72.969>.
- ³⁴ Schrieffer, J. R., Scalapino, D. J. & Wilkins, J. W. Effective tunneling density of states in superconductors. *Phys. Rev. Lett.* **10**, 336–339 (1963). URL <http://link.aps.org/doi/10.1103/PhysRevLett.10.336>.
- ³⁵ Scalapino, D. J., Schrieffer, J. R. & Wilkins, J. W. Strong-coupling superconductivity. i. *Phys. Rev.* **148**, 263–279 (1966). URL <http://link.aps.org/doi/10.1103/PhysRev.148.263>.
- ³⁶ Karppinen, M. *et al.* Layer-specific hole concentrations in $\text{bi}_2\text{sr}_2\text{y}_{1-x}\text{ca}_x\text{cu}_2\text{o}_{8+\delta}$ as probed by xanes spectroscopy and coulometric redox analysis. *Phys. Rev. B* **67**, 134522 (2003). URL <http://link.aps.org/doi/10.1103/PhysRevB.67.134522>.
- ³⁷ Liang, R., Bonn, D. A. & Hardy, W. N. Evaluation of cuo_2 plane hole doping in $\text{yba}_2\text{cu}_3\text{o}_{6+x}$ single crystals. *Phys. Rev. B* **73**, 180505 (2006). URL <http://link.aps.org/doi/10.1103/PhysRevB.73.180505>.
- ³⁸ Naqib, S. H., Cooper, J. R., Tallon, J. L. & Panagopoulos, C. Temperature dependence of electrical resistivity of high-t-c cuprates - from pseudogap to overdoped regions. *Physica C-Superconductivity and Its Applications* **387**, 365–372 (2003). URL [http://dx.doi.org/10.1016/S0921-4534\(02\)02330-4](http://dx.doi.org/10.1016/S0921-4534(02)02330-4).
- ³⁹ Yoshida, T. *et al.* Low-energy electronic structure of the high-tc cuprates $\text{la}_{2-x}\text{sr}_x\text{cuo}_4$ studied by angle-resolved photoemission spectroscopy. *Journal of Physics: Condensed Matter* **19**, 125209

- (2007). URL <http://stacks.iop.org/0953-8984/19/i=12/a=125209>.
- ⁴⁰ Ono, S. & Ando, Y. Evolution of the resistivity anisotropy in $\text{Bi}_2\text{Sr}_{2-x}\text{La}_x\text{CuO}_{6+\delta}$ single crystals for a wide range of hole doping. *Phys. Rev. B* **67**, 104512 (2003). URL <http://link.aps.org/doi/10.1103/PhysRevB.67.104512>.
- ⁴¹ Bangura, A. F. *et al.* Fermi surface and electronic homogeneity of the overdoped cuprate superconductor $\text{tl}_2\text{ba}_2\text{cuo}_{6+\delta}$ as revealed by quantum oscillations. *Phys. Rev. B* **82**, 140501 (2010). URL <http://link.aps.org/doi/10.1103/PhysRevB.82.140501>.
- ⁴² Rourke, P. M. C. *et al.* A detailed de Haas-van Alphen effect study of the overdoped cuprate $\text{tl}_2\text{ba}_2\text{cuo}_{6+\delta}$. *New Journal of Physics* **12**, 105009 (2010). URL <http://stacks.iop.org/1367-2630/12/i=10/a=105009>.
- ⁴³ Kurtin, S., McGill, T. C. & Mead, C. A. Fundamental transition in the electronic nature of solids. *Phys. Rev. Lett.* **22**, 1433–1436 (1969). URL <http://link.aps.org/doi/10.1103/PhysRevLett.22.1433>.
- ⁴⁴ Takagi, H. *et al.* Superconductor-to-nonsuperconductor transition in $(\text{la}_{1-x}\text{sr}_x)_2\text{cuo}_4$ as investigated by transport and magnetic measurements. *Phys. Rev. B* **40**, 2254–2261 (1989). URL <http://link.aps.org/doi/10.1103/PhysRevB.40.2254>.
- ⁴⁵ Herzberg, G. *Molecular Spectra and Molecular Structure I. Spectra of Diatomic Molecules* (D. Van Nostrand Company, Inc. Princeton, New Jersey, 1950).
- ⁴⁶ Herzberg, G. *Molecular Spectra and Molecular Structure II. Infrared and Raman Spectra of Polyatomic Molecules* (D. Van Nostrand Company, Inc. Princeton, New Jersey, 1945).
- ⁴⁷ Wilson, E. B., Decius, J. C. & Cross, P. C. *Molecular Vibrations. The Theory of Infrared and Raman Vibrational Spectra* (Dover Publications, Inc., New York, 1980).
- ⁴⁸ Pereiro, J. *et al.* Insights from the study of high-temperature interface superconductivity. *Philosophical Transactions of the Royal Society of London A: Mathematical, Physical and Engineering Sciences* **370**, 4890–4903 (2012). URL <http://rsta.royalsocietypublishing.org/content/370/1977/4890>.
- ⁴⁹ Allen, P. B. & Dynes, R. C. Transition temperature of strong-coupled superconductors reanalyzed. *Phys. Rev. B* **12**, 905–922 (1975). URL <http://link.aps.org/doi/10.1103/PhysRevB.12.905>.
- ⁵⁰ Blatt, J. M. *Theory of Superconductivity* (Academic Press Inc., New York and London, 1964).
- ⁵¹ Ginder, J. M. *et al.* Photoexcitations in la_2cuo_4 : 2-eV energy gap and long-lived defect states.

- Phys. Rev. B* **37**, 7506–7509 (1988). URL <http://link.aps.org/doi/10.1103/PhysRevB.37.7506>.
- ⁵² Zhang, F. C. & Rice, T. M. Effective hamiltonian for the superconducting cu oxides. *Phys. Rev. B* **37**, 3759–3761 (1988). URL <http://link.aps.org/doi/10.1103/PhysRevB.37.3759>.
- ⁵³ Becke, A. D. Density-functional thermochemistry. iii. the role of exact exchange. *J. Chem. Phys.* **98**, 5648–5652 (1993). URL <http://scitation.aip.org/content/aip/journal/jcp/98/7/10.1063/1.464913>.
- ⁵⁴ Crowley, J. M., Tahir-Kheli, J. & Goddard, W. A. Resolution of the band gap prediction problem for materials design. *J. Phys. Chem. Lett.* **7**, 1198–1203 (2016). URL <http://dx.doi.org/10.1021/acs.jpcllett.5b02870>.
- ⁵⁵ Saunders, V. *et al.* *CRYSTAL98 User's Manual* (University of Torino: Torino, 1998).
- ⁵⁶ Lee, C., Yang, W. & Parr, R. G. Development of the colle-salvetti correlation-energy formula into a functional of the electron density. *Phys. Rev. B* **37**, 785–789 (1988). URL <http://link.aps.org/doi/10.1103/PhysRevB.37.785>.
- ⁵⁷ CRYSTAL98 only had basic Fock Matrix mixing convergence (SCF) at the time of our calculation in 2001.⁹ Using the most recent version of CRYSTAL (2015), we find the gap to be 3.1 eV using exactly the same basis set. Improved SCF convergence algorithms, increased computing power, and memory indicates our result of 2001 had not fully converged. We know hybrid functionals generally overestimate the band gaps of Mott antiferromagnets by ≈ 1 eV,⁵⁴ perhaps because the unrestricted spin wavefunctions (UHF) do not represent the correct spin state. Regardless, the orbital character of the doped hole is unchanged. None of the conclusions of the current paper are altered.
- ⁵⁸ Hybertsen, M. S., Stechel, E. B., Foulkes, W. M. C. & Schluter, M. Model for low-energy electronic states probed by x-ray absorption in high-*t_c* cuprates. *Physical Review B* **45**, 10032–10050 (1992). URL <http://link.aps.org/doi/10.1103/PhysRevB.45.10032>.
- ⁵⁹ Scalapino, D. J. The electron-phonon interaction and strong-coupling superconductors. In Parks, R. D. (ed.) *Superconductivity*, vol. 1, 449–560 (Marcel Dekker, Inc., New York, 1969).
- ⁶⁰ Vidberg, H. J. & Serene, J. W. Solving the eliashberg equations by means of n-point padé approximants. *Journal of Low Temperature Physics* **29**, 179–192 (1977). URL <http://dx.doi.org/10.1007/BF00655090>.
- ⁶¹ Leavens, C. & Ritchie, D. Extension of the n-point padé approximants solution of the eliashberg

- equations to $t \sim tc$. *Solid State Communications* **53**, 137 – 142 (1985). URL <http://www.sciencedirect.com/science/article/pii/0038109885901127>.
- ⁶² Beach, K. S. D., Gooding, R. J. & Marsiglio, F. Reliable padé analytical continuation method based on a high-accuracy symbolic computation algorithm. *Phys. Rev. B* **61**, 5147–5157 (2000). URL <http://link.aps.org/doi/10.1103/PhysRevB.61.5147>.
- ⁶³ Östlin, A., Chioncel, L. & Vitos, L. One-particle spectral function and analytic continuation for many-body implementation in the exact muffin-tin orbitals method. *Phys. Rev. B* **86**, 235107 (2012). URL <http://link.aps.org/doi/10.1103/PhysRevB.86.235107>.
- ⁶⁴ Elliott, R. J., Krumhansl, J. A. & Leath, P. L. The theory and properties of randomly disordered crystals and related physical systems. *Rev. Mod. Phys.* **46**, 465–543 (1974). URL <http://link.aps.org/doi/10.1103/RevModPhys.46.465>.
- ⁶⁵ Hussey, N. E. *et al.* Dichotomy in the t -linear resistivity in hole-doped cuprates. *Philosophical Transactions of the Royal Society a-Mathematical Physical and Engineering Sciences* **369**, 1626–1639 (2011). URL <http://rsta.royalsocietypublishing.org/content/369/1941/1626>.
- ⁶⁶ Abdel-Jawad, M. *et al.* Anisotropic scattering and anomalous normal-state transport in a high-temperature superconductor. *Nature Physics* **2**, 821–825 (2006). URL <http://dx.doi.org/10.1038/Nphys449>.
- ⁶⁷ Cooper, R. A. *et al.* Anomalous criticality in the electrical resistivity of $\text{La}_2\text{-xSr}_x\text{CuO}_4$. *Science* **323**, 603–607 (2009). URL <http://dx.doi.org/10.1126/science.1165015>.

Appendix A: Analysis of Physicist and Chemist DFT

Since our prior normal state and current T_c results depend on the assumption that the chemist’s out-of-the-CuO₂ hole is correct, we discuss the physicist’s and chemist’s DFT approaches here.

Immediately following the discovery of cuprates in 1986, density functional (DFT) band structure calculations were performed using the local density approximation (LDA).⁵⁻⁷ These calculations all found the ground state of the undoped cuprates to be metallic rather than an insulating spin-1/2 antiferromagnet (AF) with a nonzero band gap of ≈ 2 eV.⁵¹ The orbital character of the electrons near the Fermi level was a mixture of planar Cu $d_{x^2-y^2}$ and planar O p_σ , where the x and y-axes and the p_σ orbitals point along the planar Cu–O bonds. Hence, LDA found the correct orbital character at the Fermi level. The problem was the electrons were not localized.

The reason for this error of LDA and the more modern PBE (Perdew-Burke-Ernzerhof) density functional⁴ arises because both LDA and PBE contain unphysical Coulomb repulsion of an electron with itself⁸ (known as the self-Coulomb repulsion). The self-repulsion spreads the electron density out, leading to greater electron hopping, and hence an increase of the valence and conduction band widths. The increased band widths reduce the gap. In the case of cuprates, the gap is reduced to zero.

Given the failure of state-of-the-art ab initio methods for the undoped AF insulator, two different approaches were taken. In the first approach, the hole created by a dopant was assumed to “knock out” one of the localized magnetic electrons by forming a spin singlet state (no magnetism) with the localized planar Cu $d_{x^2-y^2}$ spin and the neighboring planar O atoms p_σ orbitals to form a Zhang-Rice singlet.⁵² This unmagnetized “hole” in the AF spin background could hop from planar Cu site to planar Cu site. The interaction of these holes with each other and with the AF background spins comprise the $t - J$ and $t + U$ classes of Hubbard models for cuprates.

The second approach argued that the metallic band structure found by ab initio computations was a reasonable starting point for understanding cuprates because, in the superconducting range of dopings, the high temperature phase is metallic. Hence, only the Fermi level needed to be lowered to match the doping.

Both attacks assumed the only relevant orbitals for understanding cuprates are planar

Cu $d_{x^2-y^2}$ and planar O p_σ . These two pictures dominate the 30 year literature on cuprates.

Chemically, neither of these two approaches makes sense. An out-of-plane hole dopant has a net negative charge relative to the undoped background. In analogy to acceptor (p-type) dopants in semiconductors, a *localized* level surrounding the dopant should be pulled out of the valence band (the acceptor level). For cuprates, the hole orbital should be *localized* and comprised of out-of-plane character pointing toward the dopant. Instead, ab-initio DFT and the above two approaches remove a *delocalized* electron with orbital character pointing away from the dopant (inside the CuO_2 plane). If the acceptor impurity level was shallow (energy close to the top of the valence band), then at moderate temperatures, the hole will be in the valence band. In this case, the physicist's hole state would be correct, except at the lowest temperatures. However, using the chemist's DFT methods described below, the impurity state is found to be ≈ 0.75 eV above the top of the valence band for a hole doping of 12.5% ($x = 0.125$) in $\text{La}_{2-x}\text{Sr}_x\text{CuO}_4$ (see Figure 4b of Perry et al.¹⁰). The acceptor level is a deep trap.

Obtaining the correct doped electronic structure for cuprates requires correcting the self-Coulomb repulsion error in the LDA and PBE functionals that led to an undoped metallic ground state. A correction appeared in 1993 (seven years after the discovery of cuprates) by Becke⁵³ with the invention of hybrid density functionals. Hybrid density functionals reduce the self-Coulomb repulsion by including 20% exact Hartree-Fock exchange. In molecular chemistry, hybrid density functionals are superior to LDA and PBE, and have been the workhorses for ab initio computations over the past two decades. For crystalline materials, we have recently shown⁵⁴ that hybrid DFT functionals practically resolve the band gap prediction problem across the whole periodic table with a mean absolute deviation of 0.28 eV, while PBE has an absolute error of 1.27 eV. The LDA functional is worse than PBE and no numbers were reported.⁵⁴ These results are plotted in Figure 23.

Unfortunately, the appearance of the superior hybrid DFT method had no influence on the cuprate field. One possible explanation is that the ab initio band structure codes familiar to most physicists construct the Hamiltonian in a plane-wave basis set and the Hartree-Fock exchange term in hybrid DFT is computationally impractical in this basis space. Hybrid DFT becomes computationally practical using localized Gaussian basis sets. Localized basis sets are superior to plane-wave basis set for molecular problems and have been used extensively by ab initio quantum chemists. The first software to successfully implement hybrid

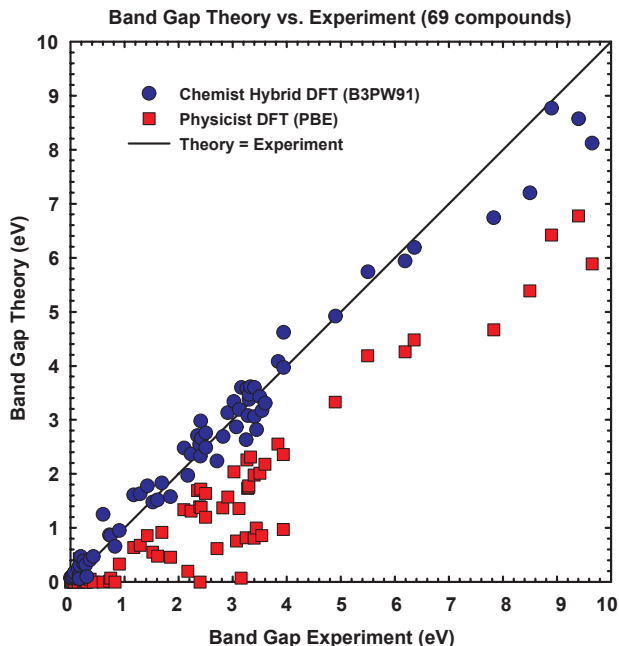


FIG. 23. Superiority of the chemist’s hybrid DFT functional, B3PW91,⁵³ (blue circles) to the physicist’s PBE density functional (red squares) for band gaps of 69 compounds across the whole periodic table. The vertical distance from the data points to the black diagonal line is the error between theory and experiment. The data is taken from Crowley et al.⁵⁴ These compounds include thermoelectrics, topological insulators, transition-metal oxides, photovoltaics, transition-metal halides, and elemental and binary semiconductors. The mean absolute error for B3PW91 is 0.28 eV and 1.27 eV for PBE. The mean error is -0.03 eV and -1.26 eV for B3PW91 and PBE, respectively. PBE consistently returns a low band gap. In 11 instances, PBE found zero gap (a metal) with the worst case being the Mott antiferromagnet FeO with an experimental gap of 2.4 eV. For the Mott antiferromagnet CoO, the experimental gap is 3.16 eV, while PBE is barely able to create a gap of 0.07 eV. Results for the LDA functional are much worse than PBE, and are not shown here.

DFT for solids was CRYSTAL98,⁵⁵ which used localized Gaussian basis functions. Regrettably, CRYSTAL98 appeared 12 years after the discovery of cuprate superconductivity.

Another possibility is historical. The solid state community has had enormous success for over 80 years assuming any inhomogeneity (such as impurities) is a small perturbation to a zeroth order Hamiltonian with full translational symmetry. Atomic-scale inhomogeneity of the kind suggested by the chemist’s DFT requires breaking translational symmetry at

zeroth order.

Using the hybrid DFT functional, B3LYP (Becke-3-Lee-Yang-Parr),^{53,56} we showed⁹ that a 2 eV band gap AF insulator is obtained⁵⁷ for undoped La_2CuO_4 , in agreement with experiment.⁵¹ Explicitly doped $\text{La}_{2-x}\text{Sr}_x\text{CuO}_4$ has hole states pointing out of the CuO_2 plane towards the dopants.¹⁰ Thus, in the case of cuprates, hybrid DFT has led to a completely different electronic structure than the LDA or PBE hole, as shown in Figure 1. The success of hybrid DFT in molecular chemistry and for the band gaps in Figure 23 strongly suggests hybrid DFT should be trusted over LDA and PBE DFT results. We believe this mistake with the doped electronic structure led the entire field astray.

*“If a mason building a wall puts the first stone in crooked,
no matter how tall the wall becomes, it will still be crooked.”*

Saadi Shirazi, (Born 1210, Died \approx 1291)

Appendix B: Degeneracy at the Fermi Level in an Isolated Plaquette that Splits in the Crystal Environment and Leads to the Pseudogap

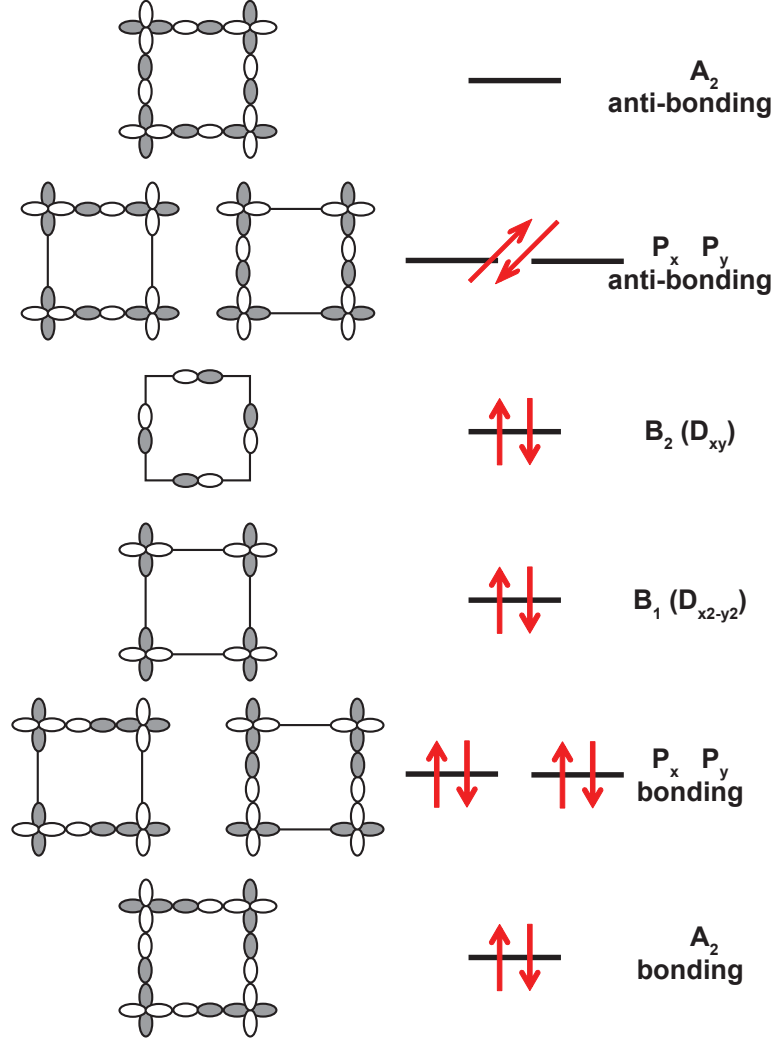
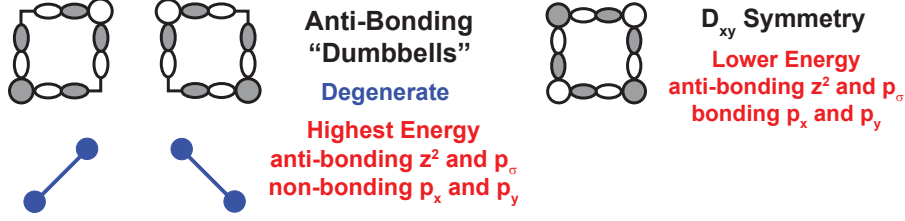


FIG. 24. The eight delocalized *planar* metallic states inside an isolated plaquette. These states are comprised of the planar Cu $d_{x^2-y^2}$ and planar O p_σ orbitals. The states are arranged with the highest energy state at the top and the lowest energy state at the bottom. The right column shows the electron occupation in red. There are two electrons per O p_σ and one electron per Cu $d_{x^2-y^2}$, leading to a total of twelve electrons. There are only two electrons to occupy the four degenerate P_x and P_y anti-bonding states. These states have dominant k-vector character at $(\pi, 0)$ and $(0, \pi)$. The splitting of the degenerate P_x and P_y states leads to the pseudogap.

Appendix C: Dumbbell Character of the Doped Plaquette Hole

The Three Highest Energy Out-of-Plane States



Hence, Out-of-Plane Hole Goes into Dumbbells

FIG. 25. The three highest energy out-of-the- CuO_2 plane states. The apical O atom p_z and the Cu $d_{3z^2-r^2}$ orbitals are shown as a circle at the vertices of the plaquette. The two degenerate “dumbbell” states are the highest in energy because they are non-bonding between the O p_x and p_y orbitals, while the D_{xy} state is bonding between these O orbitals. Since the hybridization of the p_x and p_y orbitals⁵⁸ is large (≈ 0.7 eV), it pulls the D_{xy} energy below the P-type dumbbell energy. Hence, the out-of-plane hole surrounding a negatively charged dopant is a dumbbell state.

Appendix D: Estimate of the Magnitude of the Electron-Phonon Coupling, g

It is known to be qualitatively correct that $\hbar\omega_D/E_F \approx \sqrt{m/M}$ where $\hbar\omega_D$ is the Debye energy, E_F is the Fermi energy, m is the electron mass, and M is the nuclear mass. One can quickly see that the form of the above expression is correct using $\omega_D \sim \sqrt{K/M}$ where K is the spring constant and $K \sim E_F k_F^2 \sim mE_F^2/\hbar^2$ due to metallic electron screening.

The electron-phonon coupling, g , is of the form $g \sim \sqrt{\hbar/2M\omega_D} \nabla V$, where V is the nuclear potential energy. Substituting $\nabla V \sim k_F E_F$, leads to $g^2 \sim (\hbar/2M\omega_D) k_F^2 E_F^2 \sim (m/M) E_F^3 / (\hbar\omega_D) \sim (\hbar\omega_D) E_F$. Hence, $g \approx \sqrt{\hbar\omega_D E_F}$.

Another derivation is dimensional. The coupling, g , has dimensions of energy and there are only two relevant energy scales, $\hbar\omega_D$ and E_F . Thus there are three possibilities for g : the mean, the geometric mean, and the harmonic mean of $\hbar\omega$ and E_F . Since $\hbar\omega_D \ll E_F$, the mean is $\approx E_F$, and the harmonic mean is $\approx \hbar\omega_D$. Neither of these two means makes intuitive sense because we know metallic electrons strongly screen the nuclear-nuclear potential. The only sensible choice is the geometric mean, $g \sim \sqrt{\hbar\omega_D E_F}$.

Appendix E: Fluctuation T_c : Plaquette Clusters Smaller than the Coherence Length

There are superconducting fluctuations above T_c at low dopings due to the fluctuating magenta plaquette clusters in Figures 8, 9, and 10. These plaquette clusters have superconducting pairing that does not contribute to the observed T_c because the clusters are smaller than the coherence length. Including these clusters into the T_c computation leads to an estimate of the temperature range where plaquette cluster superconducting fluctuations occur above T_c . The resulting “fluctuation T_c domes” are plotted in Figure 26. Of course, there exist superconducting fluctuations above T_c from the plaquettes clusters that are larger than the coherence length (yellow clusters in Figures 8, 9, and 10). The fluctuation T_c from the larger yellow clusters is not included in figure 26.

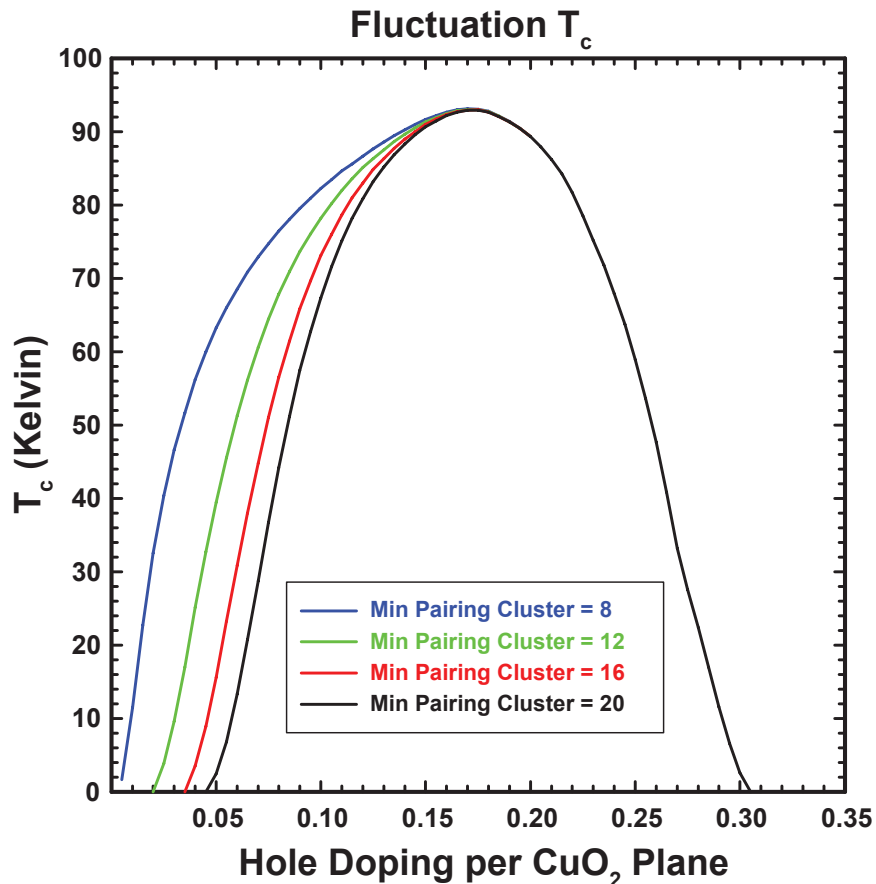


FIG. 26. The change in the T_c -dome as a function of the minimum plaquette cluster size for superconducting pairing. The black curve is identical to the black T_c curve in Figure 16. All parameters are described in Appendix F.

Appendix F: Parameters Used in the T_c Computations

TABLE II. The planar Cu $d_{x^2-y^2}$ and O p_σ band structure used in all T_c computations. We use effective single band parameters derived from the angle-resolved photoemission (ARPES) Fermi surface for single layer Bi2201.¹⁷ The 2D tight-binding band structure is $\epsilon_k = -2t[\cos(k_x a) + \cos(k_y a)] - 4t' \cos(k_x a) \cos(k_y a) - 2t''[\cos(2k_x a) + \cos(2k_y a)]$, where a is the planar Cu–Cu lattice size and the 2D momentum is $\mathbf{k} = (k_x, k_y)$. The ratio $t''/t' = -1/2$ is assumed.¹⁷ The variable n in the table is the number of metallic electrons per metallic Cu. At optimal doping, the number of holes per metallic Cu in the CuO_2 plane is $x = 0.16$, leading to $n = 1.0 - x = 0.84$. The optimal doping Fermi level is used for *all* dopings in order to keep the number of parameters to a minimum. For the multi-layer T_c calculations in Figure 17, we assume the 2D band structure ϵ_k above. The 2D \mathbf{k} states in adjacent layers, l and $l \pm 1$, are coupled by a momentum dependent matrix element equal to $\langle k, l \pm 1 | H_{inter} | k, l \rangle = -\alpha t_z (1/4) (\cos(k_x a) - \cos(k_y a))^2$, where α is the product of the fraction of metallic sites in layers l and $l \pm 1$. Since interlayer hopping of an electron between Cu sites on different layers can only occur if the two Cu sites are metallic, α is the probability of two adjacent Cu sites in different layers being metallic. The dopings of the individual layers in the multi-layer T_c calculations are all less than the threshold for plaquette overlap at $x = 0.187$. Hence, each plaquette covers 4 Cu sites. For example, between layers doped at $x = 0.16$ and $x = 0.11$, $\alpha = 4(0.16) \times 4(0.11) = 0.2816$ leading to $\alpha t_z \approx 0.023$ eV.

n	t (eV)	t' (eV)	t_z (eV)
0.84	0.25	-0.05625	0.08

TABLE III. Parameters that remain the same for every T_c calculation. They are the mass-enhancement parameter derived from the high-temperature linear slope of the resistivity, λ_{tr} , the Debye energy, $\hbar\omega_D$, the minimum energy used in the low-temperature linear resistivity, $\hbar\omega_{min}$, the energy cutoff for Eliashberg sums, $\hbar\omega_c$, and the energy of the O atom phonon modes, $\hbar\omega_{ph}$.

λ_{tr} (dimensionless)	$\hbar\omega_D$ (Kelvin)	$\hbar\omega_{min}$ (Kelvin)	$\hbar\omega_c$ (eV)	$\hbar\omega_{ph}$ (eV)
0.5	300	1.0	0.3	0.06

TABLE IV. Parameters for the T_c curves in Figures 16, 17, and 26. The variable, N_{min} , is the number of metallic Cu sites inside the smallest plaquette cluster that is larger than the coherence length, and thereby contributes to T_c . The edge, convex, and concave couplings are chosen to be equal for the next layer couplings. All units are eV.

Figure	Curve Color	N_{min}	$\delta\epsilon$			δt			Next Layer	
			Edge	Convex	Concave	Edge	Convex	Concave	$\delta\epsilon_{NL}$	δt_{NL}
16	Black	20	0.150	0.150	0.075	0.240	0.240	0.120		
16	Magenta	20	0.150	0.150	0.075	0.130	0.130	0.065		
16	Red	100	0.000	0.000	0.000	0.132	0.132	0.000		
26	Blue	8	0.150	0.150	0.075	0.240	0.240	0.120		
26	Green	12	0.150	0.150	0.075	0.240	0.240	0.120		
26	Red	16	0.150	0.150	0.075	0.240	0.240	0.120		
26	Black	20	0.150	0.150	0.075	0.240	0.240	0.120		
17	Black	20	0.150	0.150	0.075	0.240	0.240	0.120	0.0	0.2
17	Blue	20	0.050	0.000	0.000	0.130	0.130	0.065	0.05	0.13

TABLE V. Doping of each CuO_2 layer in the multi-layer T_c calculations. The outermost layers are always at optimal doping ($x = 0.16$). The adjacent layers are at $x = 0.11$ doping. The innermost layers are all at $x = 0.09$ doping. These dopings are obtained from Cu Knight shift measurements.²

Layers	Hole Doping per CuO_2 Layer									
1	0.16									
2	0.16	0.16								
3	0.16	0.11	0.16							
4	0.16	0.11	0.11	0.16						
5	0.16	0.11	0.09	0.11	0.16					
6	0.16	0.11	0.09	0.09	0.11	0.16				
7	0.16	0.11	0.09	0.09	0.09	0.11	0.16			
8	0.16	0.11	0.09	0.09	0.09	0.09	0.11	0.16		
9	0.16	0.11	0.09	0.09	0.09	0.09	0.09	0.11	0.16	
10	0.16	0.11	0.09	0.09	0.09	0.09	0.09	0.09	0.11	0.16

Appendix G: Description of the Eliashberg T_c Calculations

1. The Eliashberg Equations

The attractive electron-electron pairing mediated by phonons is not instantaneous in time due to the non-zero frequency of the phonon modes (phonon retardation). In addition, electrons are scattered by phonons leading to electron wavefunction renormalization (“lifetime effects”) that decrease T_c . Any credible T_c prediction must incorporate *both* of these effects. All T_c calculations in this paper solve the Eliashberg equations for the superconducting pairing wavefunction (also called the gap function). It includes both the pairing retardation and the electron lifetime.^{16,29,59}

The Eliashberg equations are non-linear equations for the superconducting gap function, $\Delta(\mathbf{k}, \omega, T)$, and the wave function renormalization, $Z(\mathbf{k}, \omega, T)$, as a function of momentum \mathbf{k} , frequency ω , and temperature T . Usually, the T dependence of Δ and Z is assumed, and they are written as $\Delta(\mathbf{k}, \omega)$ and $Z(\mathbf{k}, \omega)$, respectively. We follow this convention here. Both $\Delta(\mathbf{k}, \omega)$ and $Z(\mathbf{k}, \omega)$ are a complex numbers. In this Appendix only, we will absorb Boltzmann’s constant, k_B , into T . Thus T has units of energy.

Both Δ and Z are frequency dependent because of the non-instantaneous nature of the superconducting electron-electron pairing. If the pairing via phonons was instantaneous in time, then there would be no frequency dependence to Δ and Z . The simpler BCS²⁹ gap equation assumes an instantaneous pairing interaction (Δ is independent of ω) and no wavefunction renormalization ($Z = 1$).

The Eliashberg equations may be solved in momentum and frequency space (\mathbf{k}, ω) , or in momentum and discrete imaginary frequency space, $(\mathbf{k}, i\omega_n)$, where n is an integer and $\omega_n = (2n + 1)\pi T$. In the imaginary frequency space representation, the temperature dependence and the retardation of the phonon induced pairing are both absorbed into the imaginary frequency dependence, $i\omega_n$. In theory, both $\Delta(\mathbf{k}, \omega)$ and $Z(\mathbf{k}, \omega)$ can be obtained by analytic continuation of their $(\mathbf{k}, i\omega_n)$ counterparts. In practice, the analytic continuation is fraught with numerical difficulties.^{60–63} However, the symmetry of the gap can be extracted from either the real or imaginary frequency representations of Δ .

In the pioneering work of Schrieffer, Scalapino, and Wilkins,^{29,34,35,59} the goal was to obtain the isotropic (in k -space) gap function at zero temperature, $\Delta(\omega)$, as a function of ω

in order to compute the superconducting tunneling of lead ($T_c = 7.2$ K). Hence, they solved the full non-linear Eliashberg equations in frequency space.

Above T_c , $\Delta(\mathbf{k}, \omega)$ is zero. For $T \approx T_c$, Δ is small. Since our interest in this paper is on the magnitude of T_c and the symmetry of the superconducting gap, we can linearize the gap, Δ , in the Eliashberg equations for temperatures, T , close to T_c . The result is a temperature dependent real symmetric matrix eigenvalue equation with $\Delta(\mathbf{k}, \omega)$ as the eigenvector. The eigenvalues are dimensionless and the largest eigenvalue monotonically increases as T decreases. For $T > T_c$, the largest eigenvalue of the real symmetric matrix is less than 1. At $T = T_c$, the largest eigenvalue equals 1, signifying the onset of superconductivity.

The non-linear Eliashberg equations (or the linearized version) are easier to solve in imaginary frequency space.¹⁶ Hence, we solve the linearized Eliashberg equations in imaginary frequency space to obtain T_c .

We use the linearized Eliashberg equations as derived in the excellent chapter by Allen and Mitrovic.¹⁶ Prior Eliashberg formulations assume translational symmetry (momentum \mathbf{k} is a good quantum number for the metallic states). Our metallic wavefunctions are not \mathbf{k} states because they are only non-zero in the percolating metallic region. We write the wavefunction and energy for the state with index l as ψ_l and ϵ_l , respectively. Since ψ_l is only delocalized over the metallic region and is normalized, $\psi_l \sim 1/\sqrt{N_M}$, where N_M is the total number of metallic Cu sites. Rather than Cooper pairing occurring between $\mathbf{k} \uparrow$ and its time-reversed partner, $-\mathbf{k} \downarrow$, a Cooper pair here is comprised of $(\psi_l \uparrow, \bar{\psi}_l \downarrow)$, where $\bar{\psi}_l$ is the complex conjugate of ψ_l .

The linearized Eliashberg equations for $\Delta(l, i\omega_n)$ and $Z(l, i\omega_n)$ are obtained from the \mathbf{k} -vector equations¹⁶ simply by replacing \mathbf{k} with the index l everywhere

$$Z(l, i\omega_n) = 1 + \frac{\pi T}{|\omega_n|} \sum_{l'n'}^{|\omega_{n'}| < \omega_c} \left[\frac{\delta(\epsilon_{l'} - \epsilon_F)}{N(0)} \right] \lambda(l, l', \omega_n - \omega_{n'}) s_n s_{n'}, \quad (\text{G1})$$

$$\begin{aligned} Z(l, i\omega_n) \Delta(l, i\omega_n) &= \pi T \\ &\times \sum_{l'n'}^{|\omega_{n'}| < \omega_c} \frac{1}{|\omega_{n'}|} \left[\frac{\delta(\epsilon_{l'} - \epsilon_F)}{N(0)} \right] [\lambda(l, l', \omega_n - \omega_{n'}) - \mu^*(\omega_c)] \Delta(l', i\omega_{n'}), \end{aligned} \quad (\text{G2})$$

where ϵ_F is the Fermi energy, $N(0)$ is the total metallic density of states per spin per energy, $s_n = \omega_n/|\omega_n| = \text{sgn}(\omega_n)$ is the sign of ω_n , ω_c is the cutoff energy for the frequency sums, $\lambda(l, l', \omega_n)$ is the dimensionless phonon pairing strength (defined below), and $\mu^*(\omega_c)$

is the dimensionless Morel-Anderson Coulomb pseudopotential at cutoff energy ω_c . It is a real number. The wavefunction renormalization, $Z(l, i\omega_n)$, is dimensionless. In the non-linear Eliashberg equations, $\Delta(l, i\omega_n)$ has units of energy. In the linearized equations above, $\Delta(l, i\omega_n)$ is an eigenvector and is arbitrary up to a constant factor.

The ‘‘electron-phonon spectral function’’ $\alpha^2 F(l, l', \Omega)$ is defined

$$\alpha^2 F(l, l', \Omega) = N(0) \sum_{\sigma} | \langle l | H_{ep}^{\sigma} | l' \rangle |^2 \delta(\omega_{\sigma} - \Omega), \quad (\text{G3})$$

and the phonon pairing strength $\lambda(l, l', \omega_n)$ is defined

$$\lambda(l, l', \omega_n) = \int_0^{+\infty} d\Omega \alpha^2 F(l, l', \Omega) \left(\frac{2\Omega}{\omega_n^2 + \Omega^2} \right) \quad (\text{G4})$$

$$= N(0) \sum_{\sigma} | \langle l | H_{ep}^{\sigma} | l' \rangle |^2 \left(\frac{2\omega_{\sigma}}{\omega_n^2 + \omega_{\sigma}^2} \right), \quad (\text{G5})$$

where $\langle l | H_{ep}^{\sigma} | l' \rangle$ is the matrix element (units of energy) between initial and final states l' and l , respectively of the electron-phonon coupling, and H_{ep}^{σ} is the electron-phonon coupling for the phonon mode σ with energy ω_{σ} . Both $\alpha^2 F(l, l', \Omega)$ and $\lambda(l, l', \omega_n)$ are real positive numbers. Hence, $Z(l, i\omega_n)$ is a real positive number. From G2, the gap $\Delta(l, i\omega_n)$ can always be chosen to be real. Since $\lambda(l, l', \omega_n) = \lambda(l, l', -\omega_n)$ from equation G4,

$$Z(l, -i\omega_n) = Z(l, i\omega_n) = \text{Real Number}, \quad (\text{G6})$$

$$\Delta(l, -i\omega_n) = \Delta(l, i\omega_n) = \text{Real Number}. \quad (\text{G7})$$

$\alpha^2 F(l, l', \Omega)$ and $\lambda(l, l', \omega_n)$ are dimensionless because $(\text{eV})^{-1}(\text{eV})^2(\text{eV})^{-1} \sim 1$. Physically, they should be independent of the number of metallic Cu sites, N_M , as N_M becomes infinite. The independence with respect to N_M is shown below.

The electron-phonon Hamiltonian for phonon mode σ , H_{ep}^{σ} , is

$$H_{ep}^{\sigma} = \left(\frac{\hbar}{2M\omega_{\sigma}} \right)^{\frac{1}{2}} \nabla V(a_{\sigma} + a_{\sigma}^{\dagger}), \quad (\text{G8})$$

where M is the nuclear mass. a_{σ} and a_{σ}^{\dagger} destroy and create σ phonon modes, respectively. V is the potential energy of the electron. For localized phonon modes, ∇V is independent of the number of metallic sites, N_M . The l and l' metallic states each scale as $1/\sqrt{N_M}$,

leading to $\langle l|H_{ep}^\sigma|l' \rangle \sim 1/N_M$. Since the number of localized phonon modes scales as N_M , the N_M scaling of the sum $\sum_\sigma |\langle l|H_{ep}^\sigma|l' \rangle|^2$ is $\sim N_M(1/N_M)^2 \sim 1/N_M$. Hence, we have shown that $\alpha^2 F(l, l', \Omega)$ and $\lambda(l, l', \omega_n)$ are dimensionless and independent of N_M because the density of states per spin, $N(0)$, is proportional to N_M . In fact, $\alpha^2 F$ and λ are independent of N_M even when the phonon modes σ are delocalized. In this case, $\nabla V \sim 1/\sqrt{N_M}$. The electron-phonon matrix element $\langle l|H_{ep}^\sigma|l' \rangle$ is now summed over the crystal, and thereby picks up a factor of N_M . Hence, $\langle l|H_{ep}^\sigma|l' \rangle \sim N_M \times \sqrt{1/N_M} \times \sqrt{1/N_M} \times \sqrt{1/N_M} \sim 1/\sqrt{N_M}$. For delocalized phonons, the sum over phonon modes σ in $\sum_\sigma |\langle l|H_{ep}^\sigma|l' \rangle|^2$ does not add another factor of N_M . The claim is obvious when l and l' are momentum states \mathbf{k} and \mathbf{k}' because the only phonon mode that connects these two states has momentum $\mathbf{q} = \mathbf{k} - \mathbf{k}'$. Therefore, $\alpha^2 F(l, l', \Omega)$ and $\lambda(l, l', \omega_n)$ are always dimensionless and independent of N_M .

The atomic-scale inhomogeneity of cuprates implies translation is not a perfect symmetry of the crystal. However, the dopants are distributed *randomly*, and therefore *on average* \mathbf{k} becomes a good quantum number. Hence, we may work with Green's functions in \mathbf{k} space and approximate the Cooper pairing to occur between $(\mathbf{k} \uparrow, -\mathbf{k} \downarrow)$ states. The approximation is identical to the very successful Virtual Crystal Approximation (VCA) and the Coherent Potential Approximation (CPA) for random alloys.⁶⁴

In the VCA and CPA, the Green's function between two distinct \mathbf{k} states, \mathbf{k} and \mathbf{k}' is zero

$$G(\mathbf{k}, \mathbf{k}', i\omega_n) \approx 0, \text{ if } \mathbf{k} \neq \mathbf{k}'. \quad (\text{G9})$$

The fact that \mathbf{k} is *not* a good quantum number of the crystal is incorporated by including a self-energy correction, $\Sigma(\mathbf{k}, i\omega_n)$ at zeroth order into the metallic Green's function

$$G(\mathbf{k}, i\omega_n) = \frac{1}{i\omega_n - \epsilon_{bare}(\mathbf{k}) - \Sigma(\mathbf{k}, i\omega_n)}. \quad (\text{G10})$$

Here, $\epsilon_{bare}(\mathbf{k})$ is the bare electron energy. $\Sigma(\mathbf{k}, i\omega_n)$ can be written as the sum of two terms, $\Sigma(\mathbf{k}, i\omega_n) = \Sigma_0(\mathbf{k}, i\omega_n) + i\omega_n \Sigma_1(\mathbf{k}, i\omega_n)$. Both Σ_0 and Σ_1 are even powers of ω_n , $\Sigma_i(\mathbf{k}, -i\omega_n) = \Sigma_i(\mathbf{k}, i\omega_n)$, for $i = 1, 2$. Σ_0 adds a shift to the bare electron energy, $\epsilon_{bare}(\mathbf{k})$, and a lifetime broadening to the electronic state. Σ_1 leads to wavefunction renormalization of the bare electron state.

The shift of $\epsilon_{bare}(\mathbf{k})$ due to $\Sigma_0(\mathbf{k}, i\omega_n)$ leads to the observed angle-resolved photoemission

(ARPES) band structure in cuprates,¹⁷ $\epsilon_{\mathbf{k}}$, and its lifetime broadening. The lifetime broadening integrates out of the Eliashberg equations because the integral of a Lorentzian across the Fermi energy is independent of the width of the Lorentzian.¹⁶ Hence, we may use the ARPES band structure, $\epsilon_{\mathbf{k}}$, in the Eliashberg equations and absorb $\Sigma_1(\mathbf{k}, i\omega_n)$ into $Z(\mathbf{k}, i\omega_n)$ in the Eliashberg equations.

Hence, we are right back to the standard Eliashberg equations^{16,29,34,35,59}

$$\begin{aligned}
Z(\mathbf{k}, i\omega_n) &= 1 + \frac{\pi T}{|\omega_n|} \sum_{\mathbf{k}'n'}^{|\omega_{n'}| < \omega_c} \left[\frac{\delta(\epsilon_{\mathbf{k}'} - \epsilon_F)}{N(0)} \right] \lambda(\mathbf{k}, \mathbf{k}', \omega_n - \omega_{n'}) s_n s_{n'}, \\
Z(\mathbf{k}, i\omega_n) \Delta(\mathbf{k}, i\omega_n) &= \pi T \\
&\times \sum_{\mathbf{k}'n'}^{|\omega_{n'}| < \omega_c} \frac{1}{|\omega_{n'}|} \left[\frac{\delta(\epsilon_{\mathbf{k}'} - \epsilon_F)}{N(0)} \right] [\lambda(\mathbf{k}, \mathbf{k}', \omega_n - \omega_{n'}) - \mu^*(\omega_c)] \Delta(\mathbf{k}', i\omega_{n'}),
\end{aligned} \tag{G11}$$

$$Z(\mathbf{k}, -i\omega_n) = Z(\mathbf{k}, i\omega_n) = \text{Real Number}, \tag{G12}$$

$$\Delta(\mathbf{k}, -i\omega_n) = \Delta(\mathbf{k}, i\omega_n) = \text{Real Number}. \tag{G13}$$

The Eliashberg equations above are completely general for a single band crossing the Fermi level. The only inputs into the equations are the Fermi surface, Fermi velocity (in order to obtain the local density of states), the dimensionless electron-phonon pairing, $\lambda(\mathbf{k}, \mathbf{k}', \omega_n)$, and the dimensionless Morel-Anderson Coulomb pseudopotential at the cutoff energy (typically, chosen to be five times larger than the highest phonon mode, $\omega_c = 5\omega_{ph}$), $\mu^*(\omega_c)$. We apply the standard methods¹⁶ to map the above equations into a matrix equation for the highest eigenvalue as a function of T . The highest eigenvalue monotonically increases as T decreases. When the highest eigenvalue crosses 1, T_c is found.

Equations G11, G12, G13 need to be modified when more than one band crosses the Fermi level. Phonons can scatter electron pairs from one band to another in addition to scattering within a single band. The modification to the single Fermi surface Eliashberg equations above require changing the \mathbf{k} and \mathbf{k}' labels to $\mathbf{b}\mathbf{k}$ and $\mathbf{b}'\mathbf{k}'$ where \mathbf{b} and \mathbf{b}' refer to the band index. \mathbf{k} and \mathbf{k}' remain vectors in 2D so long as we assume the coupling of CuO_2 layers in different unit cells is weak. The number of bands is equal to the number of CuO_2 layers per unit cell, L . We derive the electron-phonon pairing λ for a single layer cuprate in sections G 2 and G 3. In section G 4, we derive the multi-layer λ .

The total electron-phonon spectral function is the sum of four terms

$$\alpha^2 F = \alpha^2 F_1 + \alpha^2 F_2 + \alpha^2 F_{surf} + \alpha^2 F_{\perp}, \quad (\text{G14})$$

where $\alpha^2 F_1$ and $\alpha^2 F_2$ are the spectral functions from phonons that contribute to the resistivity. $\alpha^2 F_1$ is due to the phonons that lead to the low-temperature linear term in the resistivity, and $\alpha^2 F_2$ is due to the phonons that lead to the the low-temperature T^2 resistivity term.⁶⁵ $\alpha^2 F_{surf}$ is the component due to the planar O atom at the surface between the metal and insulating regions. It is the O atom phonon shown in Figure 12a. $\alpha^2 F_{\perp}$ is the contribution from the planar O atom adjacent to the metal-insulator surface on the insulating AF side. It is shown in Figure 12b. Since the energy of these two O phonons modes is ≈ 60 meV,¹⁸ their contribution to the resistivity is very small.

Sections G 2 and G 3 in this Appendix derive the four $\alpha^2 F$ terms above in order to obtain the total phonon pairing, $\lambda = \lambda_1 + \lambda_2 + \lambda_{surf} + \lambda_{\perp}$, that is used in the Eliashberg equations G11, G12, and G13 for T_c .

2. Contribution to λ from the Interface O Atom Phonons in Figure 12

a. Surface O Atom Mode in Figure 12a

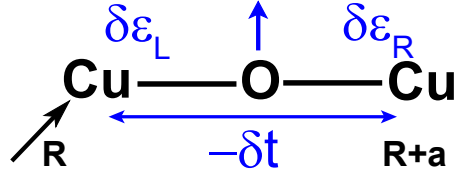


FIG. 27. A surface O atom phonon mode. The change in Cu orbital energy for the Cu atom, $\delta\epsilon_L$ for the left Cu atom, and $\delta\epsilon_R$, for the right Cu atom due to the displacement of the surface O atom on the metal-insulator interface. $-\delta t$ is the change in the hopping energy. The position of the left Cu atom is at \mathbf{R} and the right Cu atom is at $\mathbf{R}+\mathbf{a}$. $\delta\epsilon_L$, $\delta\epsilon_R$, and δt are functions of \mathbf{R} as seen in Figure 12a. We choose the energy of all the surface phonon modes to be the same and equal to ω_{ph} .

The Hamiltonian for Figure 27 is

$$H_{surf}(\mathbf{R}) = \delta\epsilon_L c_L^\dagger c_L + \delta\epsilon_R c_R^\dagger c_R - \delta t \left(c_L^\dagger c_R + c_R^\dagger c_L \right), \quad (\text{G15})$$

where c_L^\dagger and c_L create and destroy an electron at the L Cu site. c_R^\dagger and c_R are defined similarly. Since there is no electron spin coupling to the O atom phonon mode, the electron spin index is dropped in equation G15.

The \mathbf{k} state $\phi(\mathbf{k})$ is defined as

$$\phi(\mathbf{k}) = N_M^{-\frac{1}{2}} \sum_{\mathbf{R}} e^{i\mathbf{k}\cdot\mathbf{R}} \phi(\mathbf{R}), \quad (\text{G16})$$

where $\phi(\mathbf{R})$ is the localized effective Cu $d_{x^2-y^2}$ orbital at position \mathbf{R} , and N_M is the number of metallic Cu sites. The matrix element between \mathbf{k}' and \mathbf{k} is

$$\langle \phi(\mathbf{k}') | H_{surf}(\mathbf{R}) | \phi(\mathbf{k}) \rangle = N_M^{-1} e^{-i(k'-k)(R+\frac{1}{2}a)} \left[\delta\epsilon_L e^{\frac{i}{2}(k'-k)a} + \delta\epsilon_R e^{-\frac{i}{2}(k'-k)a} - 2\delta t \cos \frac{1}{2}(k'+k)a \right] \quad (\text{G17})$$

The modulus squared is

$$|\langle \phi(\mathbf{k}') | H_{surf}(\mathbf{R}) | \phi(\mathbf{k}) \rangle|^2 = N_M^{-2} \left\{ \left[(\delta\epsilon_L + \delta\epsilon_R) \cos \frac{1}{2}(k'-k)a - 2\delta t \cos \frac{1}{2}(k'+k)a \right]^2 + (\delta\epsilon_L - \delta\epsilon_R)^2 \sin^2 \frac{1}{2}(k'-k)a \right\} \quad (\text{G18})$$

Define the two functions of \mathbf{k} and \mathbf{k}' , $J_{surf}^{(x)}(\mathbf{k}, \mathbf{k}')$ and $J_{surf}^{(y)}(\mathbf{k}, \mathbf{k}')$ as

$$\begin{aligned} J_{surf}^{(x)}(\mathbf{k}, \mathbf{k}') &= \langle (\delta\epsilon_L + \delta\epsilon_R)^2 \rangle_x \cos^2 \frac{1}{2}(k'_x - k_x)a \\ &\quad - 2 \langle \delta t (\delta\epsilon_L + \delta\epsilon_R) \rangle_x \cos \frac{1}{2}(k'_x - k_x)a \cos \frac{1}{2}(k'_x + k_x)a \\ &\quad + \langle \delta t^2 \rangle_x \cdot 4 \cos^2 \frac{1}{2}(k'_x + k_x)a + \langle (\delta\epsilon_L - \delta\epsilon_R)^2 \rangle_x \sin^2 \frac{1}{2}(k'_x - k_x)a, \quad (\text{G19}) \end{aligned}$$

$$\begin{aligned} J_{surf}^{(y)}(\mathbf{k}, \mathbf{k}') &= \langle (\delta\epsilon_L + \delta\epsilon_R)^2 \rangle_y \cos^2 \frac{1}{2}(k'_y - k_y)a \\ &\quad - 2 \langle \delta t (\delta\epsilon_L + \delta\epsilon_R) \rangle_y \cos \frac{1}{2}(k'_y - k_y)a \cos \frac{1}{2}(k'_y + k_y)a \\ &\quad + \langle \delta t^2 \rangle_y \cdot 4 \cos^2 \frac{1}{2}(k'_y + k_y)a + \langle (\delta\epsilon_L - \delta\epsilon_R)^2 \rangle_y \sin^2 \frac{1}{2}(k'_y - k_y)a, \quad (\text{G20}) \end{aligned}$$

where $\langle F(\mathbf{R}_\sigma) \rangle_x$ is the average of the function $F(\mathbf{R}_\sigma)$ defined for each planar surface O on the x-axis with position \mathbf{R}_σ as shown in Figure 27,

$$\langle F(\mathbf{R}_\sigma) \rangle = \frac{1}{N_M} \sum_{\mathbf{R}_\sigma} F(\mathbf{R}_\sigma). \quad (\text{G21})$$

Similarly, $\langle F(\mathbf{R}_\sigma) \rangle_y$ is the average of $F(\mathbf{R}_\sigma)$ over the y-axis surface O atoms. The expression in equation G20 for $J_{surf}^{(y)}$ is identical to the expression for $J_{surf}^{(x)}$ in equation G19 with x replaced by y .

From the \mathbf{k} -space versions of equations G3 and G4

$$\lambda_{surf}(\mathbf{k}, \mathbf{k}', \omega_n) = \left(\frac{N(0)}{N_M} \right) \left[J_{surf}^{(x)}(\mathbf{k}, \mathbf{k}') + J_{surf}^{(y)}(\mathbf{k}, \mathbf{k}') \right] \left(\frac{2\omega_{ph}}{\omega_n^2 + \omega_{ph}^2} \right). \quad (\text{G22})$$

b. O Atom Mode Perpendicular to Surface in Figure 12b

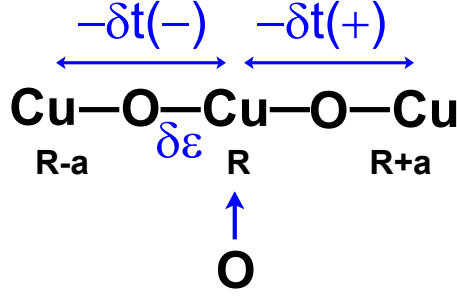


FIG. 28. The Perpendicular O atom phonon mode. The O atom is in the insulating AF region. The chain Cu–O–Cu–O–Cu is on the metal-insulator surface. The change in Cu orbital energy for the central Cu atom located at position \mathbf{R} is $\delta\epsilon$. $-\delta t(-)$ is the change in the hopping between the Cu site at $\mathbf{R} - \mathbf{a}$ and \mathbf{R} . $-\delta t(+)$ is the change in the hopping between the Cu site at $\mathbf{R} + \mathbf{a}$ and \mathbf{R} . $\delta\epsilon$, $\delta t(-)$, and $\delta t(+)$ are functions of position \mathbf{R} as seen in Figure 12b. We choose the energy of all the perpendicular surface phonon modes to be the same and equal to ω_{ph} . In this figure, the displaced O atom is on the y-axis while the Cu–O–Cu–O–Cu chain is along the x-axis. We choose the convention of labeling the phonon mode by the axis of the AF O atom. Hence, this figure is a y-axis O phonon mode.

The Hamiltonian for Figure 28 is

$$H_{\perp}(\mathbf{R}) = \delta\epsilon c_R^{\dagger} c_R - \delta t(-) \left(c_{R-a}^{\dagger} c_R + c_R^{\dagger} c_{R-a} \right) - \delta t(+) \left(c_{R+a}^{\dagger} c_R + c_R^{\dagger} c_{R+a} \right), \quad (\text{G23})$$

where c_R^\dagger and c_R create and destroy an electron at the R Cu site. $c_{R\pm a}^\dagger$ and $c_{R\pm a}$ are defined similarly. Since there is no electron spin coupling to the O atom phonon mode, the electron spin index is dropped in equation G23.

The matrix element between \mathbf{k}' and \mathbf{k} is

$$\langle \phi(\mathbf{k}') | H_\perp(\mathbf{R}) | \phi(\mathbf{k}) \rangle = N_M^{-1} e^{-i(k'-k)R} \left[\delta\epsilon - \delta t(+)(e^{-ik'a} + e^{ika}) - \delta t(-)(e^{ik'a} + e^{-ika}) \right] \quad (\text{G24})$$

The modulus squared is

$$|\langle \phi(\mathbf{k}') | H_\perp(\mathbf{R}) | \phi(\mathbf{k}) \rangle|^2 = N_M^{-2} \left\{ \left\{ \delta\epsilon - [\delta t(+)+\delta t(-)] [\cos(k'a) + \cos(ka)] \right\}^2 + [\delta t(+)-\delta t(-)]^2 [\sin(k'a) - \sin(ka)]^2 \right\} \quad (\text{G25})$$

Define the two functions of \mathbf{k} and \mathbf{k}' , $J_\perp^{(x)}(\mathbf{k}, \mathbf{k}')$ and $J_\perp^{(y)}(\mathbf{k}, \mathbf{k}')$ as

$$\begin{aligned} J_\perp^{(x)}(\mathbf{k}, \mathbf{k}') &= \langle \delta\epsilon^2 \rangle_x - 2 \langle \delta\epsilon [\delta t(+)+\delta t(-)] \rangle_x (\cos k'_x a + \cos k_x a) \\ &\quad + \langle [\delta t(+)+\delta t(-)] \rangle_x (\cos k'_x a + \cos k_x a)^2 \\ &\quad + \langle [\delta t(+)-\delta t(-)] \rangle_x (\sin k'_x a - \sin k_x a)^2, \end{aligned} \quad (\text{G26})$$

$$\begin{aligned} J_\perp^{(y)}(\mathbf{k}, \mathbf{k}') &= \langle \delta\epsilon^2 \rangle_y - 2 \langle \delta\epsilon [\delta t(+)+\delta t(-)] \rangle_y (\cos k'_y a + \cos k_y a) \\ &\quad + \langle [\delta t(+)+\delta t(-)] \rangle_y (\cos k'_y a + \cos k_y a)^2 \\ &\quad + \langle [\delta t(+)-\delta t(-)] \rangle_y (\sin k'_y a - \sin k_y a)^2, \end{aligned} \quad (\text{G27})$$

where $\langle F(\mathbf{R}_\sigma) \rangle_x$ is the average, defined in equation G21, of the function $F(\mathbf{R}_\sigma)$ for each x-axis O phonon mode with position \mathbf{R}_σ as shown in Figure 28. Similarly, $\langle F(\mathbf{R}_\sigma) \rangle_y$ is the average of $F(\mathbf{R}_\sigma)$ over the y-axis O atoms. The expression in equation G27 for $J_\perp^{(y)}$ is identical to the expression for $J_\perp^{(x)}$ in equation G26 with x replaced by y .

From the \mathbf{k} -space versions of equations G3 and G4

$$\lambda_\perp(\mathbf{k}, \mathbf{k}', \omega_n) = \left(\frac{N(0)}{N_M} \right) \left[J_\perp^{(x)}(\mathbf{k}, \mathbf{k}') + J_\perp^{(y)}(\mathbf{k}, \mathbf{k}') \right] \left(\frac{2\omega_{ph}}{\omega_n^2 + \omega_{ph}^2} \right). \quad (\text{G28})$$

3. Contribution to λ from the Phonons Responsible for the the Resistivity

The low-temperature resistivity of $\text{La}_{2-x}\text{Sr}_x\text{CuO}_4$ is the sum of two terms.⁶⁵ One term is linear in T and the other is proportional to T^2 . At high temperatures, both terms become linear in T . Previously, we showed¹³ that the doping evolution of these two terms can be explained by phonon scattering and simple counting of the number of metallic sites and the number of overlapped plaquettes, as a function of doping. The contribution of these phonons on T_c must be included in our Eliashberg calculation.

The power law dependence of the two terms in the resistivity restricts the form of their electron-phonon spectral functions, $\alpha^2 F_1$ and $\alpha^2 F_2$ for the linear and T^2 contributions, respectively. From Fermi's Golden Rule, the electron scattering rate is

$$\frac{1}{\tau(\mathbf{k})} = \frac{2\pi}{\hbar} \sum_{\mathbf{k}'} 2 \int_0^{+\infty} d\Omega \alpha^2 F(\mathbf{k}, \mathbf{k}', \Omega) n_B(\Omega), \quad (\text{G29})$$

where $n_B(\Omega)$ is the Bose-Einstein distribution $n_B(\omega) = 1/[\exp(\omega/T) - 1]$. The factor of two in front of the integral comes from the absorption and emission of phonons. $\alpha^2 F$ is zero for Ω greater than the highest phonon energy.

At high temperatures, $n_B(\Omega) \approx T/\Omega$ leading to $\hbar/\tau(\mathbf{k}) \approx 2\pi\lambda_{\mathbf{k}}T$, where

$$\lambda_{\mathbf{k}} = 2 \int_0^{+\infty} d\Omega \frac{\alpha^2 F(\mathbf{k}, \Omega)}{\Omega}, \quad (\text{G30})$$

and $\alpha^2 F(\mathbf{k}, \Omega) = \sum_{\mathbf{k}'} \alpha^2 F(\mathbf{k}, \mathbf{k}', \Omega)$. $\lambda_{\mathbf{k}}$ is called the mass-enhancement factor.¹⁶ The slope of the high-temperature scattering rate can be obtained from the resistivity. Hence, the mass-enhancement can be computed from experiment.

At low-temperatures, the Bose-Einstein distribution cuts the integral in the scattering rate off at $\Omega \sim T$. If $\alpha^2 F \sim \Omega^n$, then

$$\frac{1}{\tau(\mathbf{k})} \sim \int_0^T d\Omega \frac{\alpha^2 F(\mathbf{k}, \Omega)}{\Omega}(T) \sim T^{n+1}. \quad (\text{G31})$$

The low-temperature T^2 scattering rate is known to be isotropic in \mathbf{k} -space,⁶⁶ and thereby it must scale as $\sim \Omega$ from equation G31. From the low-temperature resistivity experiments⁶⁵, we showed the T^2 resistivity term was proportional to $(1 - N_{4M}/N_{Tot})$, where N_{Tot} is the total number of Cu sites (metallic plus insulating AF sites) and N_{4M} is the number of metallic Cu sites that are in non-overlapping plaquettes. Therefore, $\alpha^2 F_2(\mathbf{k}, \mathbf{k}', \Omega)$ is of the form

$$\alpha^2 F_2(\mathbf{k}, \mathbf{k}', \Omega) = C_2 \left(\frac{\Omega}{\omega_D} \right) \left(1 - \frac{N_{4M}}{N_{Tot}} \right), \quad (\text{G32})$$

where C_2 is a constant to be determined. ω_D is the Debye energy. $\alpha^2 F_2 = 0$, for $\Omega > \omega_D$.

The low-temperature T scattering rate is zero along the diagonals, $k_x = \pm k_y$, and large at $\mathbf{k} = (0, \pm\pi), (\pm\pi, 0)$.⁶⁶ $\alpha^2 F_1$ is independent of Ω from equation G31. The scattering rate in equation G31 logarithmically diverges for small Ω . Hence, it must be cutoff at some minimum, ω_{min} . For temperatures below ω_{min} , the scattering rate cannot be linear in T . Previously, we showed that $\omega_{min} \approx 1$ K.¹³ In this paper, we fix $\omega_{min} = 1$ K. See Appendix F.

The spectral function, $\alpha^2 F_1(\mathbf{k}, \mathbf{k}', \Omega)$, is of the form

$$\alpha^2 F_1(\mathbf{k}, \mathbf{k}', \Omega) = C_1 \left(\frac{N_{4M}}{N_{Tot}} \right) D(\mathbf{k}) D(\mathbf{k}'), \quad \text{for } \omega_{min} < \Omega < \omega_D, \quad (\text{G33})$$

where C_1 is a constant, and $\alpha^2 F_1 = 0$ outside of the range $\omega_{min} < \Omega < \omega_D$.

The anisotropy factor, $D(\mathbf{k})$, is

$$D(\mathbf{k}) = \frac{(\cos(k_x a) - \cos(k_y a))^2}{\langle (\cos(k_x a) - \cos(k_y a))^2 \rangle} \quad (\text{G34})$$

where the denominator is the average over the Fermi surface of the numerator.

The average of a function, $f(\mathbf{k})$, over the Fermi surface is defined as

$$\langle f(\mathbf{k}) \rangle = \frac{\sum_{\mathbf{k}'} \left[\frac{\delta(\epsilon_{\mathbf{k}'} - \epsilon_F)}{N(0)} \right] f(\mathbf{k}')}{\sum_{\mathbf{k}'} \left[\frac{\delta(\epsilon_{\mathbf{k}'} - \epsilon_F)}{N(0)} \right]}. \quad (\text{G35})$$

Thus $\langle D(\mathbf{k}) \rangle = 1$.

The constants C_1 and C_2 can be determined as follows. The average around the Fermi surface of the scattering rate at high-temperatures is $1/\tau = 2\pi\lambda_{tr}T$. From resistivity measurements,⁶⁷ $\lambda_{tr} \approx 0.5$. A fraction $(N_{4M}/N_{Tot})\lambda_{tr}$ of λ_{tr} comes from $\langle \alpha^2 F_1 \rangle$ and the fraction $(1 - N_{4M}/N_{Tot})\lambda_{tr}$ comes from $\langle \alpha^2 F_2 \rangle$ leading to

$$\begin{aligned} \lambda_{tr} \left(1 - \frac{N_{4M}}{N_{Tot}} \right) &= 2 \int_0^{+\infty} d\Omega \frac{\langle \alpha^2 F_2(\mathbf{k}, \mathbf{k}', \Omega) \rangle}{\Omega}, \\ \lambda_{tr} &= 2C_2 \int_0^{\omega_D} \frac{d\Omega}{\omega_D}, \\ \lambda_{tr} &= 2C_2, \end{aligned} \quad (\text{G36})$$

$$\begin{aligned}
\lambda_{tr} \left(\frac{N_{4M}}{N_{Tot}} \right) &= 2 \int_{\omega_{min}}^{\omega_D} d\Omega \frac{\langle \alpha^2 F_1(\mathbf{k}, \mathbf{k}', \Omega) \rangle}{\Omega}, \\
\lambda_{tr} &= 2C_1 \int_{\omega_{min}}^{\omega_D} \frac{d\Omega}{\Omega}, \\
\lambda_{tr} &= C_1 \left[2 \ln \left(\frac{\omega_D}{\omega_{min}} \right) \right].
\end{aligned} \tag{G37}$$

Substituting C_1 and C_2 in terms of λ_{tr} back into $\alpha^2 F_1$ and $\alpha^2 F_2$ yields

$$\alpha^2 F_1(\mathbf{k}, \mathbf{k}', \Omega) = \lambda_{tr} \left[\ln \left(\frac{\omega_D}{\omega_{min}} \right) \right]^{-1} D(\mathbf{k})D(\mathbf{k}') \left(\frac{N_{4M}}{N_{Tot}} \right), \quad \omega_{min} < \Omega < \omega_D, \tag{G38}$$

and

$$\alpha^2 F_2(\mathbf{k}, \mathbf{k}', \Omega) = \frac{1}{2} \lambda_{tr} \left(\frac{\Omega}{\omega_D} \right) \left(1 - \frac{N_{4M}}{N_{Tot}} \right), \quad 0 < \Omega < \omega_D. \tag{G39}$$

$\alpha^2 F_1 = 0$ outside of the range $\omega_{min} < \Omega < \omega_D$ and $\alpha^2 F_2 = 0$ for $\Omega > \omega_D$.

We solve for $\lambda_i(\mathbf{k}, \mathbf{k}', \omega_n)$, for $i = 1, 2$ using the \mathbf{k} -space version of equation G4

$$\lambda_i(\mathbf{k}, \mathbf{k}', \omega_n) = \int_0^{+\infty} d\Omega \alpha^2 F_i(\mathbf{k}, \mathbf{k}', \Omega) \left(\frac{2\Omega}{\omega_n^2 + \Omega^2} \right), \tag{G40}$$

leading to

$$\lambda_1(\mathbf{k}, \mathbf{k}', \omega_n) = \left(\frac{N_{4M}}{N_{Tot}} \right) \lambda_{tr} D(\mathbf{k})D(\mathbf{k}') \left[\frac{\ln \left(\frac{\omega_n^2 + \omega_D^2}{\omega_n^2 + \omega_{min}^2} \right)}{\ln \left(\frac{\omega_D^2}{\omega_{min}^2} \right)} \right] \tag{G41}$$

and

$$\lambda_2(\mathbf{k}, \mathbf{k}', \omega_n) = \left(1 - \frac{N_{4M}}{N_{Tot}} \right) \lambda_{tr} \left[1 - \frac{|\omega_n|}{\omega_D} \tan^{-1} \left(\frac{\omega_D}{|\omega_n|} \right) \right] \tag{G42}$$

4. Generalization of the Eliashberg Equations for Multi-Layer Cuprates

The Eliashberg equations G11, G12, and G13 for a single CuO₂ layer per unit cell are generalized to multi-layer cuprates by changing \mathbf{k} and \mathbf{k}' to $\mathbf{b}\mathbf{k}$ and $\mathbf{b}'\mathbf{k}'$, respectively, in the single layer Eliashberg equations.

$$\begin{aligned}
Z(\mathbf{b}\mathbf{k}, i\omega_n) &= 1 + \frac{\pi T}{|\omega_n|} \sum_{\mathbf{b}'\mathbf{k}'_{n'}}^{|\omega_{n'}| < \omega_c} \left[\frac{\delta(\epsilon_{\mathbf{b}'\mathbf{k}'} - \epsilon_F)}{N(0)} \right] \lambda(\mathbf{b}\mathbf{k}, \mathbf{b}'\mathbf{k}', \omega_n - \omega_{n'}) s_n s_{n'}, \\
Z(\mathbf{b}\mathbf{k}, i\omega_n) \Delta(\mathbf{b}\mathbf{k}, i\omega_n) &= \pi T \\
&\times \sum_{\mathbf{b}'\mathbf{k}'_{n'}}^{|\omega_{n'}| < \omega_c} \frac{1}{|\omega_{n'}|} \left[\frac{\delta(\epsilon_{\mathbf{b}'\mathbf{k}'} - \epsilon_F)}{N(0)} \right] [\lambda(\mathbf{b}\mathbf{k}, \mathbf{b}'\mathbf{k}', \omega_n - \omega_{n'}) - \mu^*(\omega_c)] \Delta(\mathbf{b}'\mathbf{k}', i\omega_{n'}),
\end{aligned} \tag{G43}$$

$$Z(\mathbf{b}\mathbf{k}, -i\omega_n) = Z(\mathbf{b}\mathbf{k}, i\omega_n) = \text{Real Number}, \tag{G44}$$

$$\Delta(\mathbf{b}\mathbf{k}, -i\omega_n) = \Delta(\mathbf{b}\mathbf{k}, i\omega_n) = \text{Real Number}, \tag{G45}$$

where \mathbf{b} and \mathbf{b}' are band indices. They vary from 1 to L , where L is the number of CuO_2 layers per unit cell. A unit cell contains L Cu atoms, one in each layer. The \mathbf{k} vector is a 2D vector. $N(0)$ is the total density of states per spin

$$N(0) = \sum_{\mathbf{b}'\mathbf{k}'} \delta(\epsilon_{\mathbf{b}'\mathbf{k}'} - \epsilon_F). \tag{G46}$$

There is a Bloch \mathbf{k} state for each layer, l , given by $\phi(l\mathbf{k})$. The band eigenfunctions are

$$\psi(\mathbf{b}\mathbf{k}) = \sum_l A_{bl}(\mathbf{k}) \phi(l\mathbf{k}). \tag{G47}$$

The coefficients, $A_{bl}(\mathbf{k})$, are real since the inter-layer hopping matrix elements are real. The matrix element for hopping between adjacent layers is

$$\langle \phi(l \pm 1\mathbf{k}') | H_{inter} | \phi(l\mathbf{k}) \rangle = -t(l \pm 1, l, \mathbf{k}) \delta_{\mathbf{k}'\mathbf{k}} \tag{G48}$$

where

$$t(l \pm 1, l, \mathbf{k}) = \alpha t_z (1/4) [\cos(k_x a) - \cos(k_y a)]^2, \tag{G49}$$

and α is the product of the fraction of metallic sites in layers l and $l \pm 1$. See Appendix F Table II.

The eigenvectors $\psi(\mathbf{b}\mathbf{k})$ of equations G47 and G48 are independent of the magnitude of $t(l \pm 1, l, \mathbf{k})$. Thus $A_{bl}(\mathbf{k})$ is independent of \mathbf{k} ,

$$A_{bl}(\mathbf{k}) = A_{bl}. \quad (\text{G50})$$

The eigenstates, $\psi(\mathbf{bk})$, are normalized leading to

$$\sum_{\mathbf{b}} A_{bl'} A_{bl} = \delta_{ll'}, \quad (\text{G51})$$

$$\sum_l A_{b'l} A_{bl} = \delta_{b'b}. \quad (\text{G52})$$

The electron-phonon spectral function $\alpha^2 F_2(\mathbf{bk}, \mathbf{b}'\mathbf{k}', \Omega)$ is

$$\alpha^2 F_2(\mathbf{bk}, \mathbf{b}'\mathbf{k}', \Omega) = \frac{1}{2} \lambda_{tr} \left(\frac{\Omega}{\omega_D} \right) (1 - n_{4M}), \quad 0 < \Omega < \omega_D, \quad (\text{G53})$$

where

$$n_{4M}(l) = \frac{N_{4M}(l)}{N_{xy}}, \quad (\text{G54})$$

$$n_{4M} = \frac{1}{L} \sum_l n_{4M}(l). \quad (\text{G55})$$

$N_{4M}(l)$ is the number of metallic Cu sites in layer l that are in non-overlapping plaquettes, L is the total number of CuO_2 layers per unit cell, and N_{xy} is the total number of Cu sites (metallic plus insulating AF) in a single CuO_2 layer. Hence, LN_{xy} is the total number of Cu sites in the crystal and n_{4M} is the total fraction of metallic Cu sites over all the CuO_2 layers. $\alpha^2 F_2 = 0$ for $\Omega > \omega_D$.

For the electron-phonon spectral function, $\alpha^2 F_1$, that leads to the low-temperature linear resistivity, define the anisotropy factor, $D(\mathbf{bk})$ as

$$D(\mathbf{bk}) = \frac{(\cos(k_x a) - \cos(k_y a))^2}{\langle (\cos(k_x a) - \cos(k_y a))^2 \rangle} \quad (\text{G56})$$

where the denominator is the average over all the L Fermi surfaces of the numerator.

The average of a function, $f(\mathbf{bk})$, over all the Fermi surfaces is defined as

$$\langle f(\mathbf{bk}) \rangle = \frac{\sum_{b'k'} \left[\frac{\delta(\epsilon_{\mathbf{b}'\mathbf{k}'} - \epsilon_F)}{N(0)} \right] f(\mathbf{b}'\mathbf{k}')}{\sum_{b'k'} \left[\frac{\delta(\epsilon_{\mathbf{b}'\mathbf{k}'} - \epsilon_F)}{N(0)} \right]}. \quad (\text{G57})$$

The phonon modes in $\alpha^2 F_1$ are 2D. Hence, the form of the spectral function between layers l and l' is of the form,

$$\alpha^2 F_1(lk, l'k', \Omega) = \delta_{ll'} \left[\ln \left(\frac{\omega_D^2}{\omega_{min}^2} \right) \right]^{-1} n_{4M}(l) D(\mathbf{k}) D(\mathbf{k}'). \quad (\text{G58})$$

Expanding the eigenstates $\psi(\mathbf{bk})$ in terms of $\phi(l\mathbf{k})$ from equation G47 leads to

$$\alpha^2 F_1(\mathbf{bk}, \mathbf{b}'\mathbf{k}', \Omega) = \left\{ \sum_l |A_{bl}|^2 |A_{b'l'}|^2 n_{4M}(l) \right\} \lambda_{tr} \left[\ln \left(\frac{\omega_D^2}{\omega_{min}^2} \right) \right]^{-1} D(\mathbf{bk}) D(\mathbf{b}'\mathbf{k}'), \quad (\text{G59})$$

where $\omega_{min} < \Omega < \omega_D$. $\alpha^2 F_1 = 0$, for $\Omega < \omega_{min}$ or $\Omega > \omega_D$.

Hence,

$$\lambda_1(\mathbf{bk}, \mathbf{b}'\mathbf{k}', \omega_n) = \left\{ \sum_l |A_{bl}|^2 |A_{b'l'}|^2 n_{4M}(l) \right\} \lambda_{tr} D(\mathbf{bk}) D(\mathbf{b}'\mathbf{k}') \left[\frac{\ln \left(\frac{\omega_n^2 + \omega_D^2}{\omega_n^2 + \omega_{min}^2} \right)}{\ln \left(\frac{\omega_D^2}{\omega_{min}^2} \right)} \right] \quad (\text{G60})$$

and

$$\lambda_2(\mathbf{bk}, \mathbf{b}'\mathbf{k}', \omega_n) = (1 - n_{4M}) \lambda_{tr} \left[1 - \frac{|\omega_n|}{\omega_D} \tan^{-1} \left(\frac{\omega_D}{|\omega_n|} \right) \right] \quad (\text{G61})$$

The multi-layer expressions for $\lambda_{surf}(\mathbf{bk}, \mathbf{b}'\mathbf{k}', \omega_n)$ and $\lambda_{\perp}(\mathbf{bk}, \mathbf{b}'\mathbf{k}', \omega_n)$ are similar to their single-layer counterparts with a modified definition for the averaging in their respective $J^{(x)}$ and $J^{(y)}$ functions.

$$\begin{aligned} J_{surf}^{(x)}(\mathbf{bk}, \mathbf{b}'\mathbf{k}') &= \langle (\delta\epsilon_L + \delta\epsilon_R)^2 \rangle_x \cos^2 \frac{1}{2}(k'_x - k_x) a \\ &\quad - 2 \langle \delta t (\delta\epsilon_L + \delta\epsilon_R) \rangle_x \cos \frac{1}{2}(k'_x - k_x) a \cos \frac{1}{2}(k'_x + k_x) a \\ &\quad + \langle \delta t^2 \rangle_x \cdot 4 \cos^2 \frac{1}{2}(k'_x + k_x) a + \langle (\delta\epsilon_L - \delta\epsilon_R)^2 \rangle_x \sin^2 \frac{1}{2}(k'_x - k_x) a, \end{aligned} \quad (\text{G62})$$

$$\begin{aligned} J_{surf}^{(y)}(\mathbf{bk}, \mathbf{b}'\mathbf{k}') &= \langle (\delta\epsilon_L + \delta\epsilon_R)^2 \rangle_y \cos^2 \frac{1}{2}(k'_y - k_y) a \\ &\quad - 2 \langle \delta t (\delta\epsilon_L + \delta\epsilon_R) \rangle_y \cos \frac{1}{2}(k'_y - k_y) a \cos \frac{1}{2}(k'_y + k_y) a \\ &\quad + \langle \delta t^2 \rangle_y \cdot 4 \cos^2 \frac{1}{2}(k'_y + k_y) a + \langle (\delta\epsilon_L - \delta\epsilon_R)^2 \rangle_y \sin^2 \frac{1}{2}(k'_y - k_y) a, \end{aligned} \quad (\text{G63})$$

where $\langle F(\mathbf{R}_\sigma) \rangle_x$ is the multi-layer average of the function $F(\mathbf{R}_\sigma)$ defined for each planar surface O on the x-axis with position \mathbf{R}_σ as shown in Figure 27,

$$\langle F(\mathbf{R}_\sigma) \rangle = \sum_l |A_{bl}|^2 |A_{b'l}|^2 \langle F_l(\mathbf{R}_\sigma) \rangle, \quad (\text{G64})$$

and $\langle F_l(\mathbf{R}_\sigma) \rangle_x$ is the average over layer l , as defined in equation G21. Similarly for $\langle F(\mathbf{R}_\sigma) \rangle_y$. The expression in equation G63 for $J_{surf}^{(y)}$ is identical to the expression for $J_{surf}^{(x)}$ in equation G62 with x replaced by y .

Hence, $\lambda_{surf}(\mathbf{b}\mathbf{k}, \mathbf{b}'\mathbf{k}', \omega_n)$ is

$$\lambda_{surf}(\mathbf{k}, \mathbf{k}', \omega_n) = \left(\frac{N(0)}{N_M} \right) \left[J_{surf}^{(x)}(\mathbf{k}, \mathbf{k}') + J_{surf}^{(y)}(\mathbf{k}, \mathbf{k}') \right] \left(\frac{2\omega_{ph}}{\omega_n^2 + \omega_{ph}^2} \right), \quad (\text{G65})$$

where N_M is the total number of metallic Cu sites, $N_M = \sum_l N_{lM}$, and N_{lM} is the total number of metallic Cu sites in layer l .

For $\lambda_\perp(\mathbf{b}\mathbf{k}, \mathbf{b}'\mathbf{k}', \omega_n)$, the corresponding $J_\perp^{(x)}$ and $J_\perp^{(y)}$ functions are

$$\begin{aligned} J_\perp^{(x)}(\mathbf{b}\mathbf{k}, \mathbf{b}'\mathbf{k}') &= \langle \delta\epsilon^2 \rangle_x - 2 \langle \delta\epsilon [\delta t(+)] + \delta t(-) \rangle_x (\cos k'_x a + \cos k_x a) \\ &\quad + \langle [\delta t(+)] + \delta t(-) \rangle_x (\cos k'_x a + \cos k_x a)^2 \\ &\quad + \langle [\delta t(+)] - \delta t(-) \rangle_x (\sin k'_x a - \sin k_x a)^2, \end{aligned} \quad (\text{G66})$$

$$\begin{aligned} J_\perp^{(y)}(\mathbf{b}\mathbf{k}, \mathbf{b}'\mathbf{k}') &= \langle \delta\epsilon^2 \rangle_y - 2 \langle \delta\epsilon [\delta t(+)] + \delta t(-) \rangle_y (\cos k'_y a + \cos k_y a) \\ &\quad + \langle [\delta t(+)] + \delta t(-) \rangle_y (\cos k'_y a + \cos k_y a)^2 \\ &\quad + \langle [\delta t(+)] - \delta t(-) \rangle_y (\sin k'_y a - \sin k_y a)^2. \end{aligned} \quad (\text{G67})$$

All averages in equations G66 and G67 are defined in equation G64.

Hence, $\lambda_\perp(\mathbf{b}\mathbf{k}, \mathbf{b}'\mathbf{k}', \omega_n)$ is

$$\lambda_\perp(\mathbf{b}\mathbf{k}, \mathbf{b}'\mathbf{k}', \omega_n) = \left(\frac{N(0)}{N_M} \right) \left[J_\perp^{(x)}(\mathbf{b}\mathbf{k}, \mathbf{b}'\mathbf{k}') + J_\perp^{(y)}(\mathbf{b}\mathbf{k}, \mathbf{b}'\mathbf{k}') \right] \left(\frac{2\omega_{ph}}{\omega_n^2 + \omega_{ph}^2} \right). \quad (\text{G68})$$

5. Computational Details

The band structure, $\epsilon_{\mathbf{k}}$, and all the parameters used to solve the Eliashberg equations for T_c are described in Appendix F. Here, we discuss the computational issues necessary to obtain an accurate T_c .

The two planar interface O atom phonon modes in Figure 12 require averaging products of pairs of parameters ($\delta\epsilon_L$, $\delta\epsilon_R$, and δt for λ_{surf} , and $\delta\epsilon$ and $\delta t(\pm)$ for λ_{\perp}) over the lattice as seen in equations G19, G20, G26, G27, G62, G63, G66, and G67. These parameters vary depending on the environment of the Cu atoms, as shown in Figure 12.

For each doping value, we generate a 2000×2000 lattice of doped plaquettes. All O atoms that contribute to λ_{surf} and λ_{\perp} are identified along with the nature of the corresponding Cu sites (edge, convex, or concave, as shown in Figure 12). All the product averages are computed. Ensembles of 2000×2000 lattices can be generated to obtain more accurate product averages. We found that a single 2000×2000 doped lattice is large enough to obtain all the products to an accuracy of less than 1 %.

All four electron-phonon pairing functions, λ_1 , λ_2 , λ_{surf} , and λ_{\perp} can be written in the following product form $\lambda(\mathbf{k}, \mathbf{k}', \omega_n) = \lambda'(\mathbf{k}, \mathbf{k}')F(\omega_n)$. The product separation, $\lambda = \lambda'F$, leads to a large reduction in the storage requirements because λ' and F can be computed once and saved, and the product computed on the fly.

We discretize the Fermi surface by choosing 10 uniformly spaced (in angle) \mathbf{k} -points in the 45° wedge bounded by the vectors along the x-axis, $(\pi, 0)$, and the diagonal, (π, π) , leading to a total of 80 \mathbf{k} -points over the full Fermi surface. Increasing the number of \mathbf{k} -points further led to < 0.1 K change in the calculated T_c .

Fermi surface weights, $W_{\mathbf{bk}}$, are computed at each \mathbf{bk} -point using the Fermi velocity evaluated from the band structure, $\epsilon_{\mathbf{k}}$. By rescaling the gap function, $\Delta(\mathbf{bk}, \omega_n)$,

$$\Delta'(\mathbf{bk}, \omega_n) = \left[\frac{W_{\mathbf{bk}}}{|2n + 1|} \right]^{\frac{1}{2}} \Delta(\mathbf{bk}, \omega_n) \quad (\text{G69})$$

the Eliashberg equations can be turned into an eigenvalue equation with a real symmetric matrix.¹⁶ Since T_c occurs when the largest eigenvalue reaches one, we can perform a Lanczos projection. We compute T_c by bracketing. All the T_c values found in this paper are accurate to ± 0.3 K. For approximate timings, a full T_c -dome is computed on a small workstation in $\approx 5 - 10$ minutes.

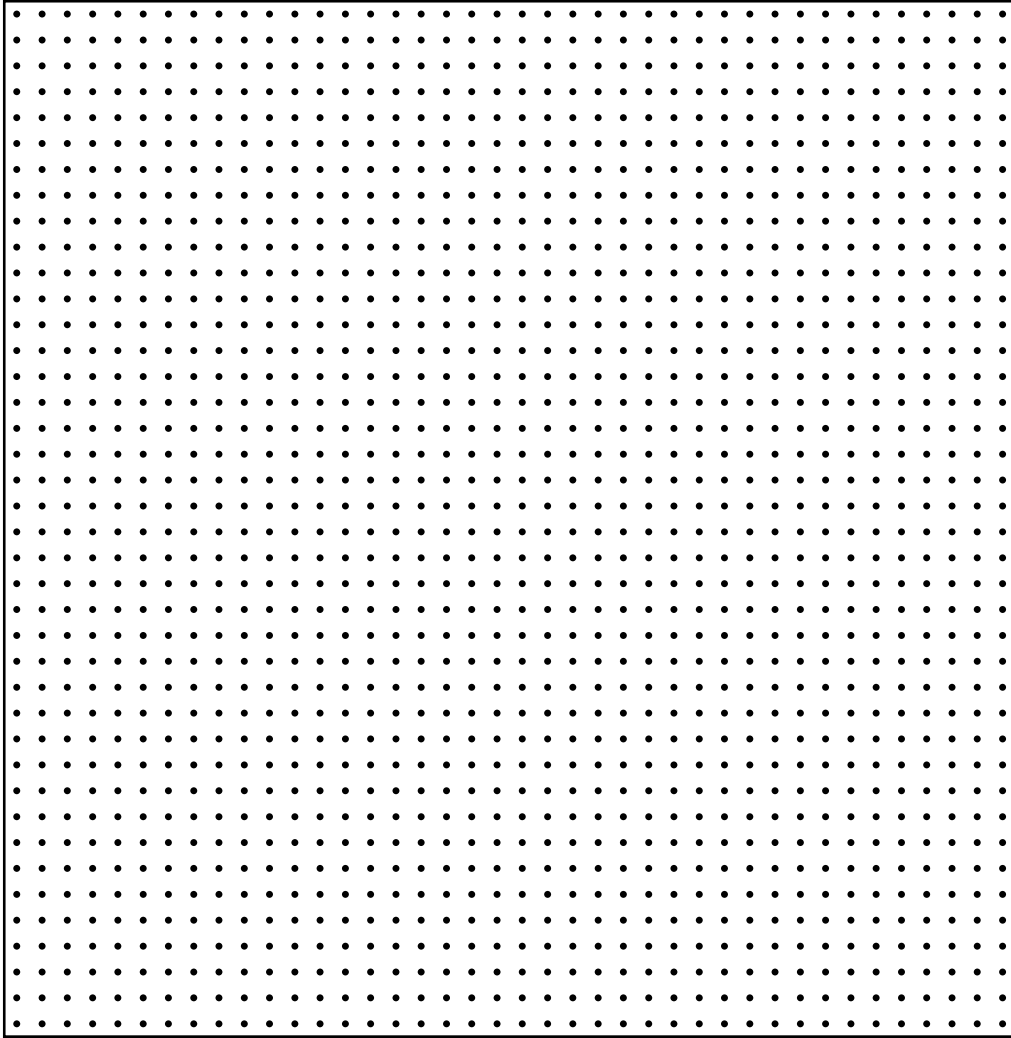


Figure S0 ($x = 0.00$): Plaquette doping of a 40×40 square CuO_2 lattice. Only the Cu sites are shown. The black dots are undoped AF Cu sites. The material is a spin-1/2 antiferromagnet (AF).

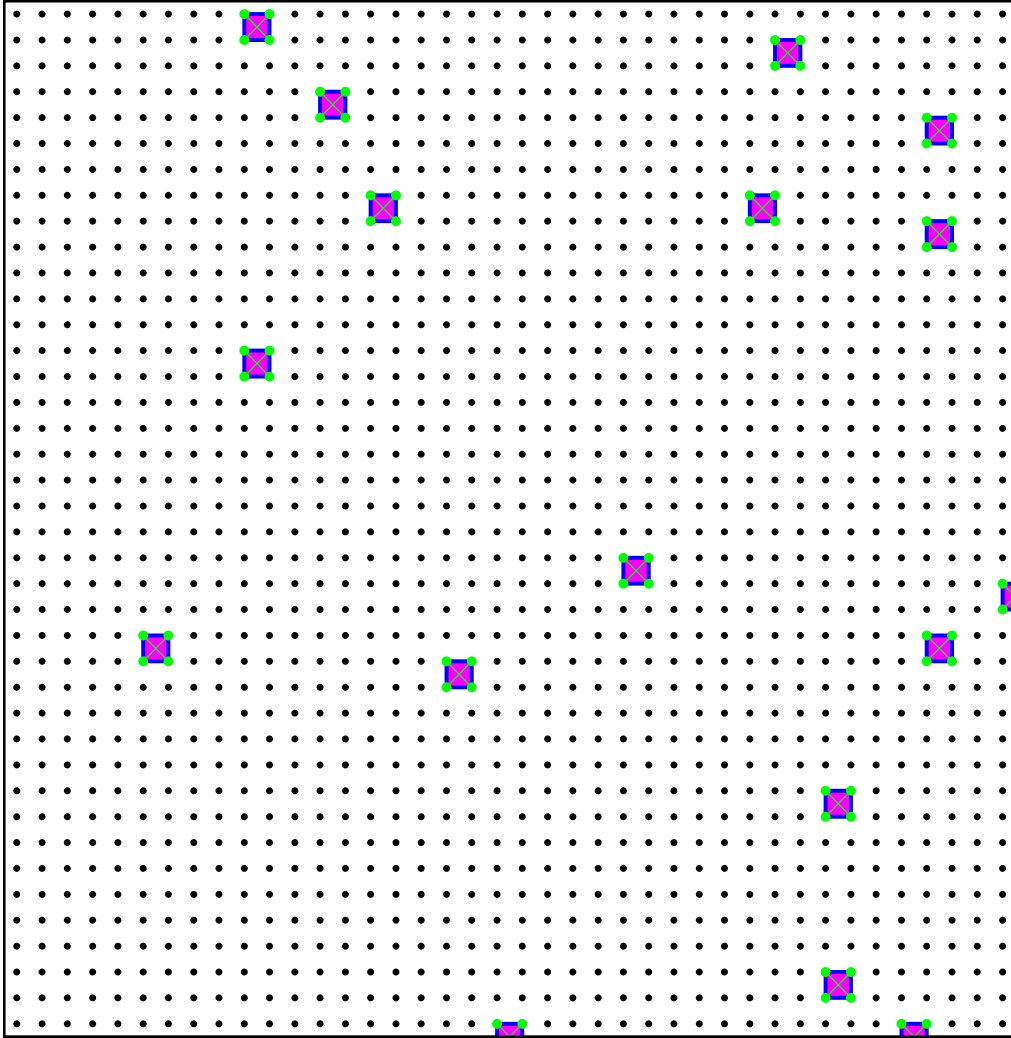


Figure S1 ($x = 0.01$): Plaquette doping of a 40×40 square CuO_2 lattice. Only the Cu sites are shown. The black dots are undoped AF Cu sites. The blue squares are isolated plaquettes (no neighboring plaquette). There are only isolated plaquettes. The magenta overlay represents metallic delocalization of the planar Cu $d_{x^2-y^2}$ and O p_σ orbitals inside each plaquette. Fluctuating dumbbells are shown in every plaquette. There is no plaquette overlap at this doping.

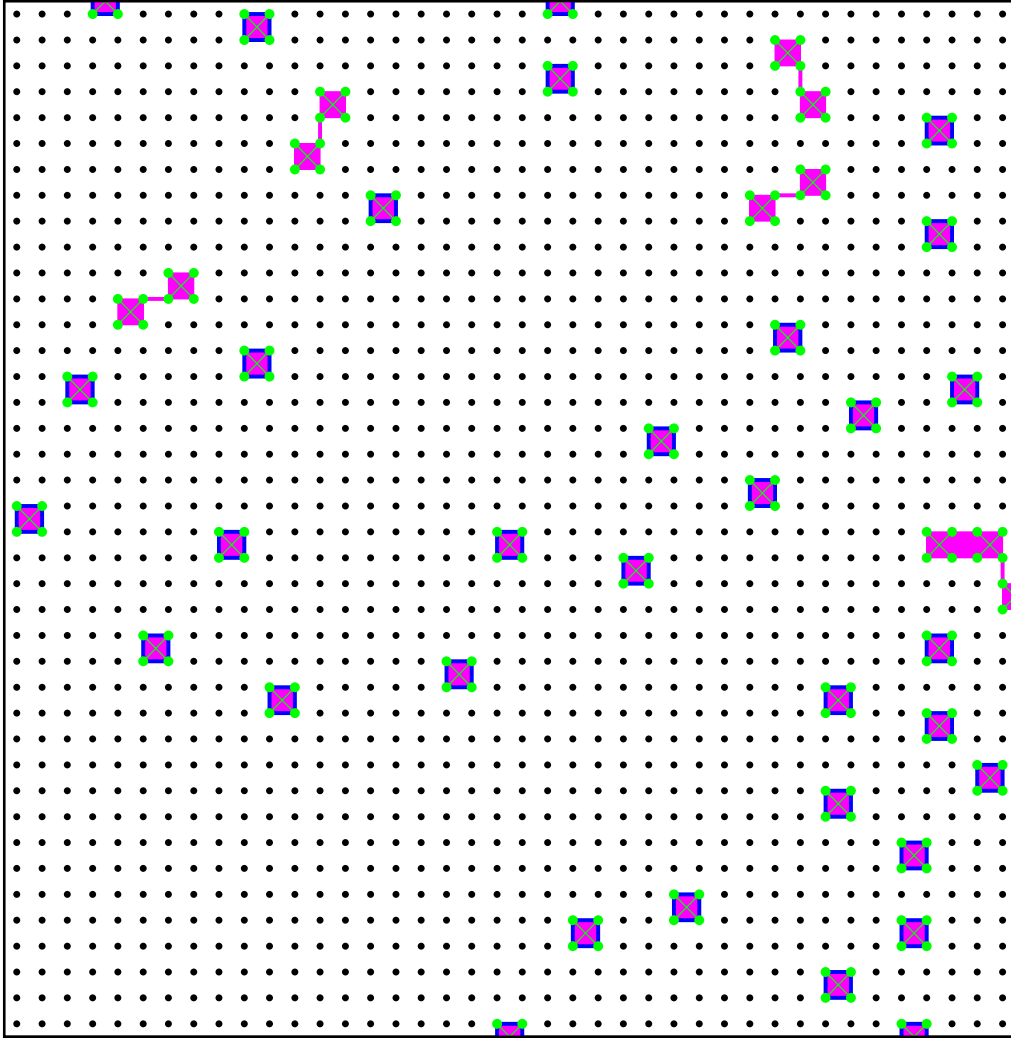


Figure S2 ($x = 0.02$): Plaquette doping of a 40×40 square CuO_2 lattice. Only the Cu sites are shown. The black dots are undoped AF Cu sites. The blue squares are isolated plaquettes (no neighboring plaquette). A few magenta plaquette clusters are formed. These magenta clusters are smaller than the Cooper pair coherence length and do not contribute to superconducting pairing. The magenta overlay represents metallic delocalization of the planar Cu $d_{x^2-y^2}$ and O p_σ orbitals. Fluctuating dumbbells are shown in every plaquette. There is no plaquette overlap at this doping.

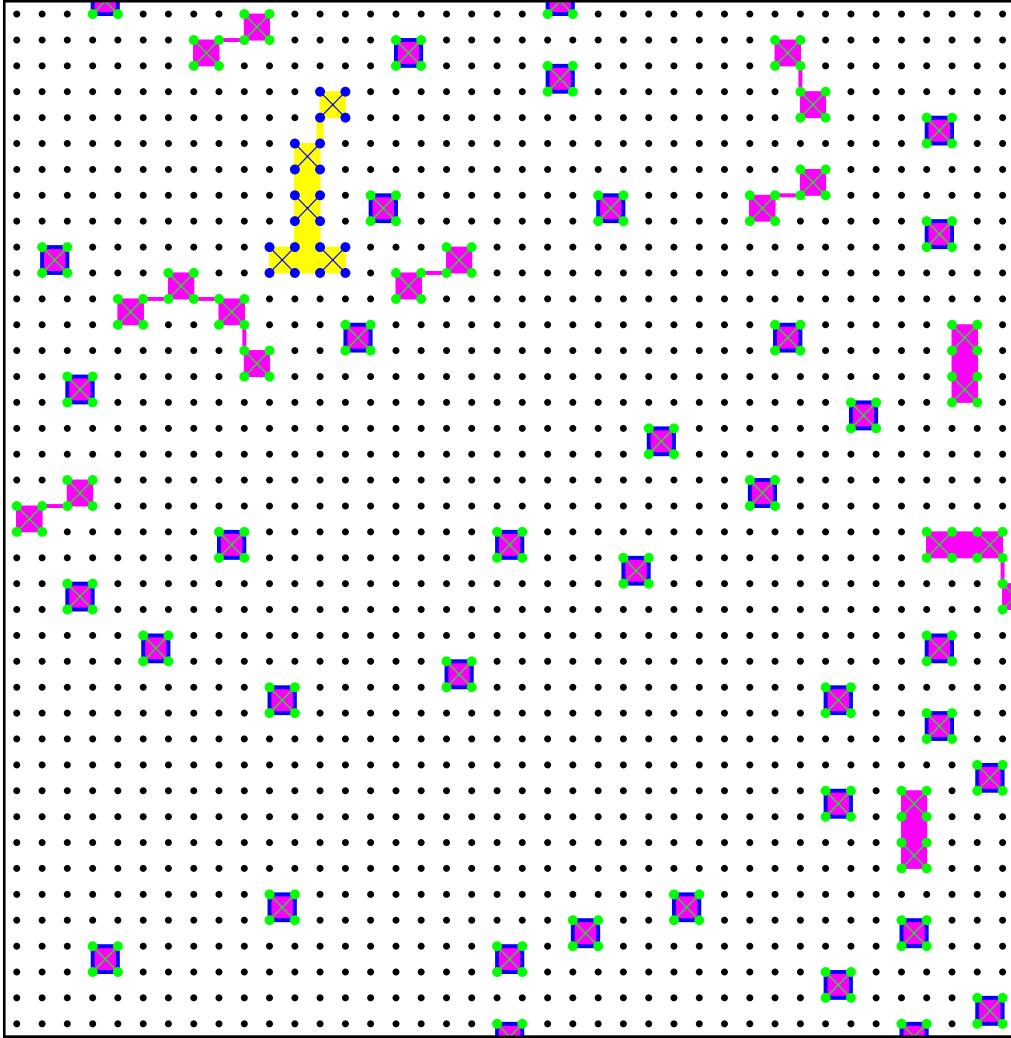


Figure S3 ($x = 0.03$): Plaquette doping of a 40×40 square CuO_2 lattice. Only the Cu sites are shown. The black dots are undoped AF Cu sites. The blue squares are isolated plaquettes (no neighboring plaquette). The yellow plaquette clusters are comprised of more than 4 plaquettes and contribute to the superconducting pairing because they are larger than the coherence length. The yellow overlay represents the metallic region comprised of planar Cu $d_{x^2-y^2}$ and planar O p_σ character. The magenta clusters are smaller than the Cooper pair coherence length and do not contribute to superconducting pairing. The magenta overlay represents metallic delocalization of the planar Cu $d_{x^2-y^2}$ and O p_σ orbitals. Fluctuating dumbbells are shown in every plaquette. There is no plaquette overlap at this doping.

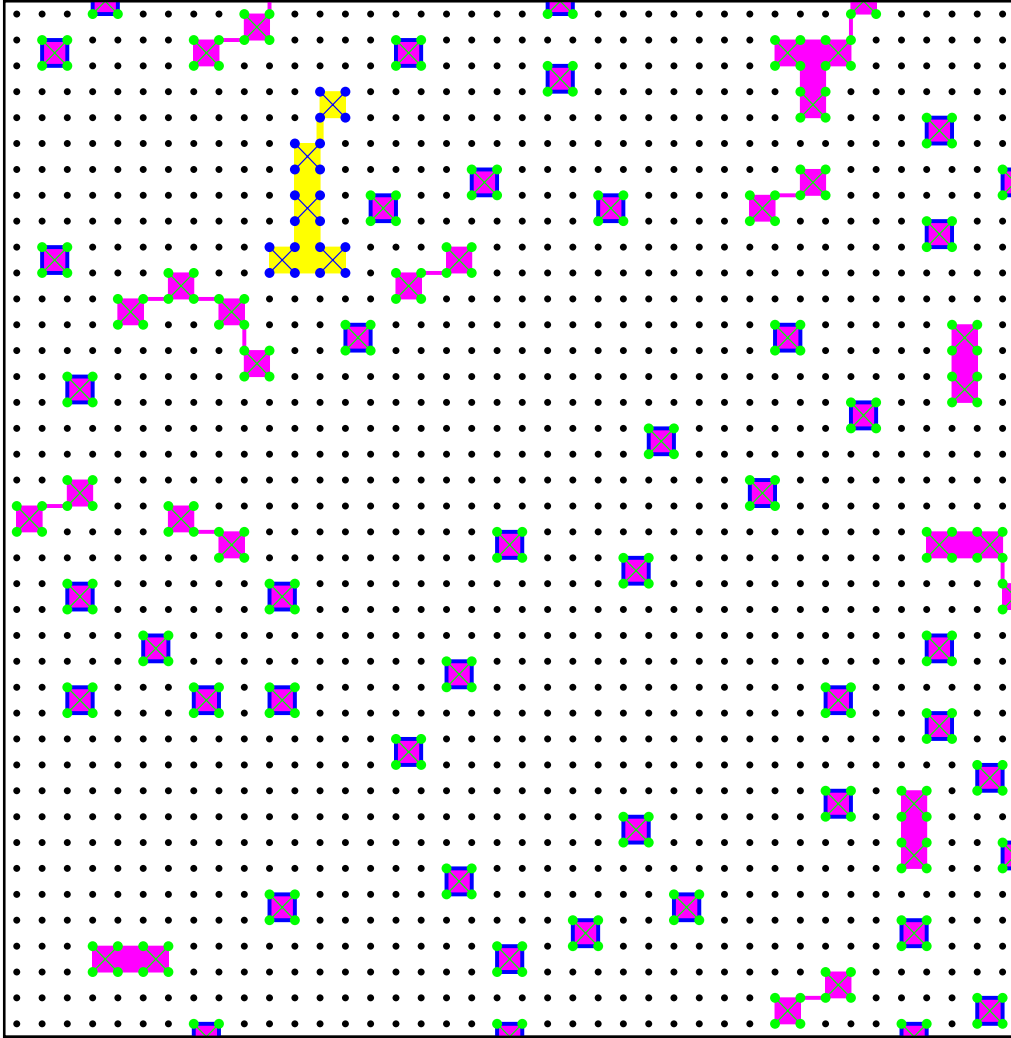


Figure S4 ($x = 0.04$): Plaquette doping of a 40×40 square CuO_2 lattice. Only the Cu sites are shown. The black dots are undoped AF Cu sites. The blue squares are isolated plaquettes (no neighboring plaquette). The yellow plaquette clusters are comprised of more than 4 plaquettes and contribute to the superconducting pairing because they are larger than the coherence length. The yellow overlay represents the metallic region comprised of planar Cu $d_{x^2-y^2}$ and planar O p_σ character. The magenta clusters are smaller than the Cooper pair coherence length and do not contribute to superconducting pairing. The magenta overlay represents metallic delocalization of the planar Cu $d_{x^2-y^2}$ and O p_σ orbitals. Fluctuating dumbbells are shown in every plaquette. There is no plaquette overlap at this doping.

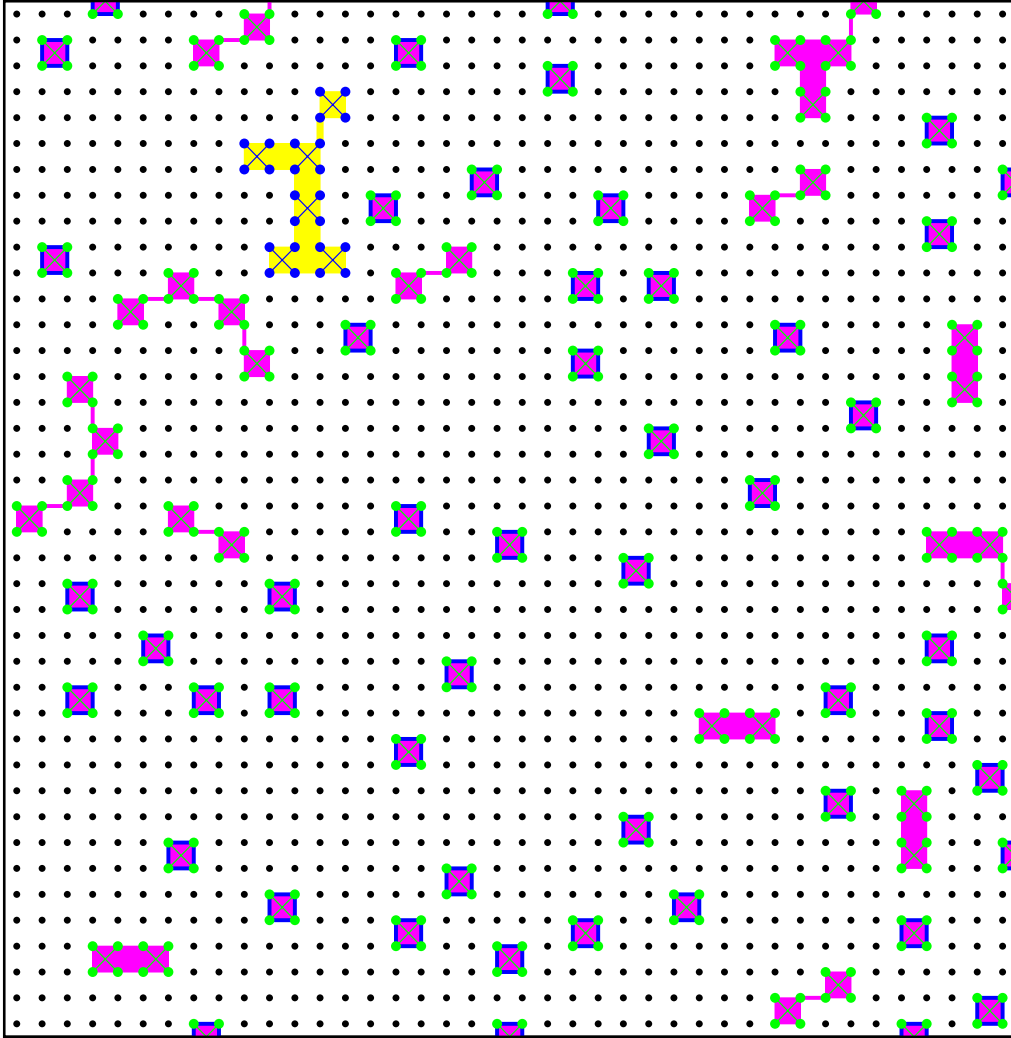


Figure S5 ($x = 0.05$): Plaquette doping of a 40×40 square CuO_2 lattice. Only the Cu sites are shown. The black dots are undoped AF Cu sites. The blue squares are isolated plaquettes (no neighboring plaquette). The yellow plaquette clusters are comprised of more than 4 plaquettes and contribute to the superconducting pairing because they are larger than the coherence length. The yellow overlay represents the metallic region comprised of planar Cu $d_{x^2-y^2}$ and planar O p_σ character. The magenta clusters are smaller than the Cooper pair coherence length and do not contribute to superconducting pairing. The magenta overlay represents metallic delocalization of the planar Cu $d_{x^2-y^2}$ and O p_σ orbitals. Fluctuating dumbbells are shown in every plaquette. There is no plaquette overlap at this doping. The number of isolated plaquettes peaks at this doping.

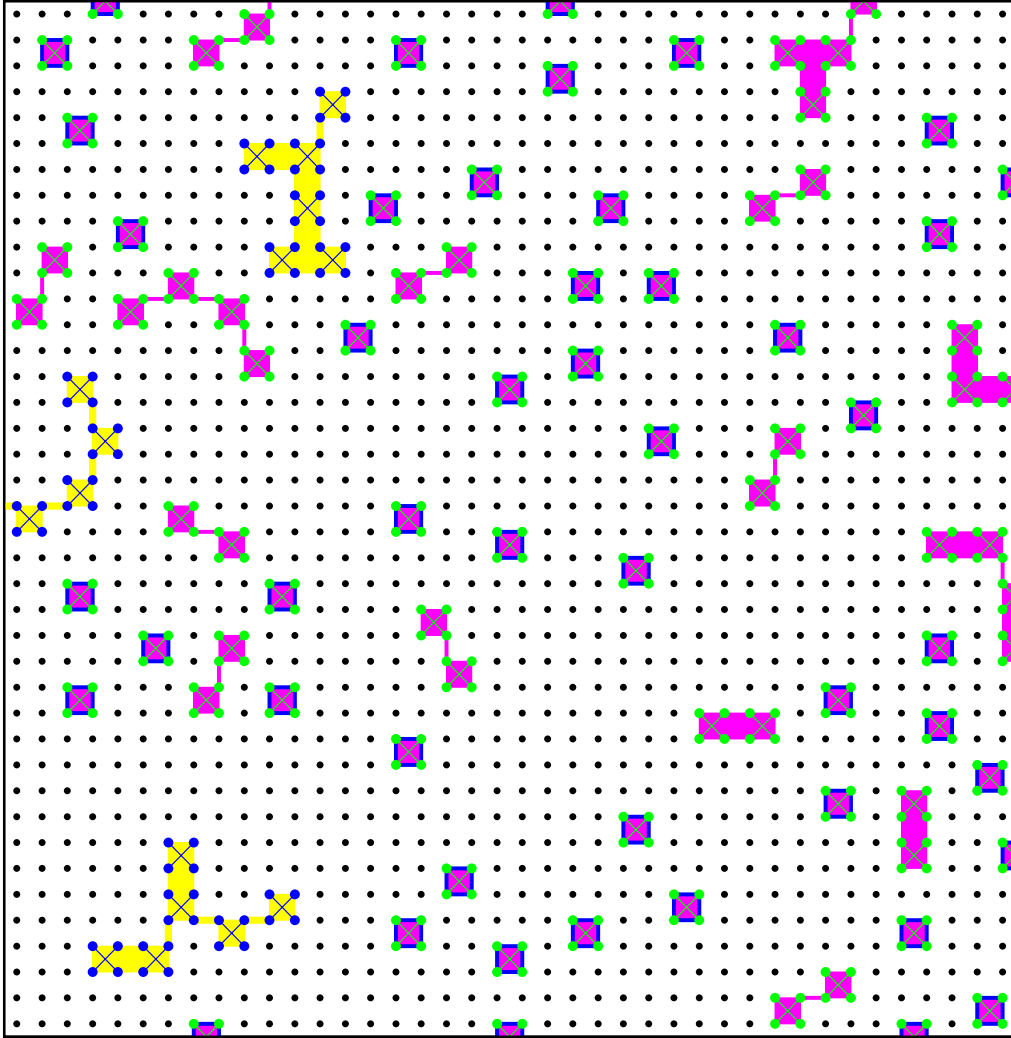


Figure S6 ($x = 0.06$): Plaquette doping of a 40×40 square CuO_2 lattice. Only the Cu sites are shown. The black dots are undoped AF Cu sites. The blue squares are isolated plaquettes (no neighboring plaquette). The yellow plaquette clusters are comprised of more than 4 plaquettes and contribute to the superconducting pairing because they are larger than the coherence length. The yellow overlay represents the metallic region comprised of planar Cu $d_{x^2-y^2}$ and planar O p_σ character. The magenta clusters are smaller than the Cooper pair coherence length and do not contribute to superconducting pairing. The magenta overlay represents metallic delocalization of the planar Cu $d_{x^2-y^2}$ and O p_σ orbitals. Fluctuating dumbbells are shown in every plaquette. There is no plaquette overlap at this doping.

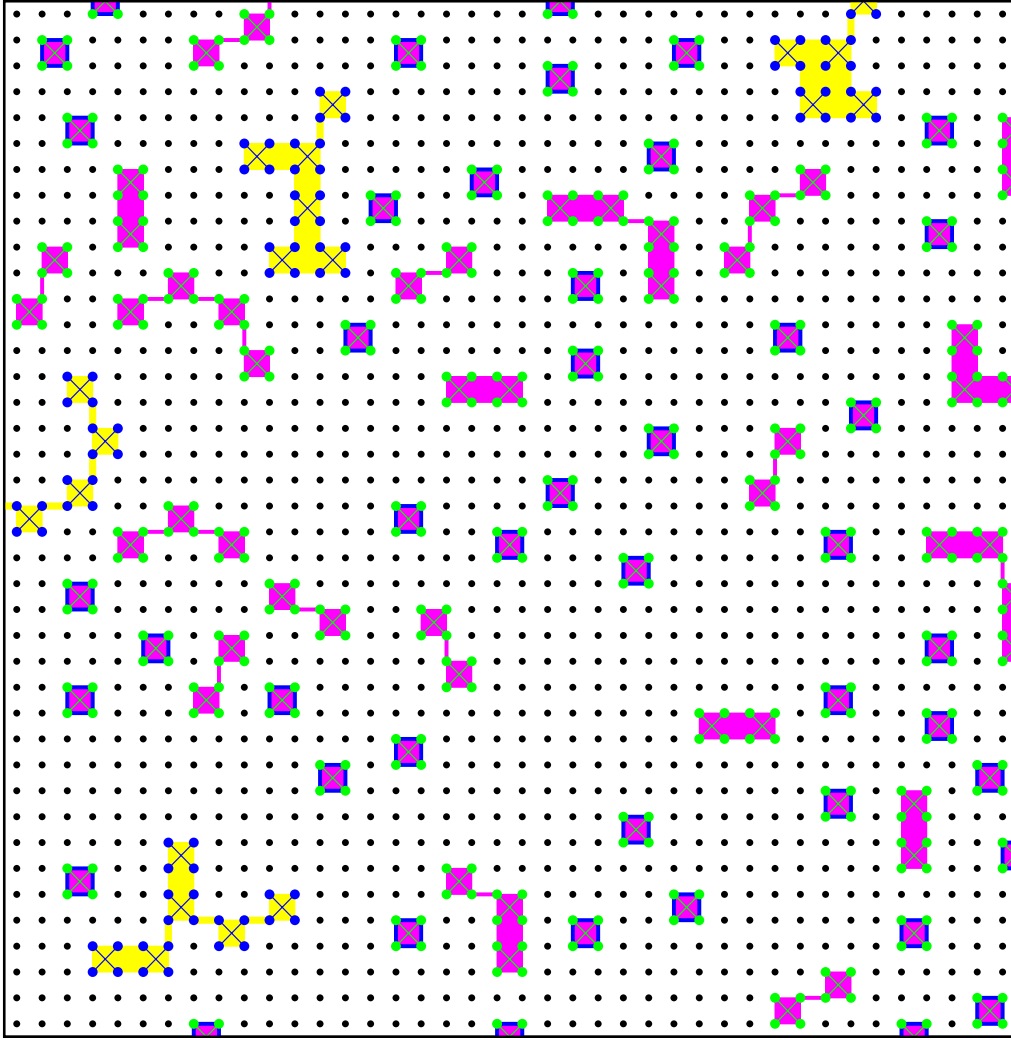


Figure S7 ($x = 0.07$): Plaquette doping of a 40×40 square CuO_2 lattice. Only the Cu sites are shown. The black dots are undoped AF Cu sites. The blue squares are isolated plaquettes (no neighboring plaquette). The yellow plaquette clusters are comprised of more than 4 plaquettes and contribute to the superconducting pairing because they are larger than the coherence length. The yellow overlay represents the metallic region comprised of planar Cu $d_{x^2-y^2}$ and planar O p_σ character. The magenta clusters are smaller than the Cooper pair coherence length and do not contribute to superconducting pairing. The magenta overlay represents metallic delocalization of the planar Cu $d_{x^2-y^2}$ and O p_σ orbitals. Fluctuating dumbbells are shown in every plaquette. There is no plaquette overlap at this doping.

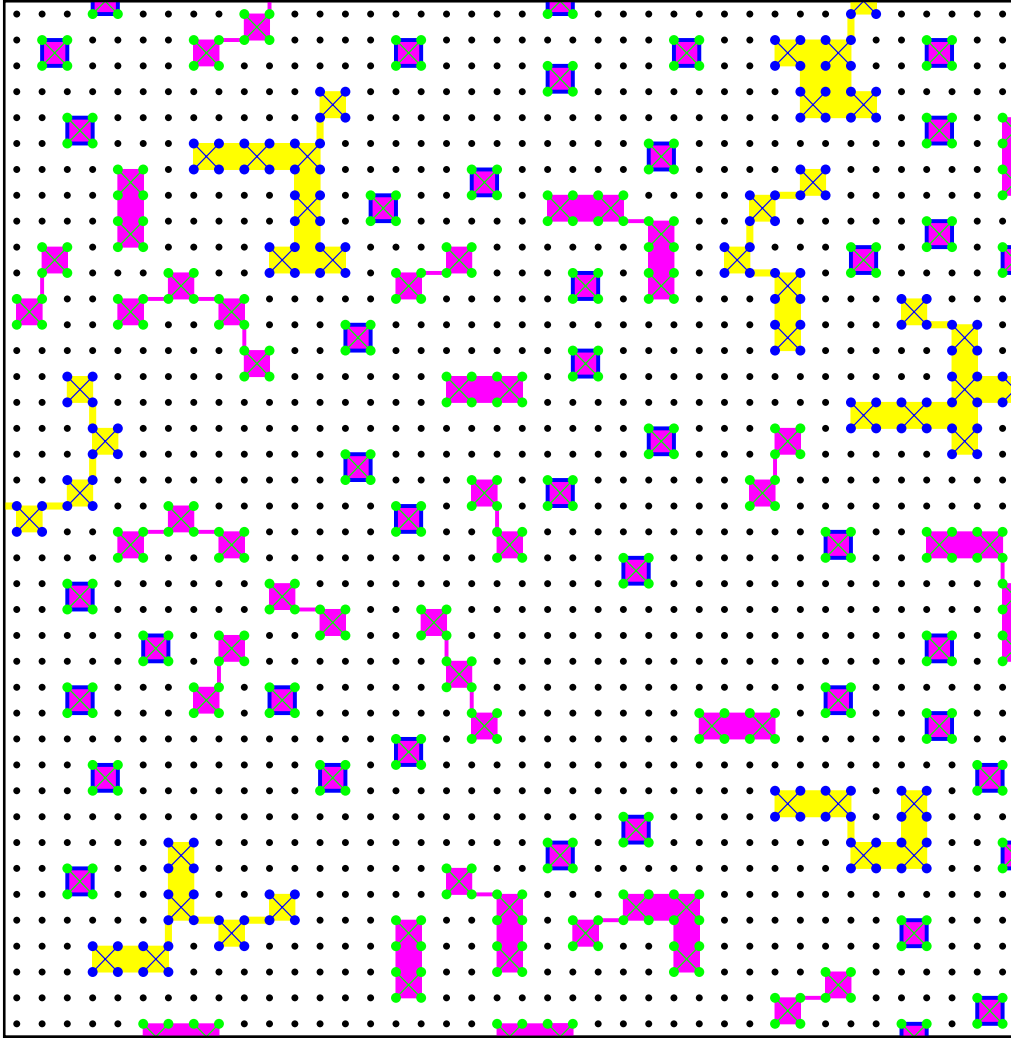


Figure S8 ($x = 0.08$): Plaquette doping of a 40×40 square CuO_2 lattice. Only the Cu sites are shown. The black dots are undoped AF Cu sites. The blue squares are isolated plaquettes (no neighboring plaquette). The yellow plaquette clusters are comprised of more than 4 plaquettes and contribute to the superconducting pairing because they are larger than the coherence length. The yellow overlay represents the metallic region comprised of planar Cu $d_{x^2-y^2}$ and planar O p_σ character. The magenta clusters are smaller than the Cooper pair coherence length and do not contribute to superconducting pairing. The magenta overlay represents metallic delocalization of the planar Cu $d_{x^2-y^2}$ and O p_σ orbitals. Fluctuating dumbbells are shown in every plaquette. There is no plaquette overlap at this doping.

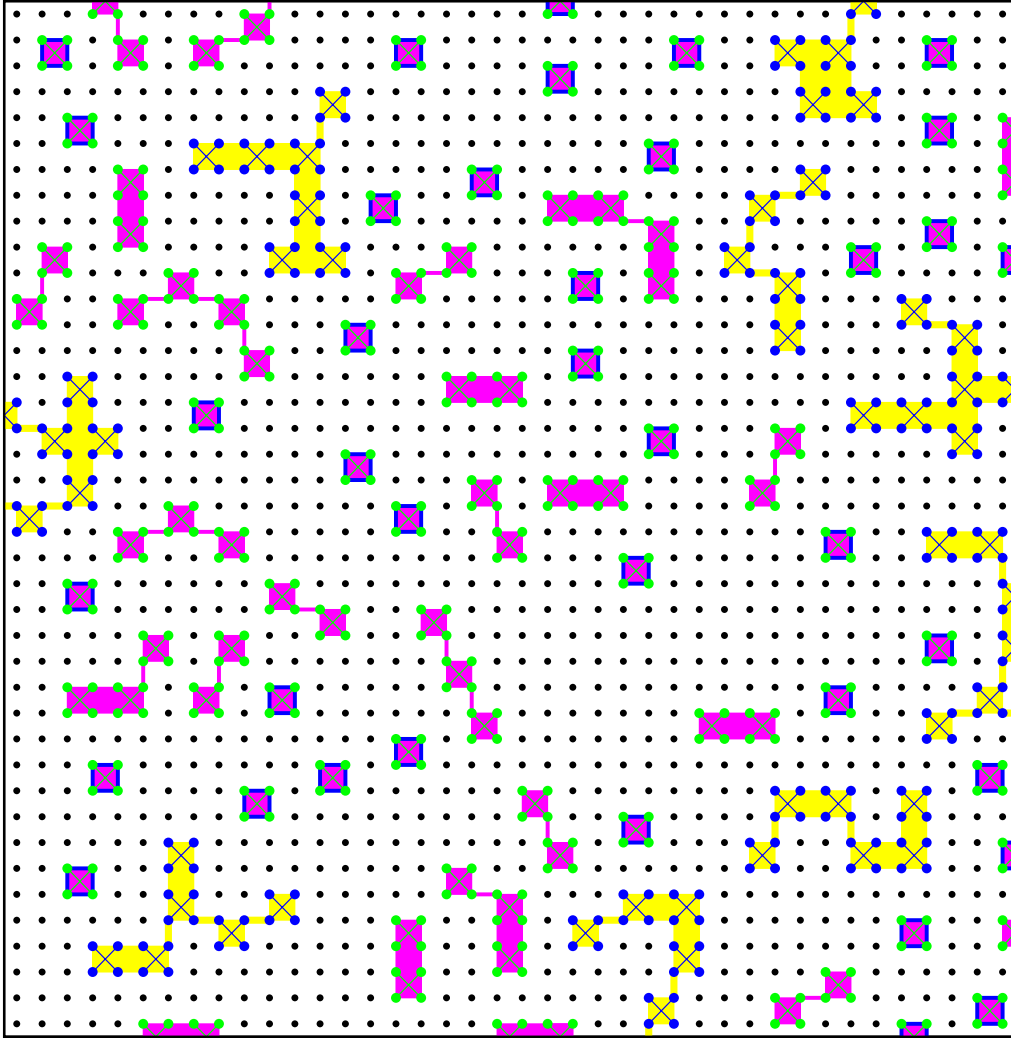


Figure S9 ($x = 0.09$): Plaquette doping of a 40×40 square CuO_2 lattice. Only the Cu sites are shown. The black dots are undoped AF Cu sites. The blue squares are isolated plaquettes (no neighboring plaquette). The yellow plaquette clusters are comprised of more than 4 plaquettes and contribute to the superconducting pairing because they are larger than the coherence length. The yellow overlay represents the metallic region comprised of planar Cu $d_{x^2-y^2}$ and planar O p_σ character. The magenta clusters are smaller than the Cooper pair coherence length and do not contribute to superconducting pairing. The magenta overlay represents metallic delocalization of the planar Cu $d_{x^2-y^2}$ and O p_σ orbitals. Fluctuating dumbbells are shown in every plaquette. There is no plaquette overlap at this doping.

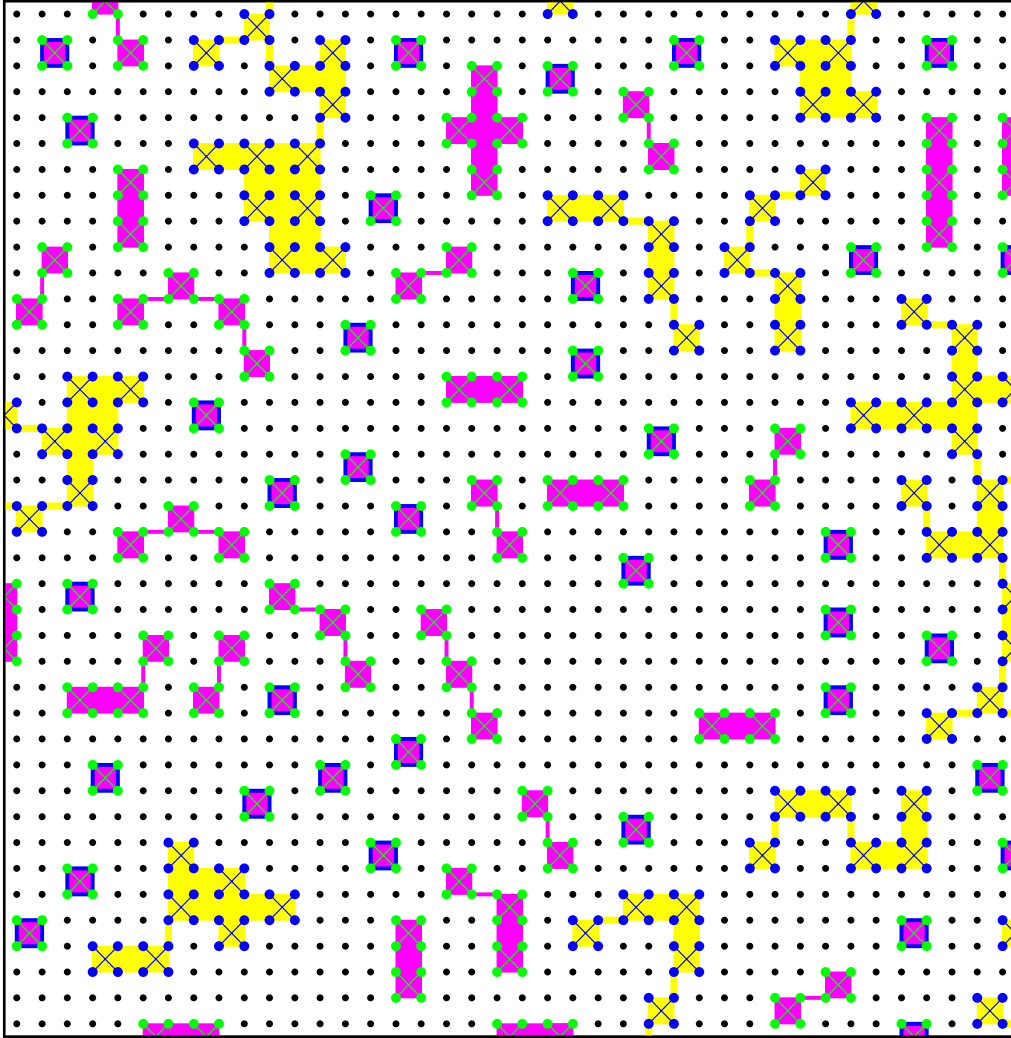


Figure S10 ($x = 0.10$): Plaquette doping of a 40×40 square CuO_2 lattice. Only the Cu sites are shown. The black dots are undoped AF Cu sites. The blue squares are isolated plaquettes (no neighboring plaquette). The yellow plaquette clusters are comprised of more than 4 plaquettes and contribute to the superconducting pairing because they are larger than the coherence length. The yellow overlay represents the metallic region comprised of planar Cu $d_{x^2-y^2}$ and planar O p_σ character. The magenta clusters are smaller than the Cooper pair coherence length and do not contribute to superconducting pairing. The magenta overlay represents metallic delocalization of the planar Cu $d_{x^2-y^2}$ and O p_σ orbitals. Fluctuating dumbbells are shown in every plaquette. There is no plaquette overlap at this doping.

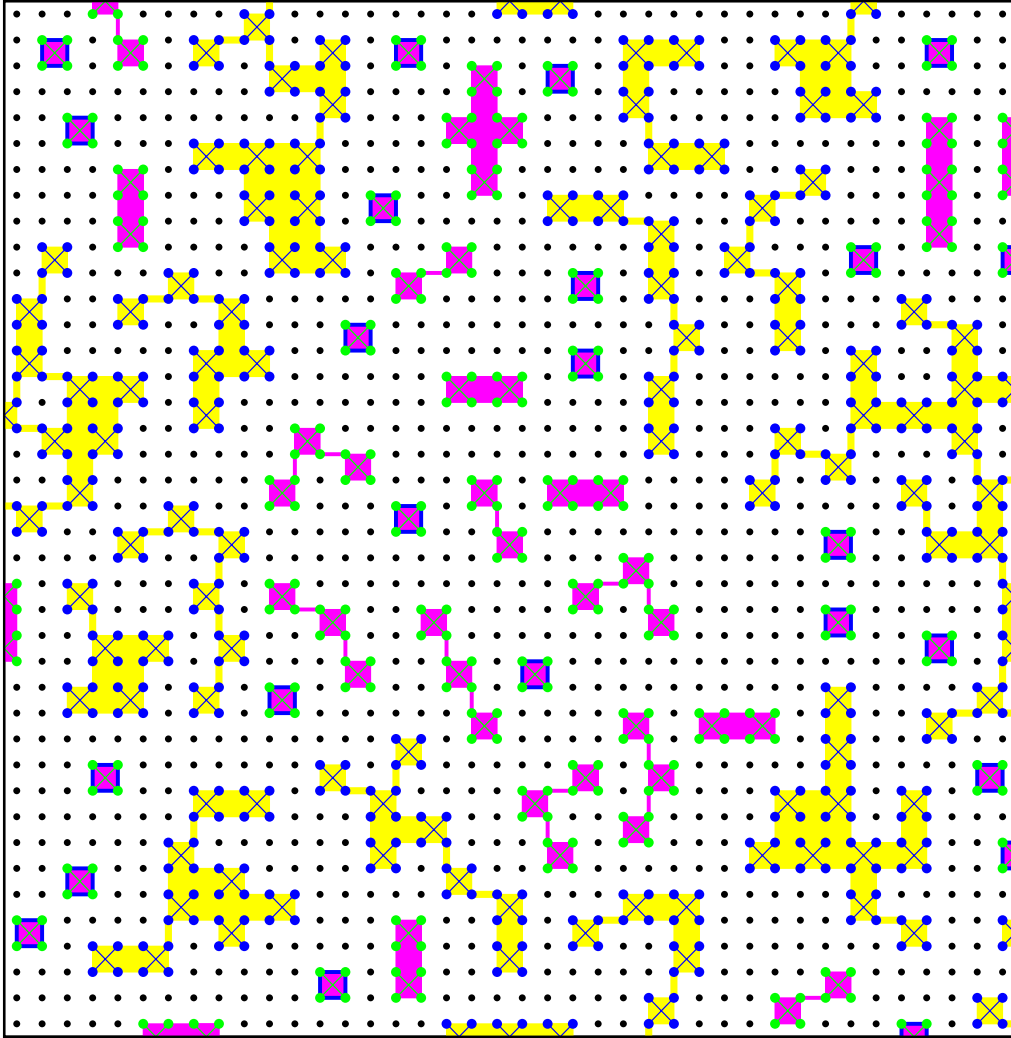


Figure S11 ($x = 0.11$): Plaquette doping of a 40×40 square CuO_2 lattice. Only the Cu sites are shown. The black dots are undoped AF Cu sites. The blue squares are isolated plaquettes (no neighboring plaquette). The yellow plaquette clusters are comprised of more than 4 plaquettes and contribute to the superconducting pairing because they are larger than the coherence length. The yellow overlay represents the metallic region comprised of planar Cu $d_{x^2-y^2}$ and planar O p_σ character. The magenta clusters are smaller than the Cooper pair coherence length and do not contribute to superconducting pairing. The magenta overlay represents metallic delocalization of the planar Cu $d_{x^2-y^2}$ and O p_σ orbitals. Fluctuating dumbbells are shown in every plaquette. There is no plaquette overlap at this doping.

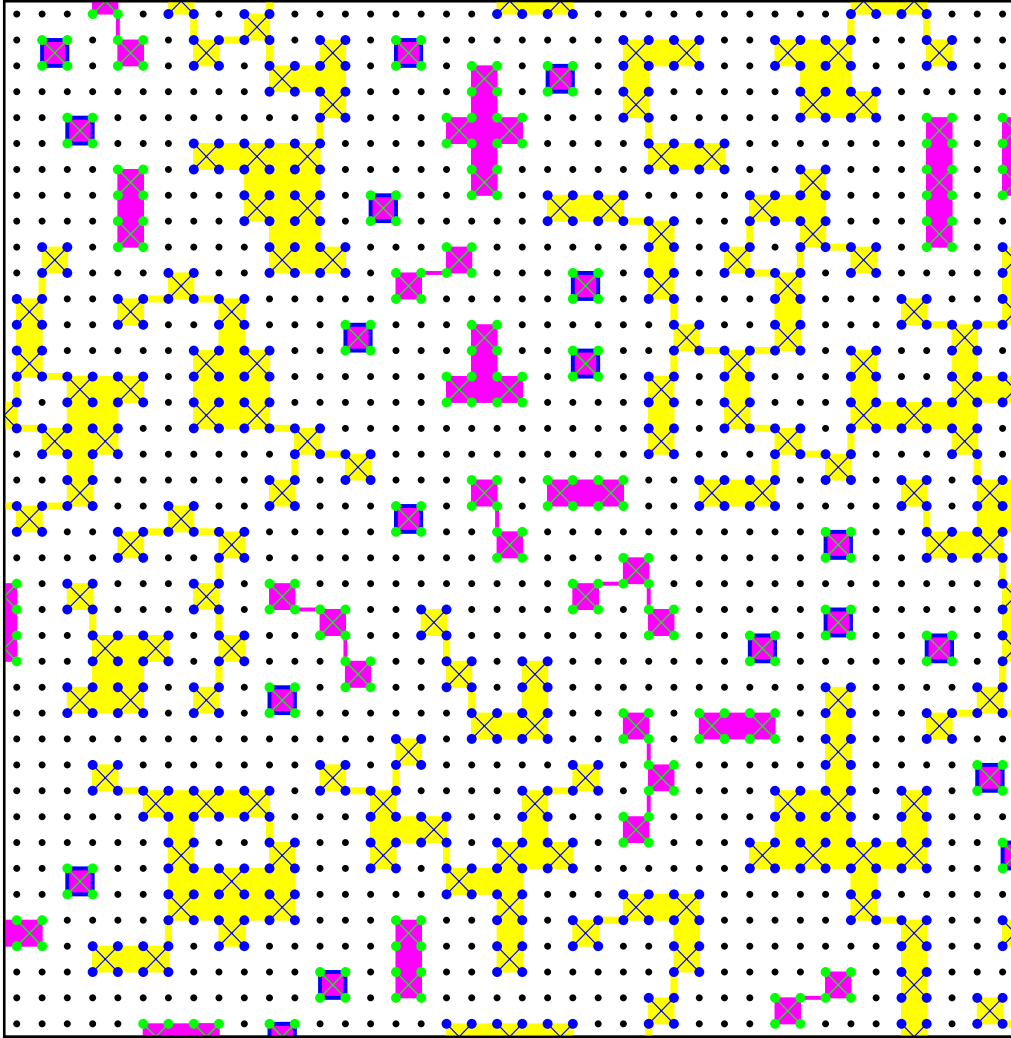


Figure S12 ($x = 0.12$): Plaquette doping of a 40×40 square CuO_2 lattice. Only the Cu sites are shown. The black dots are undoped AF Cu sites. The blue squares are isolated plaquettes (no neighboring plaquette). The yellow plaquette clusters are comprised of more than 4 plaquettes and contribute to the superconducting pairing because they are larger than the coherence length. The yellow overlay represents the metallic region comprised of planar Cu $d_{x^2-y^2}$ and planar O p_σ character. The magenta clusters are smaller than the Cooper pair coherence length and do not contribute to superconducting pairing. The magenta overlay represents metallic delocalization of the planar Cu $d_{x^2-y^2}$ and O p_σ orbitals. Fluctuating dumbbells are shown in every plaquette. There is no plaquette overlap at this doping.

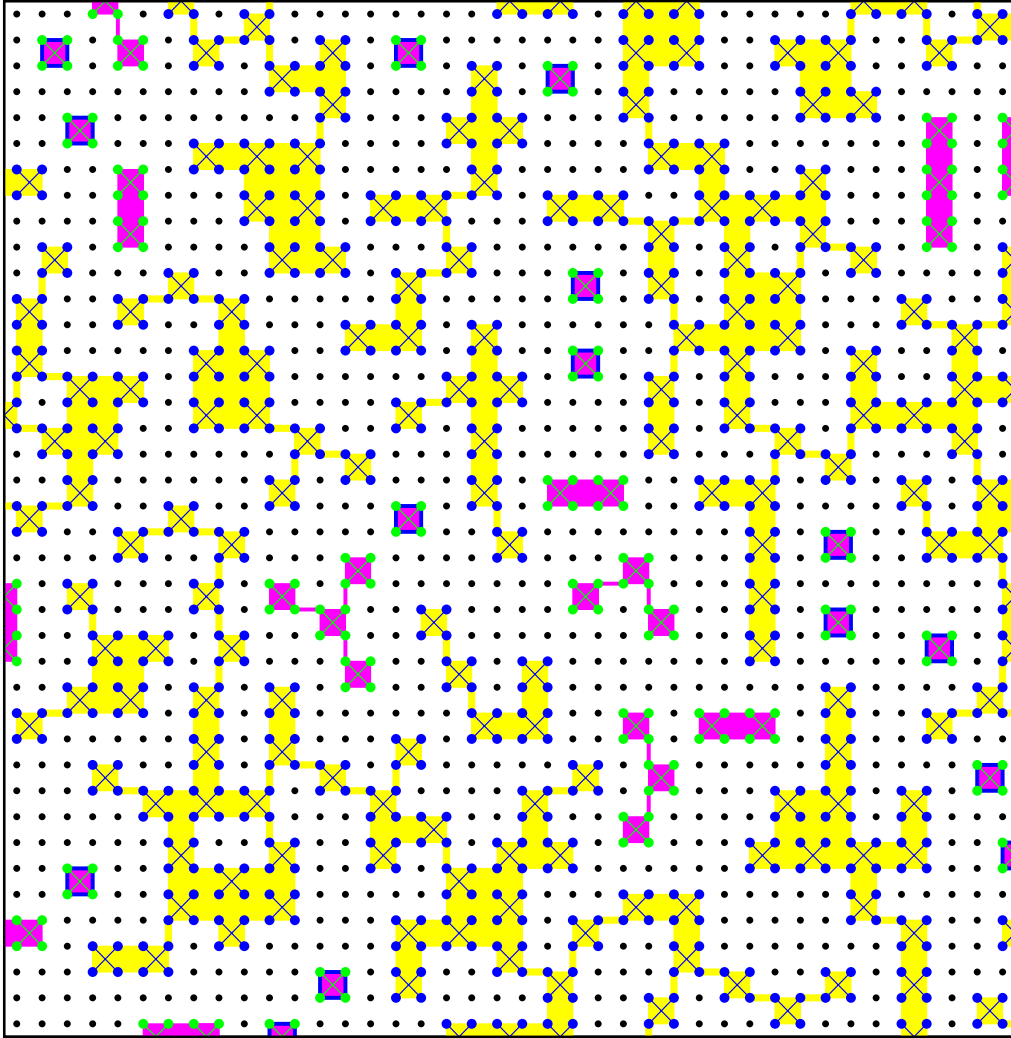


Figure S13 ($x = 0.13$): Plaquette doping of a 40×40 square CuO_2 lattice. Only the Cu sites are shown. The black dots are undoped AF Cu sites. The blue squares are isolated plaquettes (no neighboring plaquette). The yellow plaquette clusters are comprised of more than 4 plaquettes and contribute to the superconducting pairing because they are larger than the coherence length. The yellow overlay represents the metallic region comprised of planar Cu $d_{x^2-y^2}$ and planar O p_σ character. The magenta clusters are smaller than the Cooper pair coherence length and do not contribute to superconducting pairing. The magenta overlay represents metallic delocalization of the planar Cu $d_{x^2-y^2}$ and O p_σ orbitals. Fluctuating dumbbells are shown in every plaquette. There is no plaquette overlap at this doping.

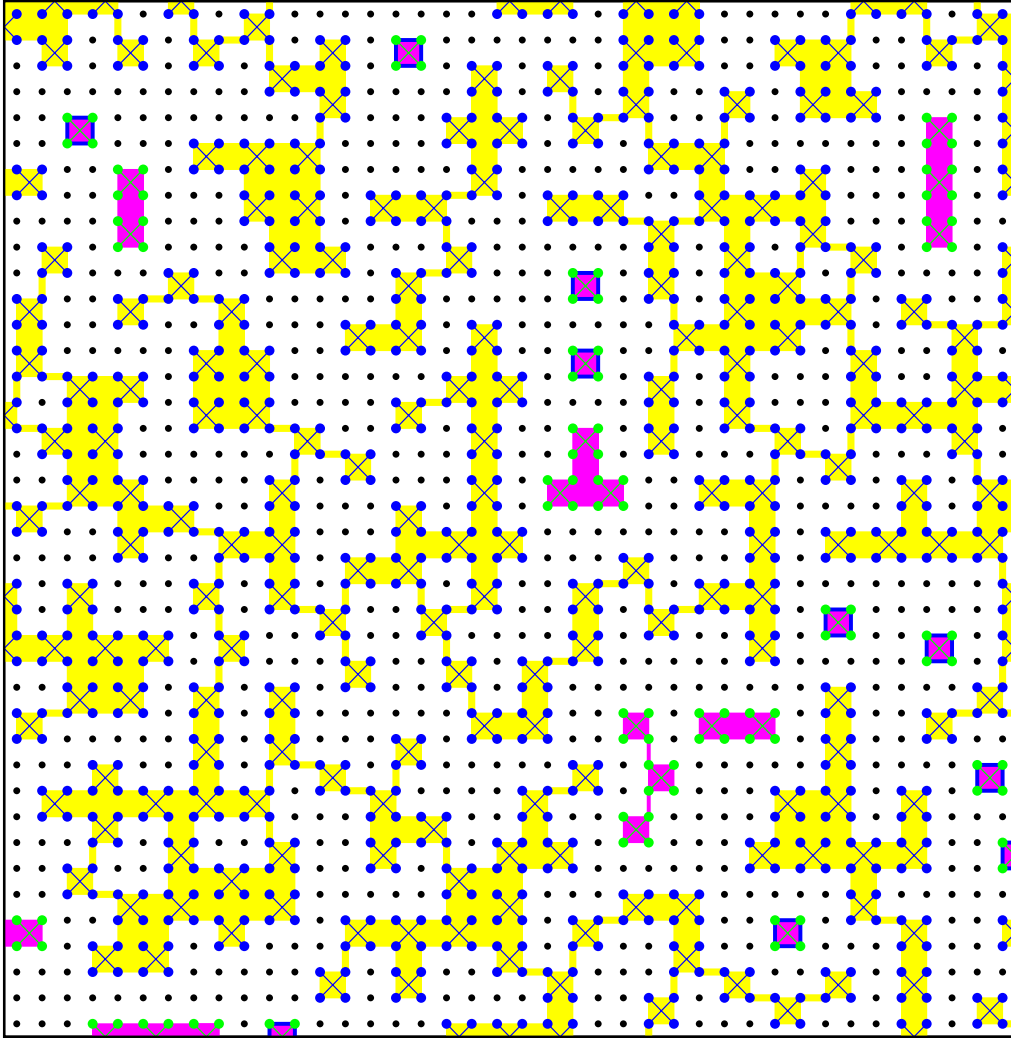


Figure S14 ($x = 0.14$): Plaquette doping of a 40×40 square CuO_2 lattice. Only the Cu sites are shown. The black dots are undoped AF Cu sites. The blue squares are isolated plaquettes (no neighboring plaquette). The yellow plaquette clusters are comprised of more than 4 plaquettes and contribute to the superconducting pairing because they are larger than the coherence length. The yellow overlay represents the metallic region comprised of planar Cu $d_{x^2-y^2}$ and planar O p_σ character. The magenta clusters are smaller than the Cooper pair coherence length and do not contribute to superconducting pairing. The magenta overlay represents metallic delocalization of the planar Cu $d_{x^2-y^2}$ and O p_σ orbitals. Fluctuating dumbbells are shown in every plaquette. There is no plaquette overlap at this doping.

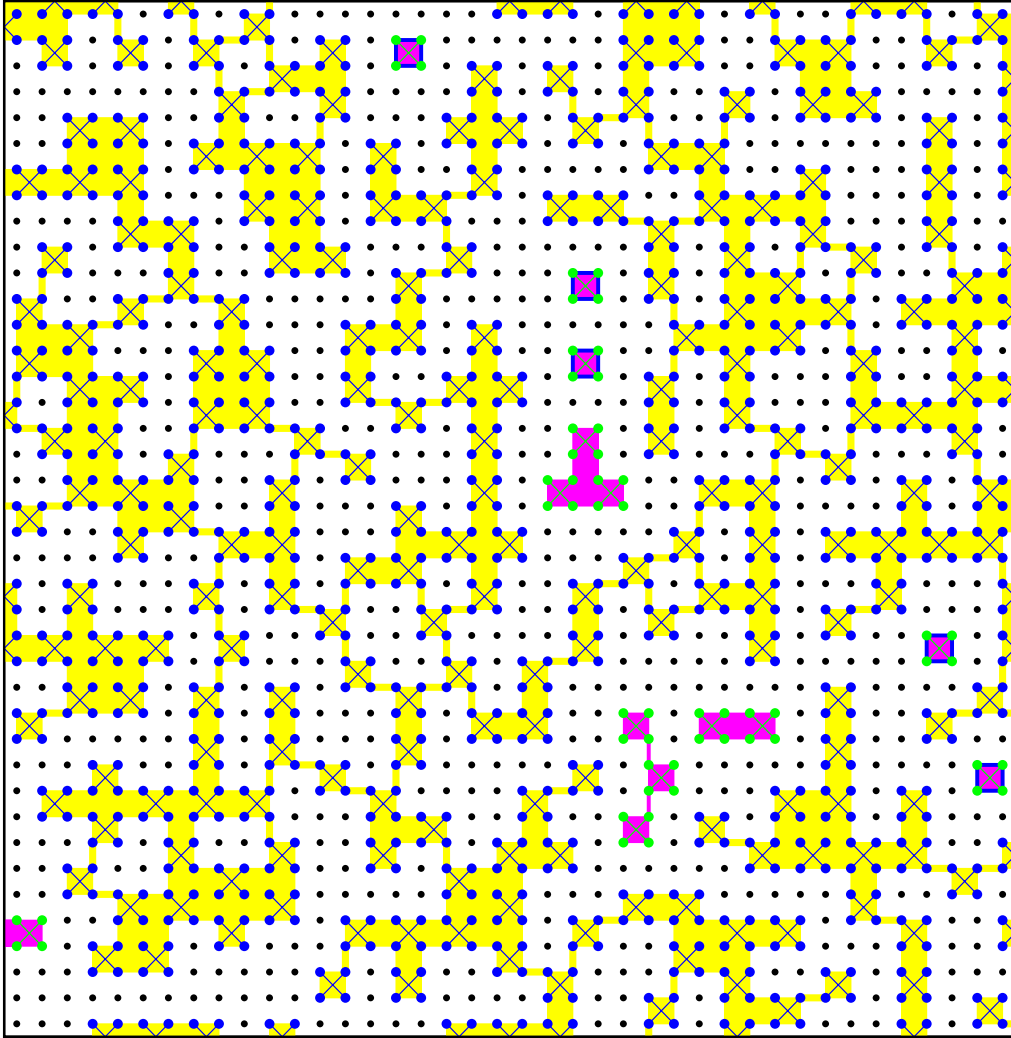


Figure S15 ($x = 0.15$): Plaquette doping of a 40×40 square CuO_2 lattice. Only the Cu sites are shown. The black dots are undoped AF Cu sites. The blue squares are isolated plaquettes (no neighboring plaquette). The yellow plaquette clusters are comprised of more than 4 plaquettes and contribute to the superconducting pairing because they are larger than the coherence length. The yellow overlay represents the metallic region comprised of planar Cu $d_{x^2-y^2}$ and planar O p_σ character. The magenta clusters are smaller than the Cooper pair coherence length and do not contribute to superconducting pairing. The magenta overlay represents metallic delocalization of the planar Cu $d_{x^2-y^2}$ and O p_σ orbitals. Fluctuating dumbbells are shown in every plaquette. There is no plaquette overlap at this doping. The 2D percolation threshold is approximately here.

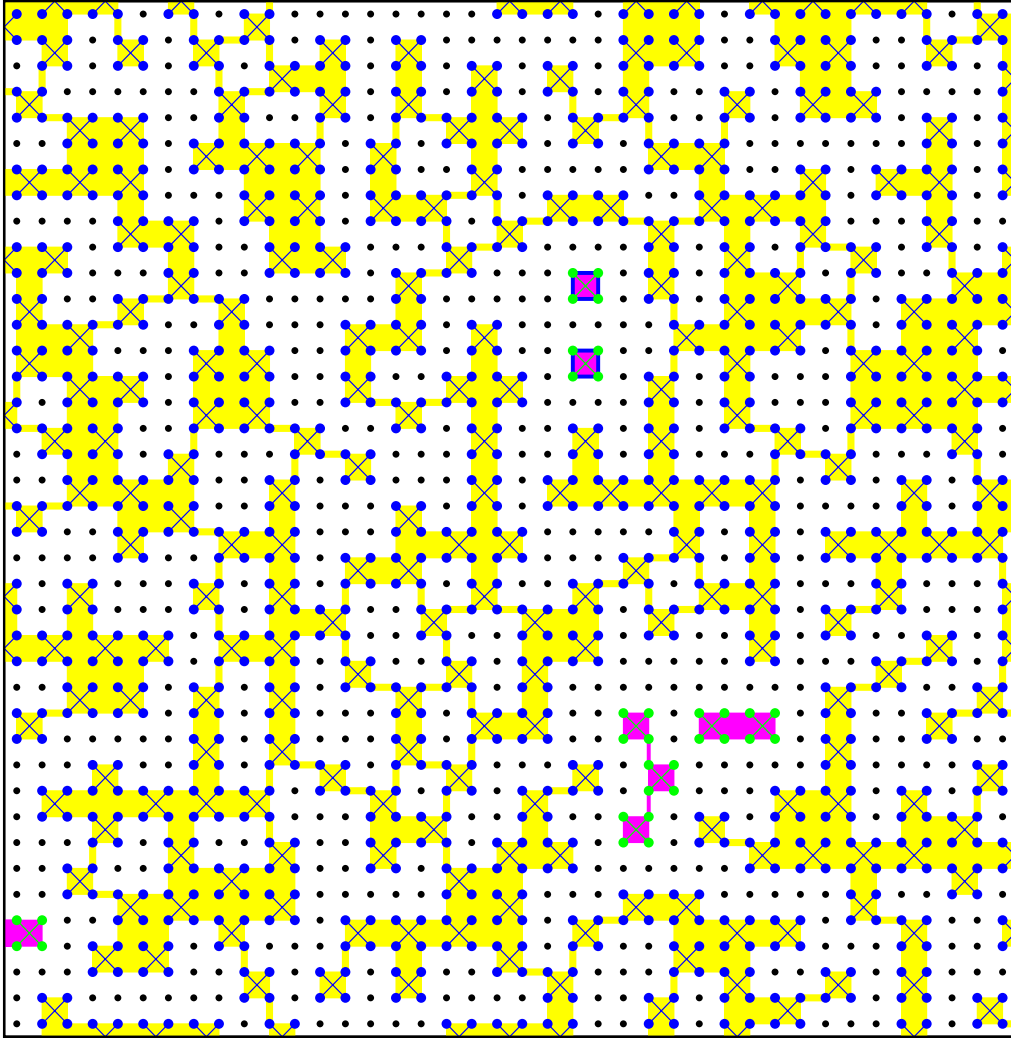


Figure S16 ($x = 0.16$): See the caption of Figure S15 for a definition of the symbols used here. 2D percolation occurs (see Figure 4), but the pathway is very tenuous. However, T_c is highest near this doping because the ratio of the surface metallic sites in the yellow region to total metallic sites (sum of yellow and magenta regions) is maximized.

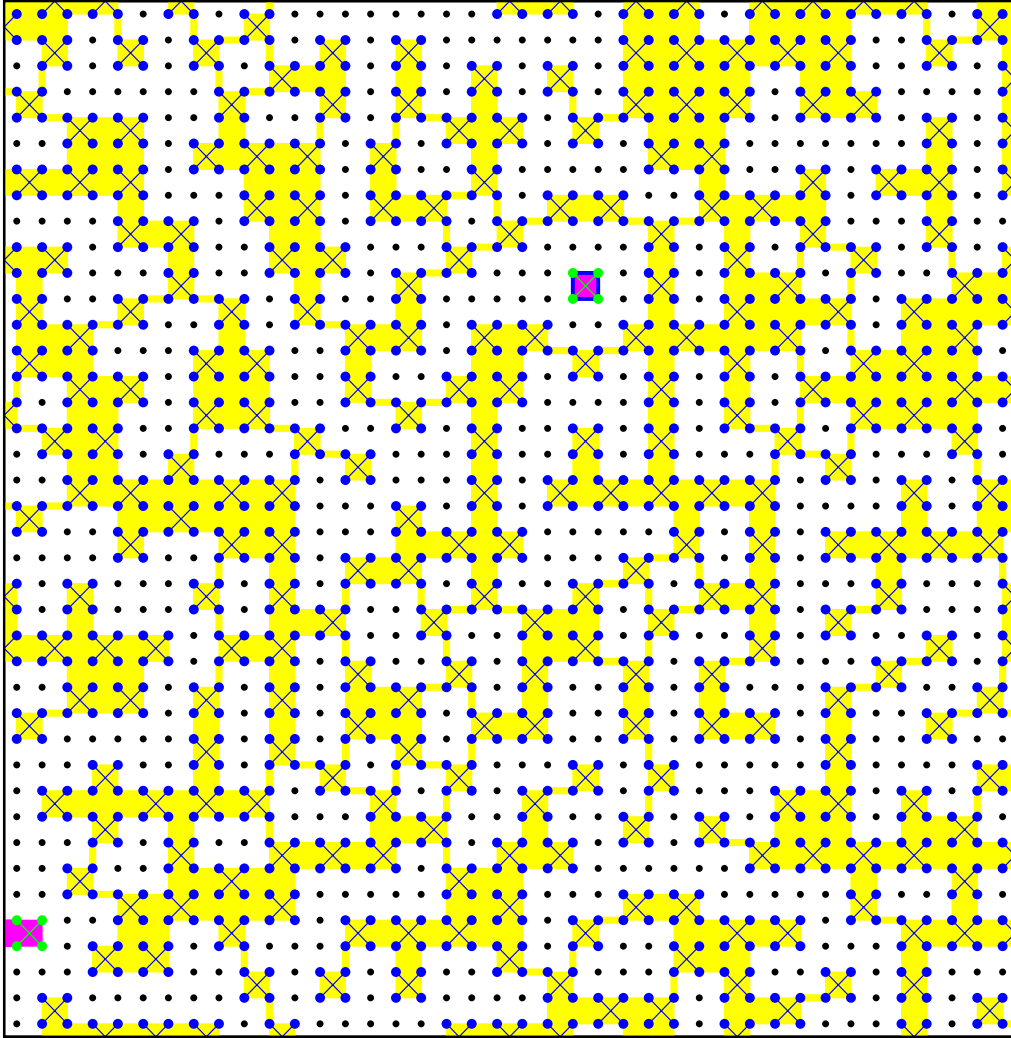


Figure S17 ($x = 0.17$): Plaquette doping of a 40×40 square CuO_2 lattice. Only the Cu sites are shown. The black dots are undoped AF Cu sites. The blue squares are isolated plaquettes (no neighboring plaquette). The yellow plaquette clusters are comprised of more than 4 plaquettes and contribute to the superconducting pairing because they are larger than the coherence length. The yellow overlay represents the metallic region comprised of planar Cu $d_{x^2-y^2}$ and planar O p_σ character. The magenta clusters are smaller than the Cooper pair coherence length and do not contribute to superconducting pairing. The magenta overlay represents metallic delocalization of the planar Cu $d_{x^2-y^2}$ and O p_σ orbitals. Fluctuating dumbbells are shown in every plaquette. There is no plaquette overlap at this doping. 2D percolation occurs here, but the pathway is very tenuous.

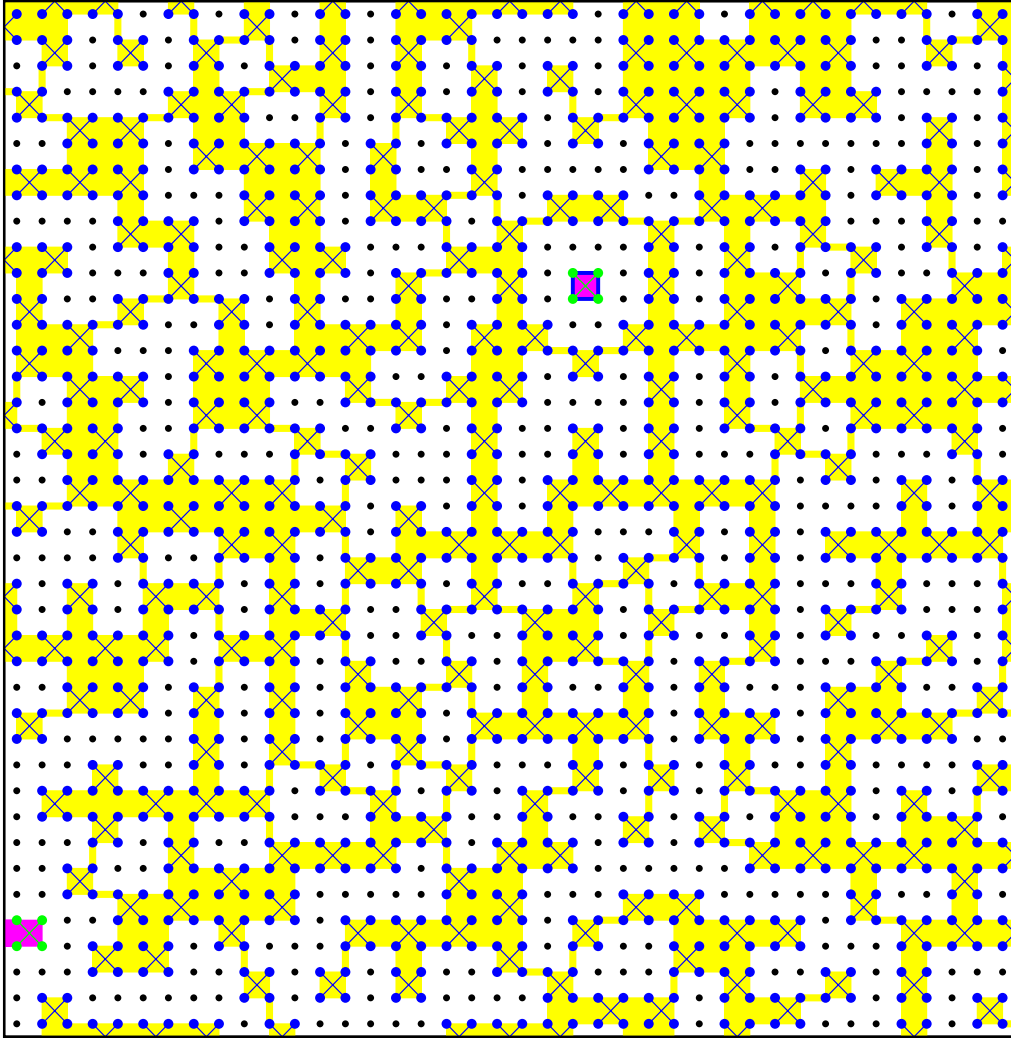


Figure S18 ($x = 0.18$): Plaquette doping of a 40×40 square CuO_2 lattice. Only the Cu sites are shown. The black dots are undoped AF Cu sites. The blue squares are isolated plaquettes (no neighboring plaquette). The yellow plaquette clusters are comprised of more than 4 plaquettes and contribute to the superconducting pairing because they are larger than the coherence length. The yellow overlay represents the metallic region comprised of planar Cu $d_{x^2-y^2}$ and planar O p_σ character. The magenta clusters are smaller than the Cooper pair coherence length and do not contribute to superconducting pairing. The magenta overlay represents metallic delocalization of the planar Cu $d_{x^2-y^2}$ and O p_σ orbitals. Fluctuating dumbbells are shown in every plaquette. There is no plaquette overlap at this doping. 2D percolation occurs here, but the pathway is very tenuous.

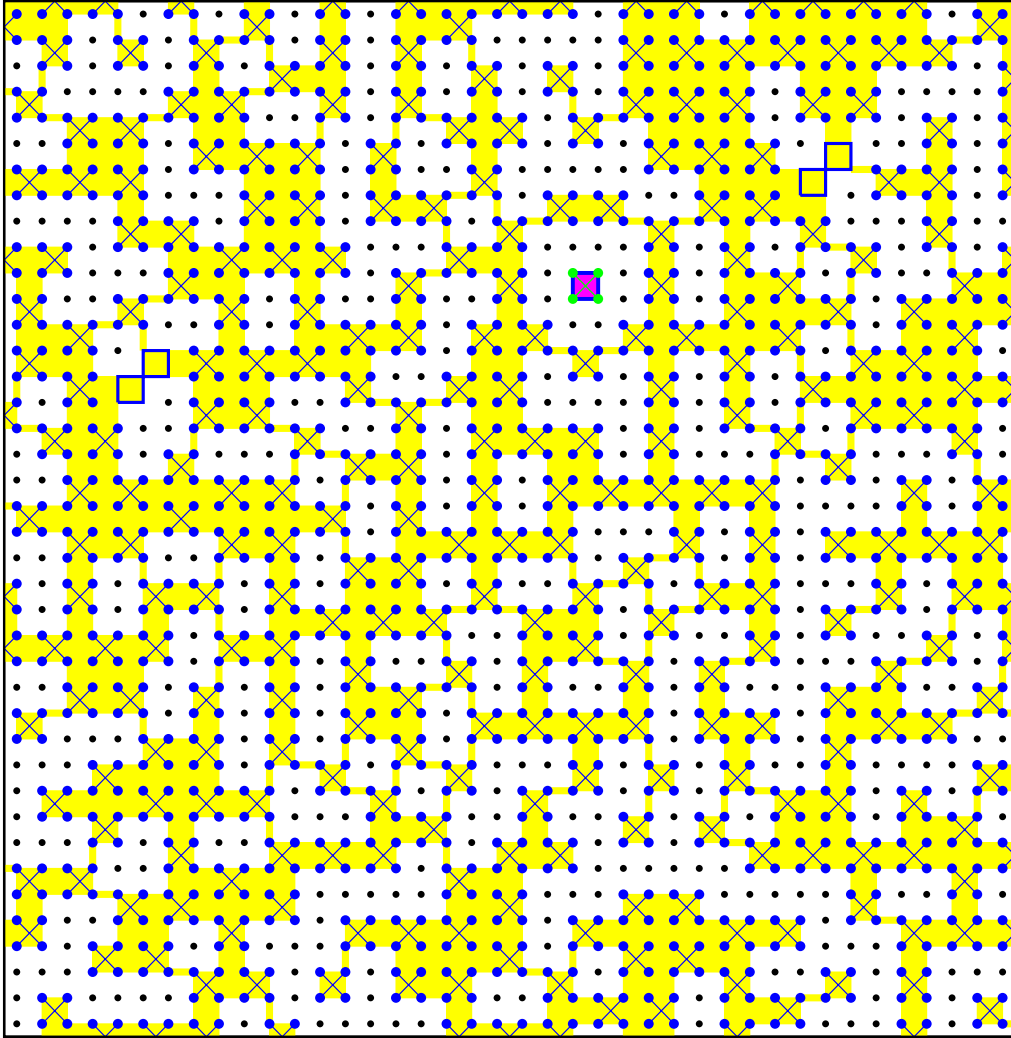


Figure S19 ($x = 0.19$): Plaquette doping of a 40×40 square CuO_2 lattice. Only the Cu sites are shown. The black dots are undoped AF Cu sites. One isolated plaquette (no neighboring plaquette) remains. The yellow plaquette clusters are comprised of more than 4 plaquettes and contribute to the superconducting pairing because they are larger than the coherence length. The yellow overlay represents the metallic region comprised of planar Cu $d_{x^2-y^2}$ and planar O p_σ character. The magenta clusters are smaller than the Cooper pair coherence length and do not contribute to superconducting pairing. The magenta overlay represents metallic delocalization of the planar Cu $d_{x^2-y^2}$ and O p_σ orbitals. Fluctuating dumbbells are inside non-overlapping plaquettes. Plaquette overlap begins (blue squares). In order to minimize their repulsion, the overlap occurs at the plaquette corners.

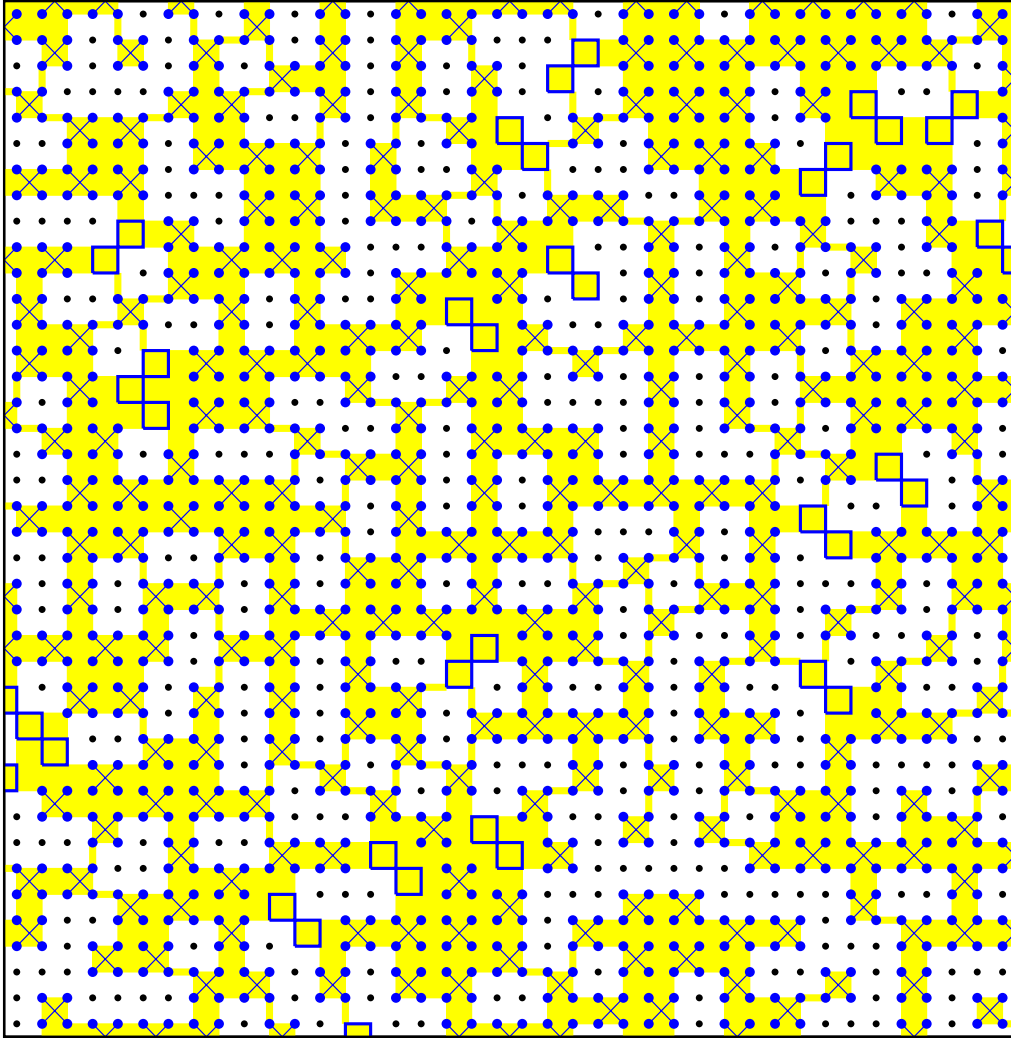


Figure S20 ($x = 0.20$): Plaquette doping of a 40×40 square CuO_2 lattice. Only the Cu sites are shown. The black dots are undoped AF Cu sites. The yellow plaquette clusters are comprised of more than 4 plaquettes and contribute to the superconducting pairing because they are larger than the coherence length. The yellow overlay represents the metallic region comprised of planar Cu $d_{x^2-y^2}$ and planar O p_σ character. Fluctuating dumbbells are inside non-overlapping plaquettes. Plaquette overlap is shown by blue squares. In order to minimize their repulsion, the overlap occurs at the plaquette corners only. There are no isolated plaquettes remaining in this lattice. The number of isolated plaquettes in the crystal is of measure zero. The pseudogap (arising from the isolated plaquettes) has vanished.¹¹

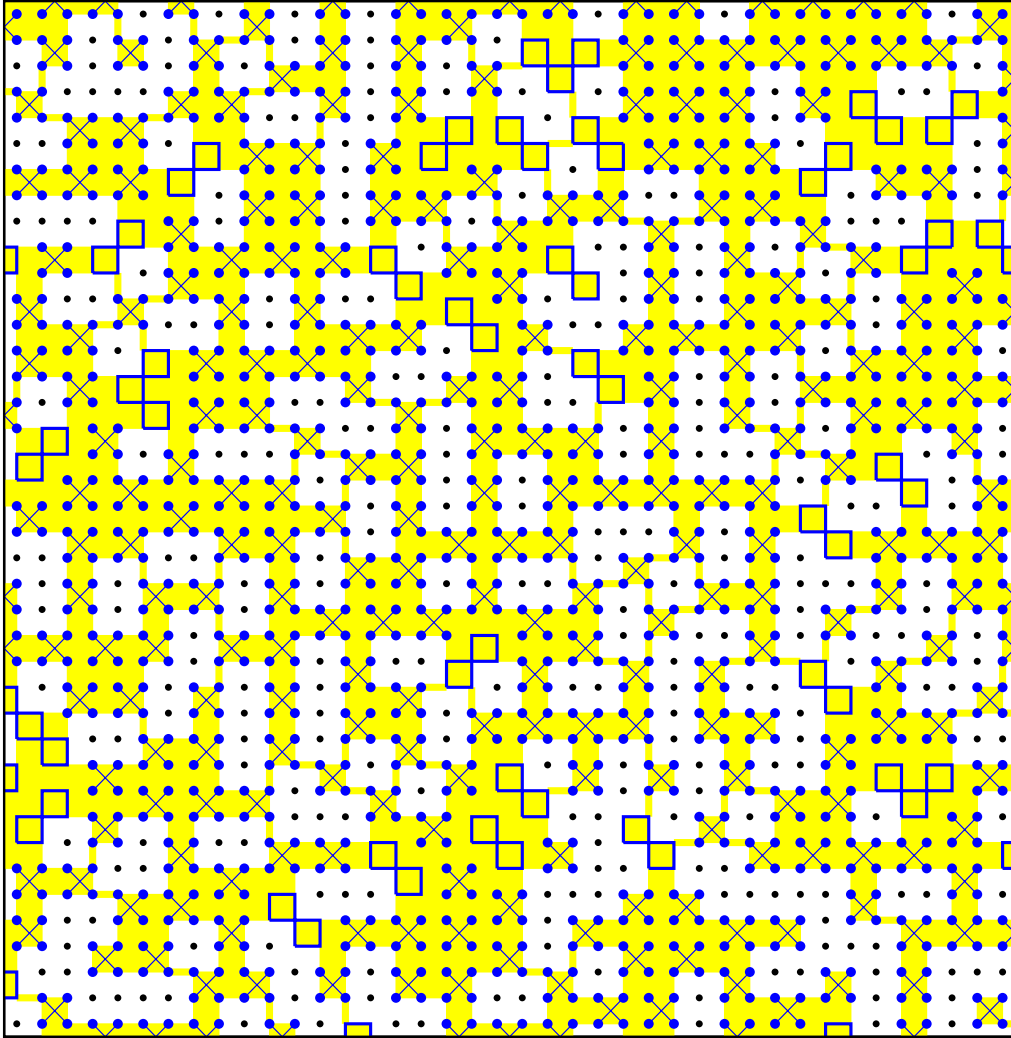


Figure S21 ($x = 0.21$): Plaquette doping of a 40×40 square CuO_2 lattice. Only the Cu sites are shown. The black dots are undoped AF Cu sites. The yellow plaquette clusters are comprised of more than 4 plaquettes and contribute to the superconducting pairing because they are larger than the coherence length. The yellow overlay represents the metallic region comprised of planar Cu $d_{x^2-y^2}$ and planar O p_σ character. Fluctuating dumbbells are inside non-overlapping plaquettes. Plaquette overlap is shown by blue squares. In order to minimize their repulsion, the overlap occurs at the plaquette corners only. There are no isolated plaquettes remaining in this lattice. The number of isolated plaquettes in the crystal is of measure zero.

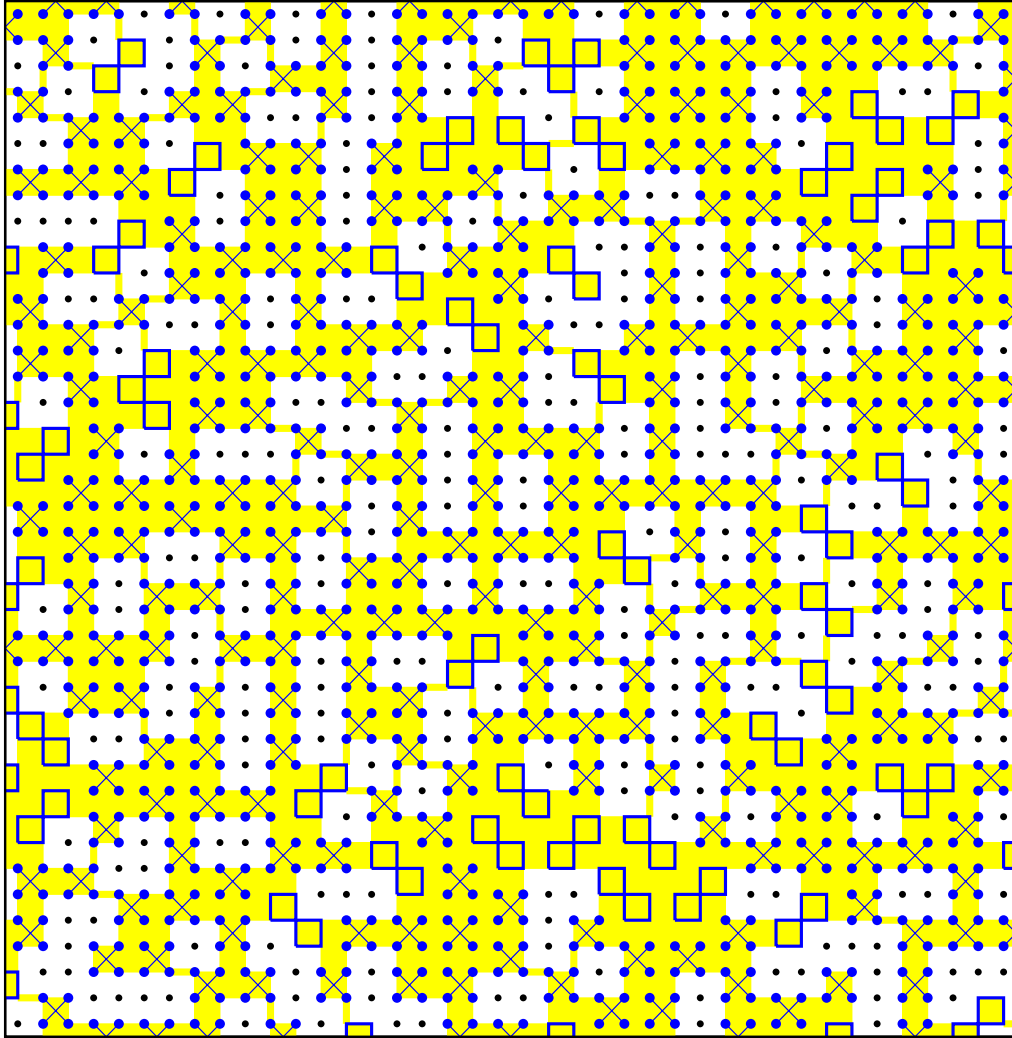


Figure S22 ($x = 0.22$): Plaquette doping of a 40×40 square CuO_2 lattice. Only the Cu sites are shown. The black dots are undoped AF Cu sites. The yellow plaquette clusters are comprised of more than 4 plaquettes and contribute to the superconducting pairing because they are larger than the coherence length. The yellow overlay represents the metallic region comprised of planar Cu $d_{x^2-y^2}$ and planar O p_σ character. Fluctuating dumbbells are inside non-overlapping plaquettes. Plaquette overlap is shown by blue squares. In order to minimize their repulsion, the overlap occurs at the plaquette corners only. There are no isolated plaquettes remaining in this lattice. The number of isolated plaquettes in the crystal is of measure zero.

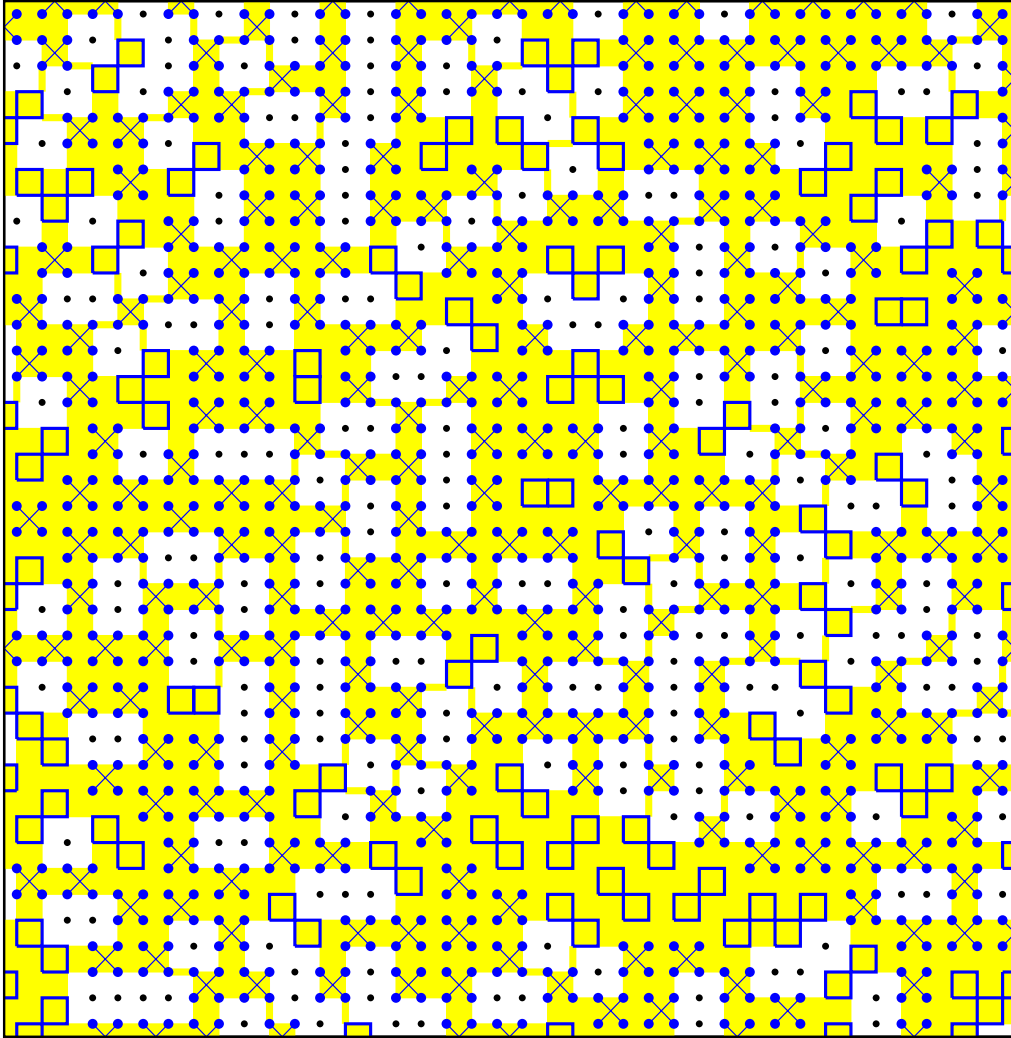


Figure S23 ($x = 0.23$): Plaquette doping of a 40×40 square CuO_2 lattice. Only the Cu sites are shown. The black dots are undoped AF Cu sites. The yellow plaquette clusters are comprised of more than 4 plaquettes and contribute to the superconducting pairing because they are larger than the coherence length. The yellow overlay represents the metallic region comprised of planar Cu $d_{x^2-y^2}$ and planar O p_σ character. Fluctuating dumbbells are inside non-overlapping plaquettes. Plaquette overlap is shown by blue squares. Corner overlap of plaquettes is no longer possible. Added plaquettes overlap existing plaquettes by sharing edges or overlapping two plaquettes at their corners. We believe the additional energy needed to overlap plaquette edges or two corners is the reason why $\text{YBa}_2\text{Cu}_3\text{O}_{7-\delta}$ cannot be doped beyond this point.

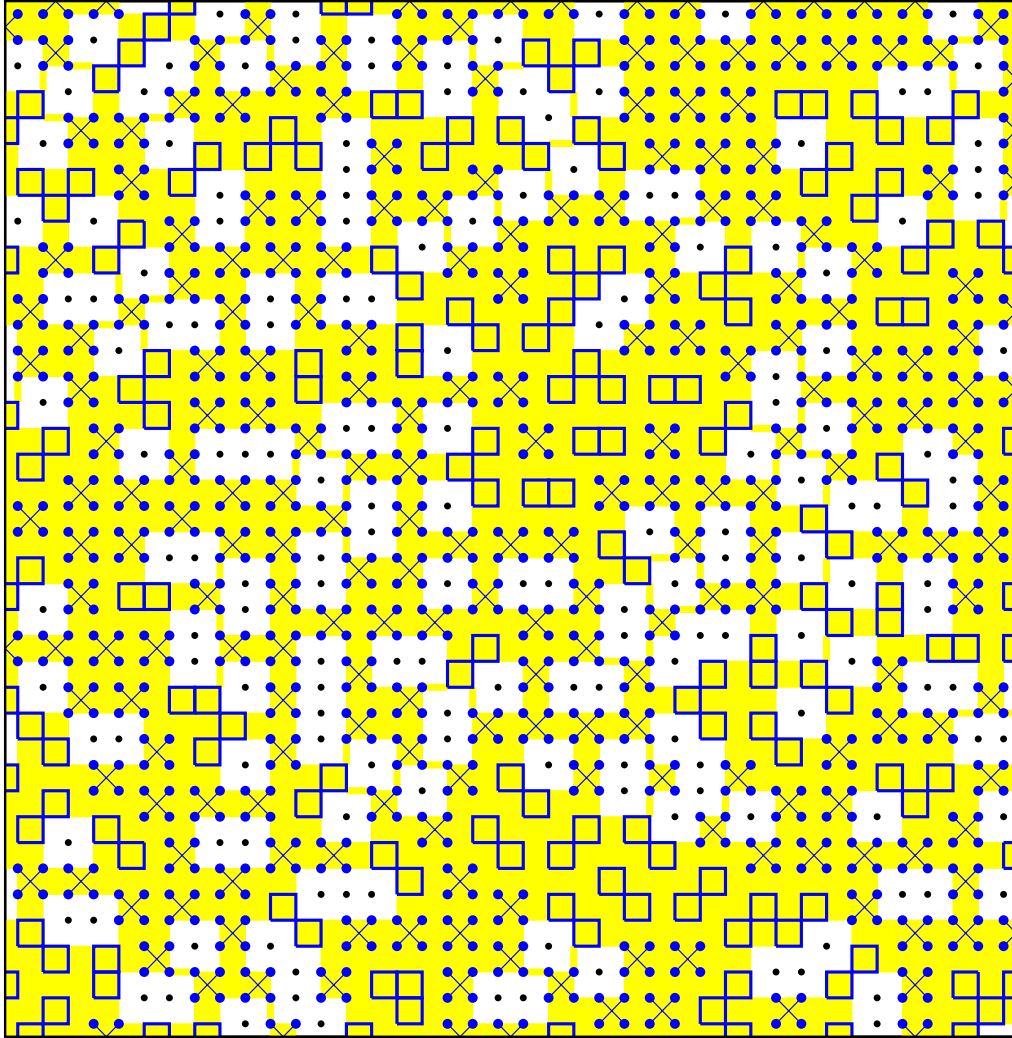


Figure S24 ($x = 0.24$): Plaquette doping of a 40×40 square CuO_2 lattice. Only the Cu sites are shown. The black dots are undoped AF Cu sites. The yellow plaquette clusters are comprised of more than 4 plaquettes and contribute to the superconducting pairing because they are larger than the coherence length. The yellow overlay represents the metallic region comprised of planar Cu $d_{x^2-y^2}$ and planar O p_σ character. Fluctuating dumbbells are inside non-overlapping plaquettes. Plaquette overlap is shown by blue squares. Corner overlap of plaquettes is no longer possible. Added plaquettes overlap existing plaquettes by sharing edges or overlapping two plaquettes at their corners.

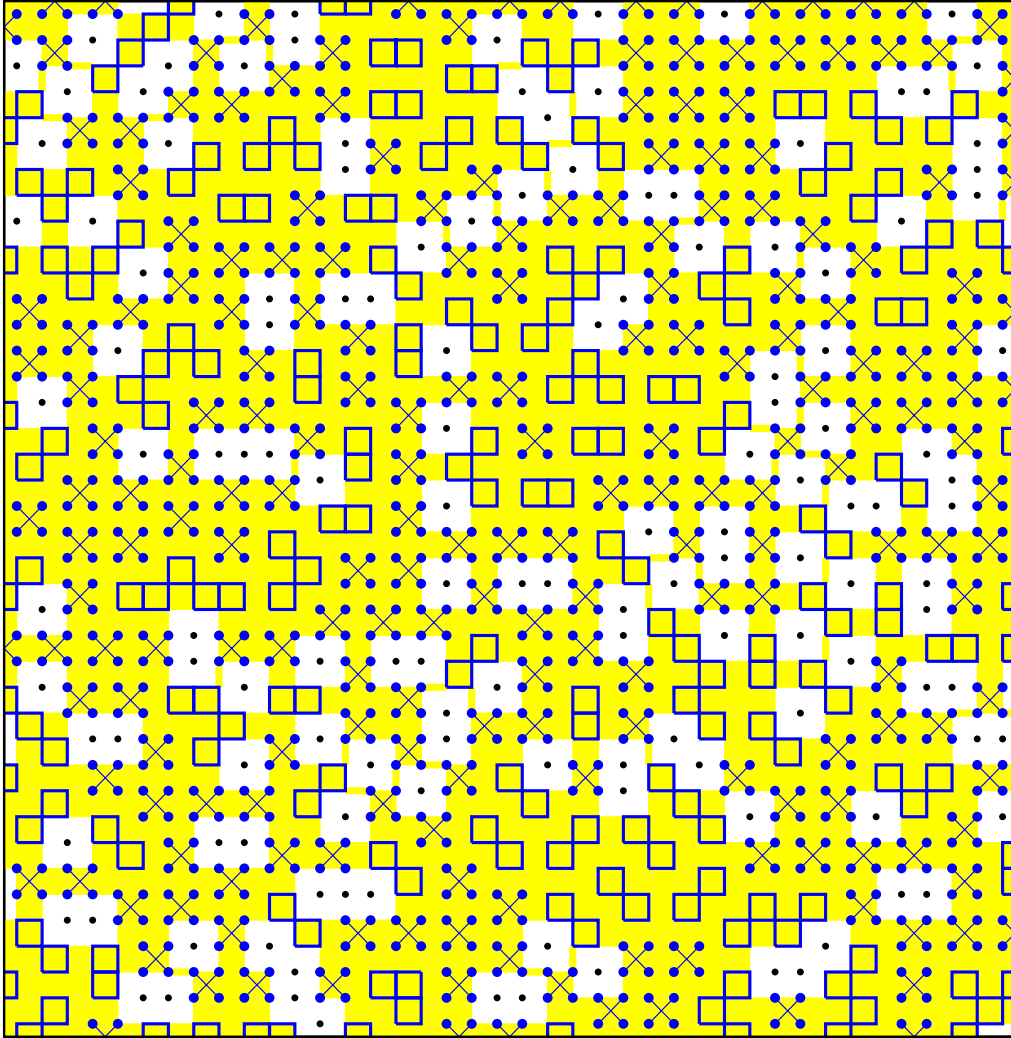


Figure S25 ($x = 0.25$): Plaquette doping of a 40×40 square CuO_2 lattice. Only the Cu sites are shown. The black dots are undoped AF Cu sites. The yellow plaquette clusters are comprised of more than 4 plaquettes and contribute to the superconducting pairing because they are larger than the coherence length. The yellow overlay represents the metallic region comprised of planar Cu $d_{x^2-y^2}$ and planar O p_σ character. Fluctuating dumbbells are inside non-overlapping plaquettes. Plaquette overlap is shown by blue squares. Corner overlap of plaquettes is no longer possible. Added plaquettes overlap existing plaquettes by sharing edges or overlapping two plaquettes at their corners.

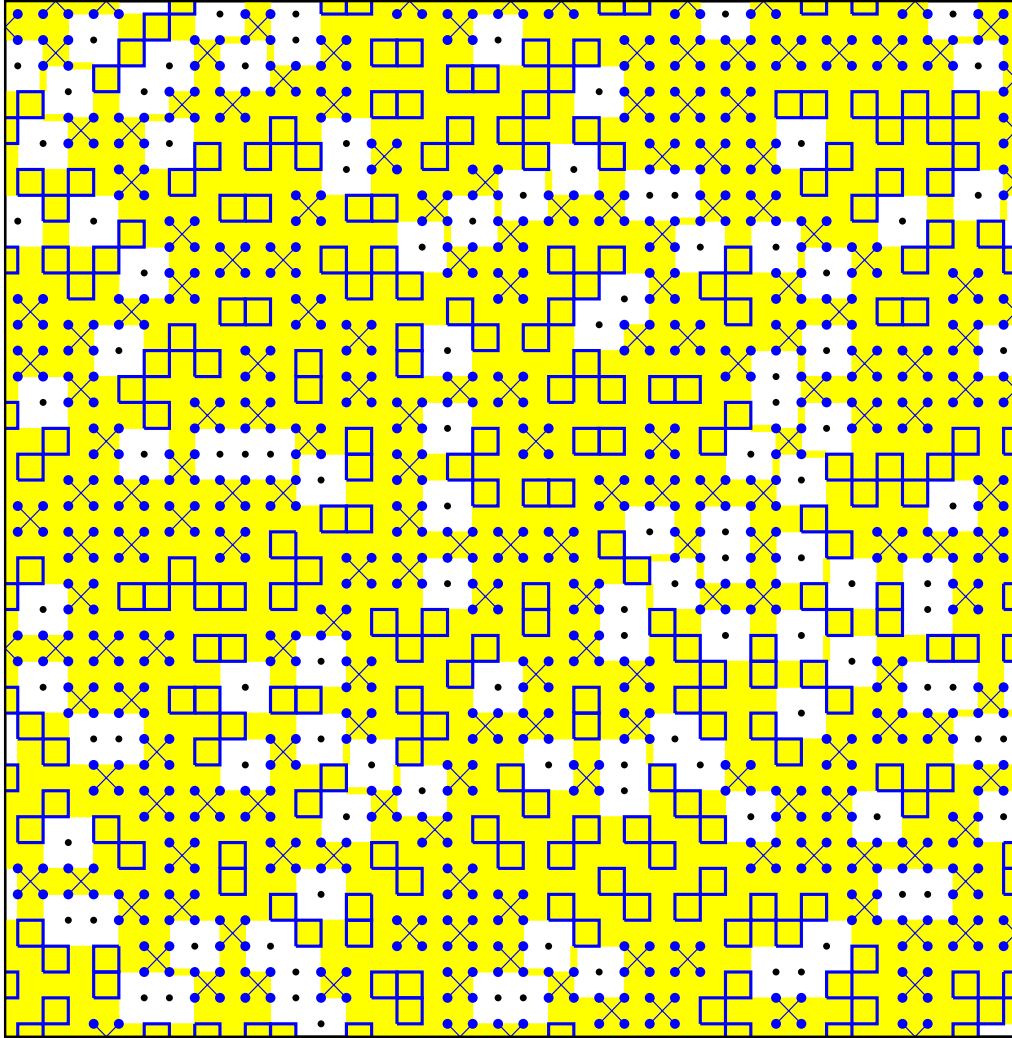


Figure S26 ($x = 0.26$): Plaquette doping of a 40×40 square CuO_2 lattice. Only the Cu sites are shown. The black dots are undoped AF Cu sites. The yellow plaquette clusters are comprised of more than 4 plaquettes and contribute to the superconducting pairing because they are larger than the coherence length. The yellow overlay represents the metallic region comprised of planar Cu $d_{x^2-y^2}$ and planar O p_σ character. Fluctuating dumbbells are inside non-overlapping plaquettes. Plaquette overlap is shown by blue squares. Corner overlap of plaquettes is no longer possible. Added plaquettes overlap existing plaquettes by sharing edges or overlapping two plaquettes at their corners.

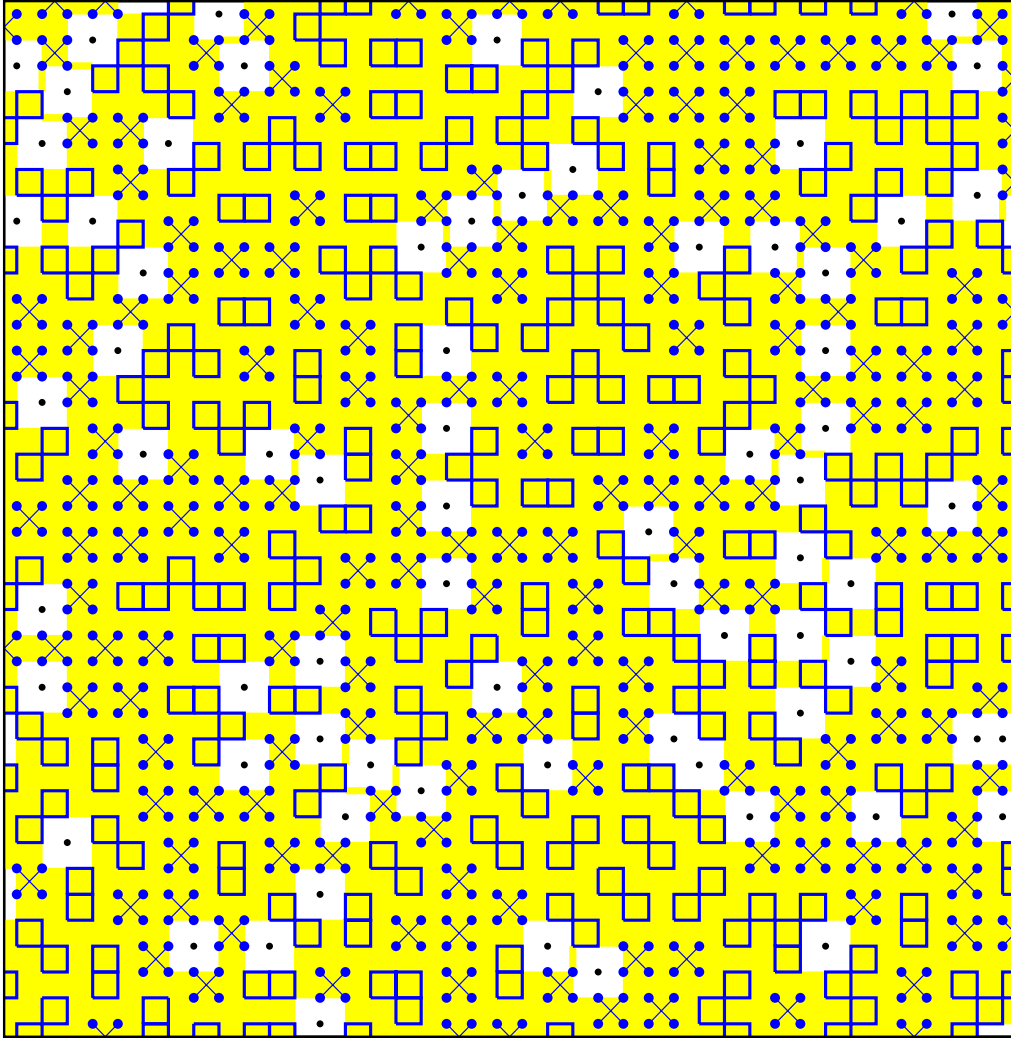


Figure S27 ($x = 0.27$): Plaquette doping of a 40×40 square CuO_2 lattice. Only the Cu sites are shown. The black dots are undoped AF Cu sites. The yellow plaquette clusters are comprised of more than 4 plaquettes and contribute to the superconducting pairing because they are larger than the coherence length. The yellow overlay represents the metallic region comprised of planar Cu $d_{x^2-y^2}$ and planar O p_σ character. Fluctuating dumbbells are inside non-overlapping plaquettes. Plaquette overlap is shown by blue squares. Corner overlap of plaquettes is no longer possible. Added plaquettes overlap existing plaquettes by sharing edges or overlapping two plaquettes at their corners.

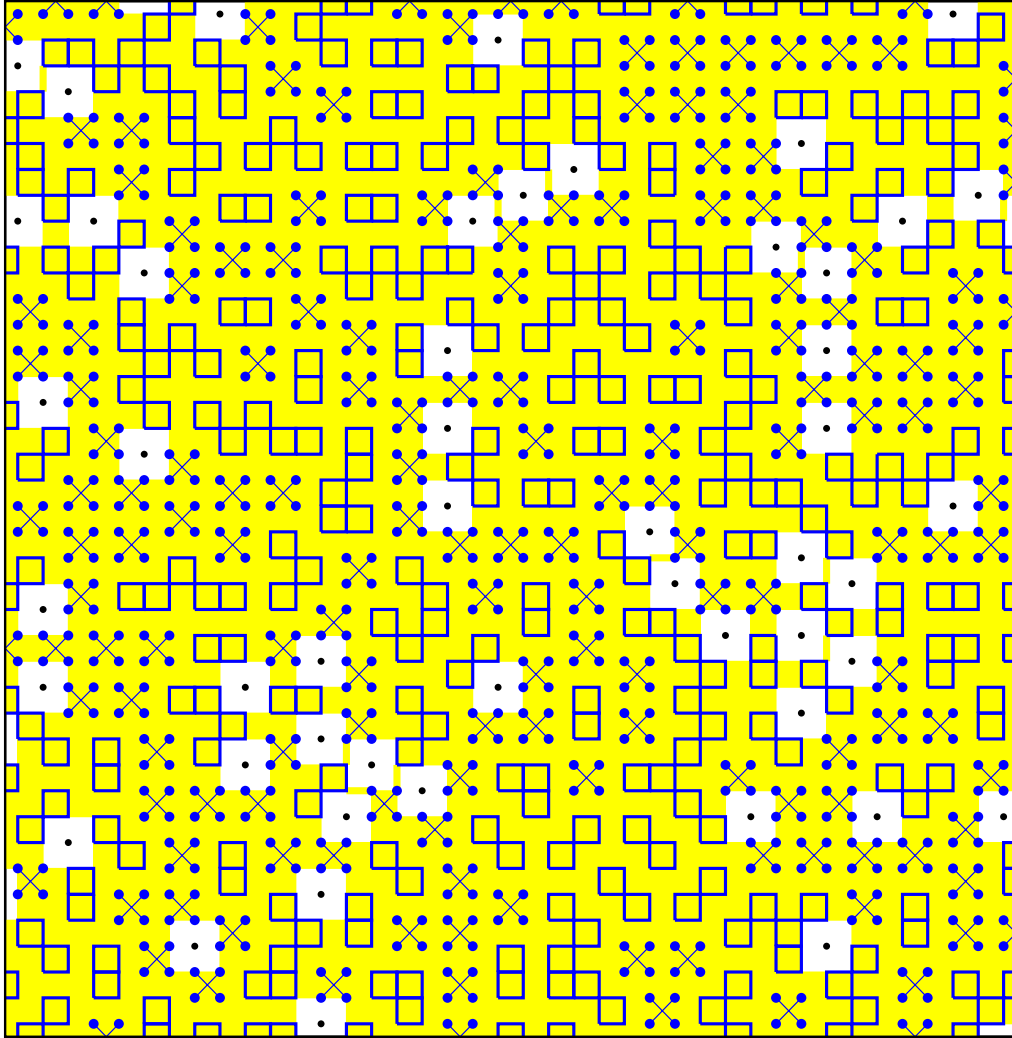


Figure S28 ($x = 0.28$): Plaquette doping of a 40×40 square CuO_2 lattice. Only the Cu sites are shown. The black dots are undoped AF Cu sites. The yellow plaquette clusters are comprised of more than 4 plaquettes and contribute to the superconducting pairing because they are larger than the coherence length. The yellow overlay represents the metallic region comprised of planar Cu $d_{x^2-y^2}$ and planar O p_σ character. Fluctuating dumbbells are inside non-overlapping plaquettes. Plaquette overlap is shown by blue squares. Edge overlap of plaquettes is no longer possible. Added plaquettes overlap existing plaquettes at three metallic sites. Only isolated localized spins remain (there are no adjacent black dots).

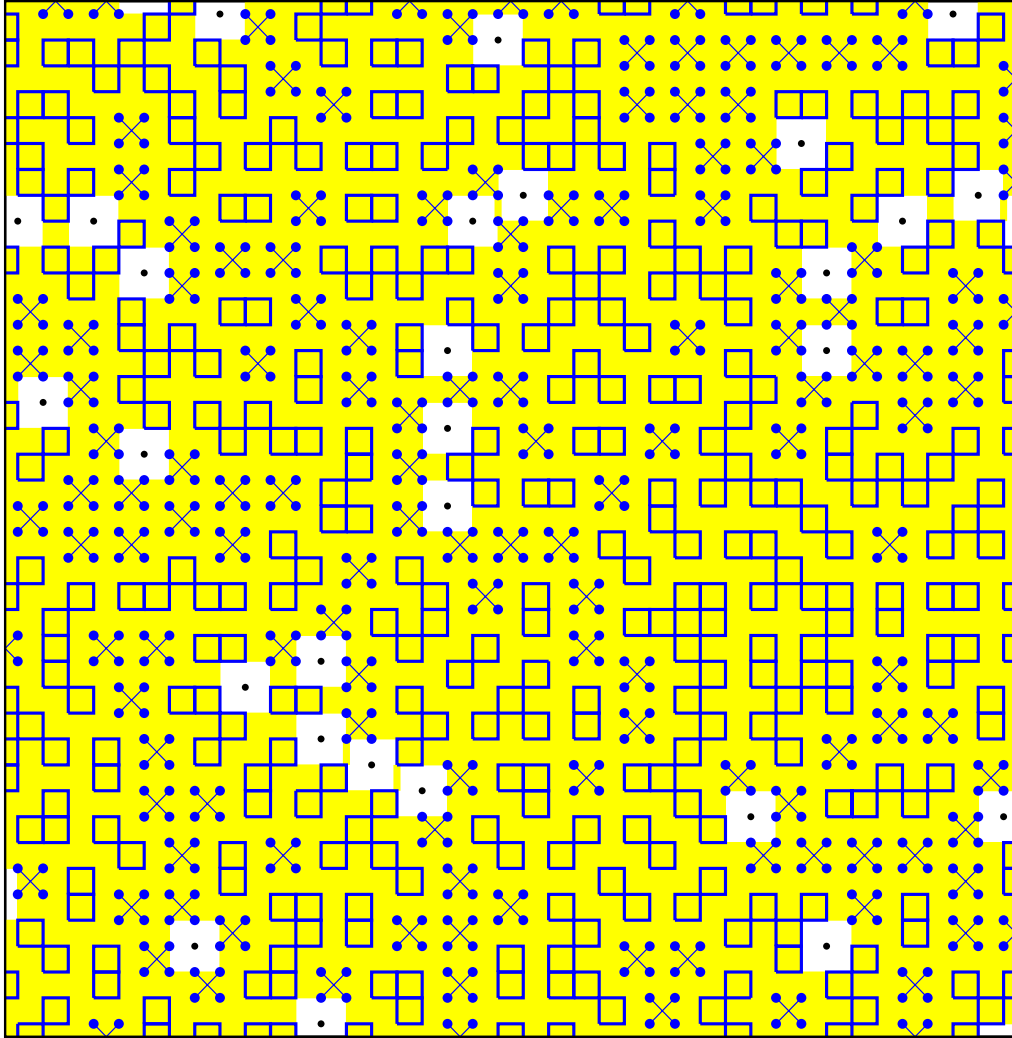


Figure S29 ($x = 0.29$): Plaquette doping of a 40×40 square CuO_2 lattice. Only the Cu sites are shown. The black dots are undoped AF Cu sites. The yellow plaquette clusters are comprised of more than 4 plaquettes and contribute to the superconducting pairing because they are larger than the coherence length. The yellow overlay represents the metallic region comprised of planar Cu $d_{x^2-y^2}$ and planar O p_σ character. Fluctuating dumbbells are inside non-overlapping plaquettes. Plaquette overlap is shown by blue squares. Edge overlap of plaquettes is no longer possible. Added plaquettes overlap existing plaquettes at three metallic sites. Only isolated localized spins remain (there are no adjacent black dots).

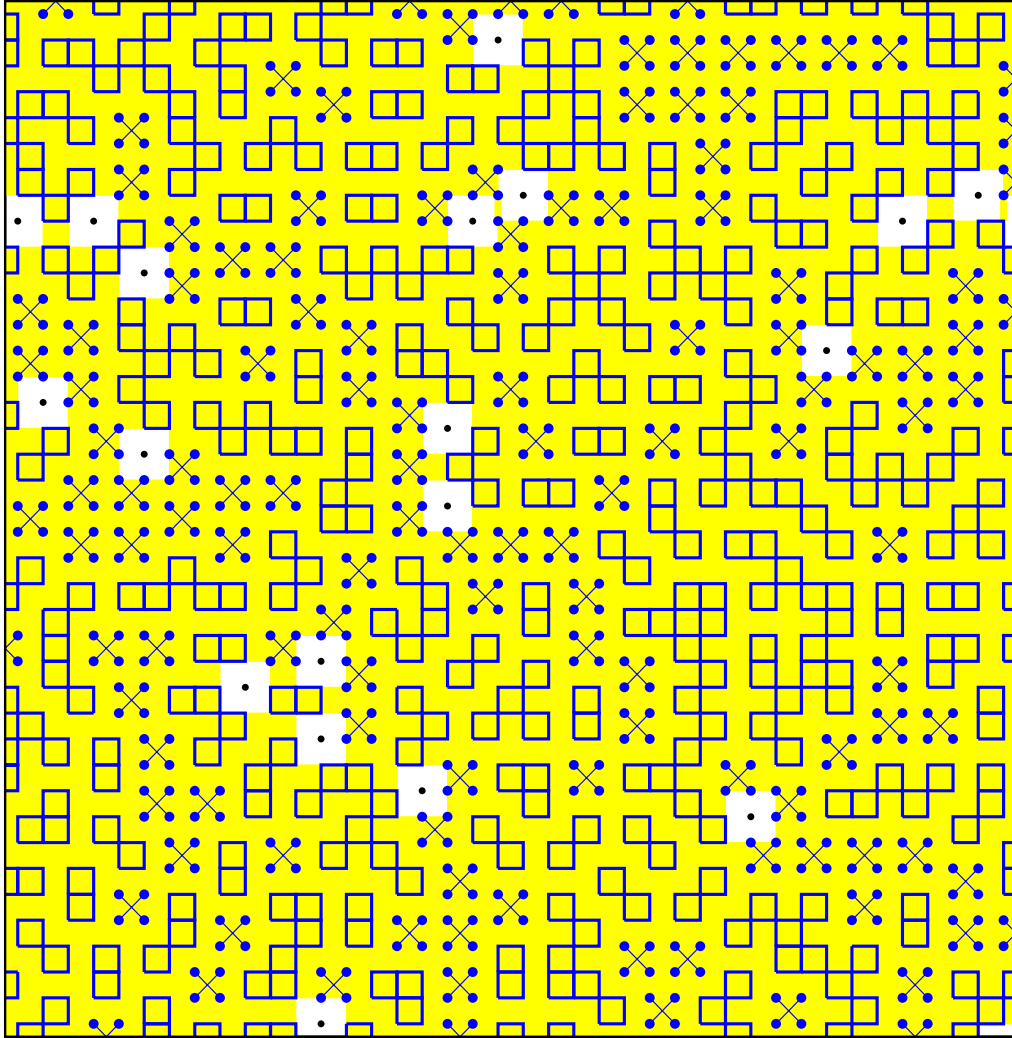


Figure S30 ($x = 0.30$): Plaquette doping of a 40×40 square CuO_2 lattice. Only the Cu sites are shown. The black dots are undoped AF Cu sites. The yellow plaquette clusters are comprised of more than 4 plaquettes and contribute to the superconducting pairing because they are larger than the coherence length. The yellow overlay represents the metallic region comprised of planar Cu $d_{x^2-y^2}$ and planar O p_σ character. Fluctuating dumbbells are inside non-overlapping plaquettes. Plaquette overlap is shown by blue squares. Edge overlap of plaquettes is no longer possible. Added plaquettes overlap existing plaquettes at three metallic sites. Only isolated localized spins remain (there are no adjacent black dots).

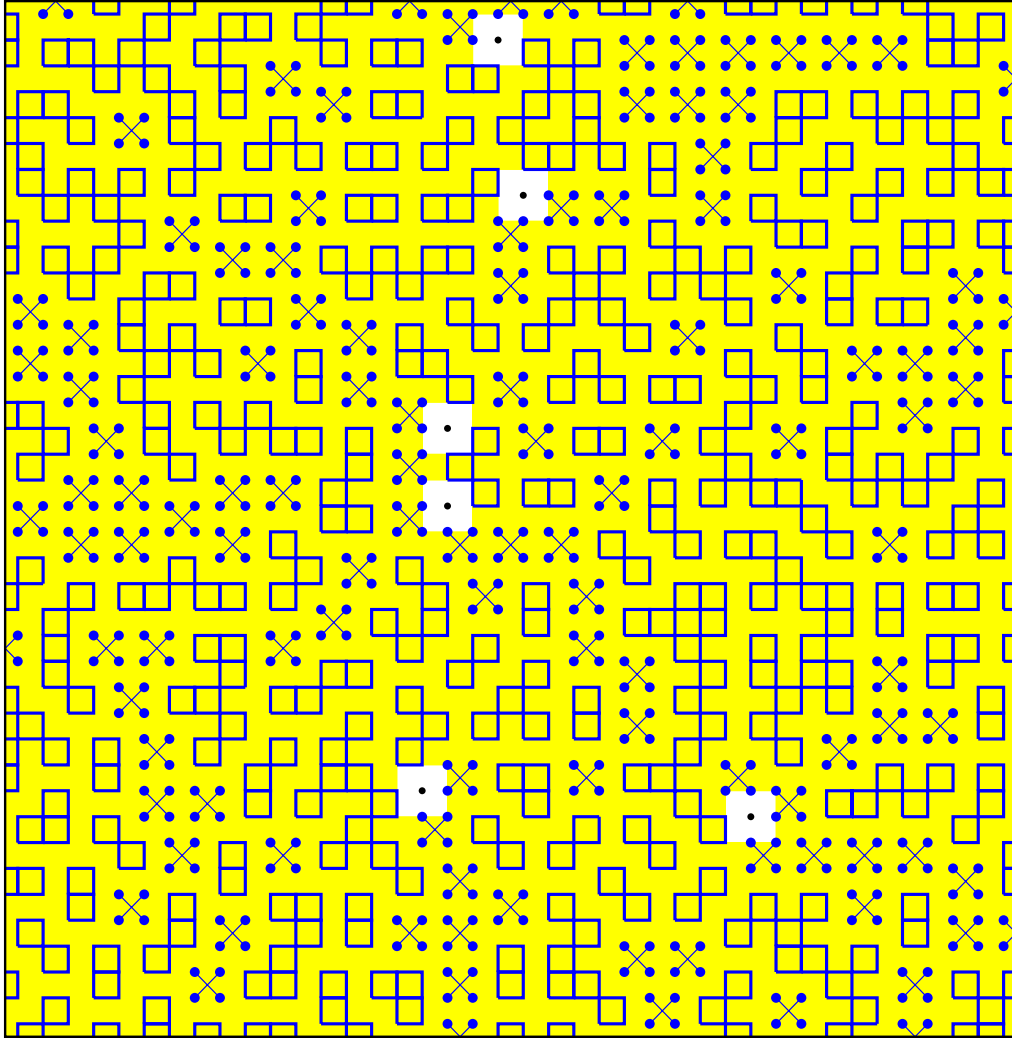


Figure S31 ($x = 0.31$): Plaquette doping of a 40×40 square CuO_2 lattice. Only the Cu sites are shown. The black dots are undoped AF Cu sites. The yellow plaquette clusters are comprised of more than 4 plaquettes and contribute to the superconducting pairing because they are larger than the coherence length. The yellow overlay represents the metallic region comprised of planar Cu $d_{x^2-y^2}$ and planar O p_σ character. Fluctuating dumbbells are inside non-overlapping plaquettes. Plaquette overlap is shown by blue squares. Edge overlap of plaquettes is no longer possible. Added plaquettes overlap existing plaquettes at three metallic sites. Only isolated localized spins remain (there are no adjacent black dots).

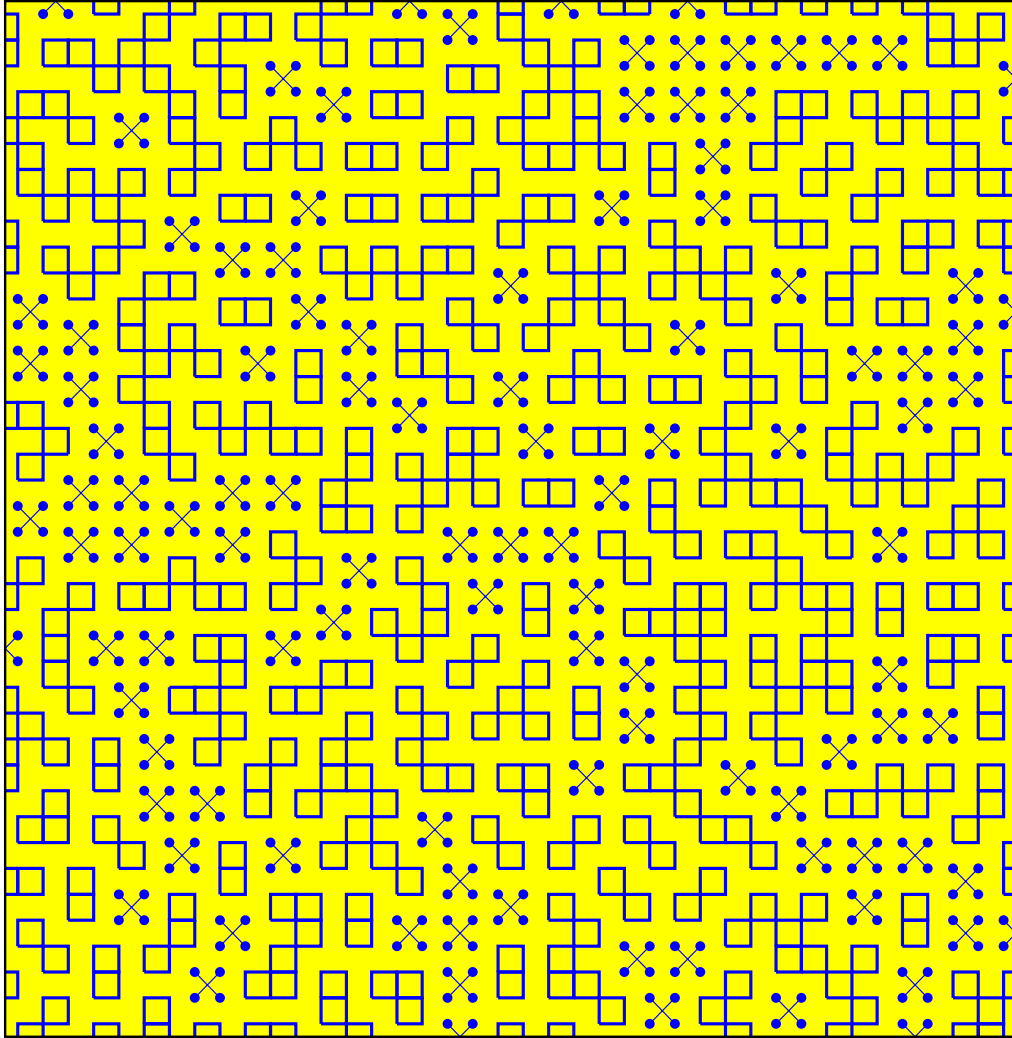


Figure S32 ($x = 0.32$): Plaquette doping of a 40×40 square CuO_2 lattice. Only the Cu sites are shown. The black dots are undoped AF Cu sites. The yellow plaquette clusters are comprised of more than 4 plaquettes and contribute to the superconducting pairing because they are larger than the coherence length. The yellow overlay represents the metallic region comprised of planar Cu $d_{x^2-y^2}$ and planar O p_σ character. Fluctuating dumbbells are inside non-overlapping plaquettes. Plaquette overlap is shown by blue squares. Edge overlap of plaquettes is no longer possible. Added plaquettes overlap existing plaquettes at three metallic sites. There are no remaining localized spins (black dots). The crystal is 100% metallic. There is no metal-insulator interface to produce superconducting pairing, and therefore $T_c = 0$.